ISSN: 2376-2136 (Print)
ISSN: 2376-2144 (Online)

# Trends in Renewable Energy

Volume 6, Issue 1, April 2020

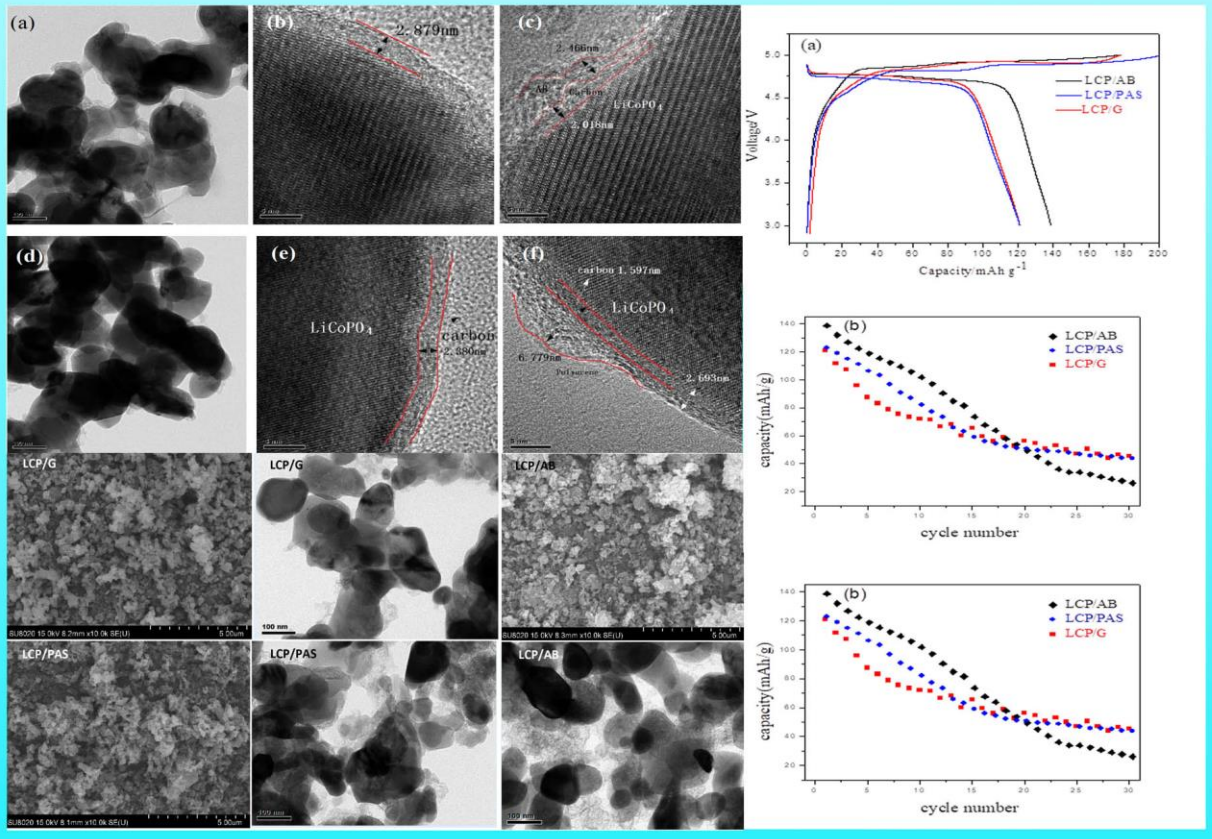


Cover image: Double carbon coated $LiCoPO_4$ cathode for Lithium ion batteries, see article by Yu, Liu *et al.* in this issue.

ISSN 2376-2136
9 772376 213001 16

futureenergysp.com
thefutureenergy.org

# Trends in Renewable Energy

**ISSN: 2376-2136 (Print) ISSN: 2376-2144 (Online)**

**http://futureenergysp.com/**

---

Trends in Renewable Energy is an open accessed, peer-reviewed semi-annual journal publishing reviews and research papers in the field of renewable energy technology and science.

The aim of this journal is to provide a communication platform that is run exclusively by scientists working in the renewable energy field. Scope of the journal covers: Bioenergy, Biofuel, Biomass, Bioprocessing, Biorefinery, Biological waste treatment, Catalysis for energy generation, Energy conservation, Energy delivery, Energy resources, Energy storage, Energy transformation, Environmental impact, Feedstock utilization, Future energy development, Green chemistry, Green energy, Microbial products, Physico-chemical process for Biomass, Policy, Pollution, Renewable energy, Smart grid, Thermo-chemical processes for biomass, etc.

The Trends in Renewable Energy publishes the following article types: peer-reviewed reviews, mini-reviews, technical notes, short-form research papers, and original research papers.

*The article processing charge (APC), also known as a publication fee, is fully waived for the Trends in Renewable Energy.*

# Editorial Team of Trends in Renewable Energy

## EDITORIAL BOARD

| | |
|---|---|
| Dr. Jun Mei | School of Chemistry and Physics, Science and Engineering Faculty, Queensland University of Technology, Australia |
| Dr. Valeria Di Sarli | Institute for Research on Combustion, National Research Council of Italy, Italy |
| Dr. Utkucan Şahin | Assistant Prof., Department of Energy Systems Engineering, Faculty of Technology, Muğla Sıtkı Koçman University, Turkey |
| Dr. ALIASHIM ALBANI | School of Ocean Engineering, Universiti Malaysia Terengganu, Malaysia |
| Dr. Ashwini Kumar | Assistant Prof., College of Engineering, HSBPVT's Parikrama Group of Institutions, India |
| Dr. Hasan AYDOGAN | Associate Prof., Mechanical Engineering Department, Selcuk University, Turkey |
| Dr. Jiekang Wu | Professor, School of Automation, Guangdong University of Technology, China |
| Dr. Ong Huei Ruey | DRB-HICOM University of Automotive, Malaysia |
| Dr. Miguel Ángel Reyes Belmonte | IMDEA Energy Institute, Spain |
| Dr. Chitra Venugopal | Associate Professor in Electrical Engineering, University of Trinidad and Tobago, Trinidad |
| Dr. Amit Kumar Singh | Assistant Prof., Instrumentation & Control Engineering Department, Dr. B.R.A. National Institute of Technology, India |
| Dr. Suvanjan Bhattacharyya | University of Pretoria, South Africa |
| Dr. Karunesh Tiwari | Babu Banarasi Das University, India |
| Dr. Sharadrao A. Vhanalkar | Karmaveer Hire Arts, Science, Commerce and Education College, India |
| Dr. Prasenjit Chatterjee | Assistant Prof. and Head, MCKV Institute of Engineering, India |
| Dr. S. Balamurugan | Mindnotix Technologies, India |
| Dr. Mohammad Nurunnabi | University of Oxford, United Kingdom |
| Dr. Kenneth Okedu | Caledonian College of Engineering, Oman |
| Dr. Cheng Zhang | Sr. Materials Engineer, Medtronic, Inc., United States |
| Dr. Chandani Sharma | Assistant Prof., Department of Electrical Engineering, Graphic Era University, India |
| Dr. Kashif Irshad | Assistant Prof., Mechanical Engineering Department, King Khalid University, Saudi Arabia |
| Dr. Abhijit Bhagavatula | Principal Lead Engineer, Southern Company Services, United States |
| Dr. S. Sathish | Associate Prof., Department of Mechanical Engineering, Hindustan University, India |
| Mr. A. Avinash | Assistant Prof., KPR Institute of Engineering & Technology, India |
| Mr. Bindeshwar Singh | Assistant Prof., Kamla Nehru Institute of Technology, India |
| Dr. Yashar Hashemi | Tehran Regional Electric Company, Iran |
| Dr. Navanietha Krishnaraj R | South Dakota School of Mines and Technology, United States |
| Dr. SANDEEP GUPTA | JECRC University, India |
| Dr. Shwetank Avikal | Graphic Era Hill University, India |
| Dr. Xianglin Zhai | Poochon Scientific LLC, United States |
| Dr. Rui Li | Assistant Prof., College of Engineering, China Agricultural University, China |
| Dr. Adam Elhag Ahmed | National Nutrition Policy Chair, Department of Community Services, College of Applied Medical Sciences, King Saud University, Saudi Arabia |
| Dr. Jingbo Li | Massachusetts Institute of Technology, United States |
| Dr. Srikanth Mutnuri | Associate Prof., Department of Biological Sciences, Associate Dean for International Programmes and Collaboration, Birla Institute of Technology & Science, India |
| Dr. Bashar Malkawi | S.J.D., Associate Prof., College of Law, University of Sharjah, United Arab Emirates |
| Dr. Simona Silvia Merola | Istituto Motori - National Research Council of Naples, Italy |
| Dr. Hakan Caliskan | Faculty of Engineering, Department of Mechanical Engineering, Usak University, Turkey |

# Table of Contents

## Volume 6, Issue No. 1, April 2020

## Articles

Trends in Renewable Energy
OPEN ACCESS ISSN: 2376-2144
Peer-Reviewed Article futureenergysp.com/index.php/tre

# Double Carbon Coated $LiCoPO_4$ Nano Composite as High-Performance Cathode for Lithium Ion Batteries

Yong Yu[a], Huifang Zhao[a], Yao Chen[a], Zeng-kai Feng[b], Xiaomin Liu[a,*], and Hui Yang[a]

[a]*School of Material Science and Engineering, Nanjing Tech University, Nanjing, Jiangsu, China*
[b]*Foshan Branch, Beijing Landmark Engineering Co., Ltd., Foshan, Guangdong, China*

Received November 23, 2019; Accepted December 15, 2019; Published January 2, 2020

Polyacene(PAS)/carbon and acetylene black(AB)/carbon coated lithium cobalt phosphate composites were synthesized via the solid state reaction method using co-precipitated $Co_3(PO_4)_2 \cdot 8H_2O$ and $Li_3PO_4$ mixture as its precursor. X-ray powder diffraction (XRD) was performed to investigate the structure and phase of all the samples. The transmission electron microscopy (TEM) shows that the double carbon layers coated on the surface of $LiCoPO_4$ successfully. The $LiCoPO_4$/C, $LiCoPO_4$/PAS and $LiCoPO_4$/AB delivered a capacity of T 120.92, 121.07 and 138.06 $mAh \cdot g^{-1}$ at 0.1C, respectively. The double carbon coated $LiCoPO_4$ electrode delivered an initial discharge capacity of 147.12, 143.51 $mAh \cdot g^{-1}$ after AB/glucose, PAS/glucose coating, which maintained at 59.5% and 61.7% after 15 cycles at the 0.1C rate, respectively.

*Keywords: Double carbon coated $LiCoPO_4$ nano composite; High-performance cathode; Lithium ion battery*

## Introduction

As renewable energy usage increases and price falls, energy storage becomes more and more important. The development of lithium-ion battery technology has opened the door to opportunities for the future of energy storage. For decades, scientists have been actively searching for new electrode materials and electrolytes that can produce a new generation of lithium-ion batteries which can provide greater energy storage, longer life, lower cost, and greater safety.

Olivine type $LiMPO_4$ (M = Fe, Mn, Co, Ni) cathode materials is one of the most promising positive electrode materials for next-generation lithium-ion batteries (LIBs) owing to the strong P-O covalent bond and the resulting stability [1]. Among $LiMPO_4$ materials, $LiFePO_4$ is widely applicated in the field of electric and hybrid electric vehicles (HEVs) [2, 3], because of its low cost, environmental benignity, excellent thermal stability and outstanding cyclability [4]. However, the energy density of $LiFePO_4$ (586 $Wh \cdot Kg^{-1}$) limits its further development due to the low discharge potential (3.4 V vs. $Li^+/Li$). $LiCoPO_4$ presents the $Li^+$ extraction/insertion behaviour at potentials around 4.8 V (vs. $Li^+/Li$), which is highly beneficial to its energy density (801 $Wh \cdot Kg^{-1}$). But its poor electronic conductivity (~$10^{-9}$ $S \cdot cm^{-1}$) [5] and ion conductivity ($8.8 \times 10^{-8}$ $S \cdot cm^{-1}$ at 27°C) [6] make it difficult to exhibit $Li^+$ insertion/extraction. On the other hand, there is no suitable 5 V electrolyte matching with its high operating voltage, which is the essential

**Corresponding author:* liuxm@njtech.edu.cn

Tr Ren Energy, 2020, Vol.6, No.1, 1-11. doi: 10.17737/tre.2020.6.1.00108

reason for the fast capacity fading. Both causes lead to poor electrochemical performance and short service life of the pristine $LiCoPO_4$. In order to optimize the performance of $LiCoPO_4$, particle size reduction [7, 8], carbon coating [9-12] and cation doping on the Co site [13, 14] have been adopted to improve the initial discharge capacity and rate capability. The addition of conductive compounds or polymers can shrink the transport path length of Li ion, increase the electronic conductivity and modify the surface of pure $LiCoPO_4$ [15]. Moreover, a uniform and compact carbon network layer which can prevent direct contact between the active mass and HF in the electrolyte is critical for the cathode material.

In this paper, a novel double carbon layers coated $LiCoPO_4$ is designed, where carbon is the first layer to make the conductive carbon adhere tightly on the surface of $LiCoPO_4$, the polyacene (PAS) or acetylene black (AB) is the second layer coating on the inner carbon layer to enhance the electronic conductivity of $LiCoPO_4$. In addition, the outer carbon layer can prevent the spalling of the first carbon layer and avoid partial irreversible structure changes during its charging and discharging process, thus extending the cycle life.

## Experimental

$LiCoPO_4$ samples were prepared by the solid-state sintering method, in which the precursors ($Li_3PO_4$ and $Co_3(PO_4)_2{\cdot}8H_2O$) were prepared via a co-precipitation route using a micro reactor followed by stirring at 60 ℃ for 1 h. The processing procedure of the precursor ($Li_3PO_4$ and $Co_3(PO_4)_2$) and bare $LiCoPO_4$ (LCP) were described in our previous paper [16].

For single carbon coated samples, the precursor LC-1 ($n_{Li}$:$n_{Co}$ = 2:1 in the reactant) was mixed with 3 wt% acetylene black, 5 wt% phenol–formaldehyde resins or 10 wt% glucose using a planetary milling machine. The obtained mixture was calcined at 650 ℃ for 10h in an $Ar/H_2$ (5%) atmosphere to generate materials LCP/C, labelled as LCP/AB, LCP/PAS and LCP/C, respectively.

In order to get the double carbon coated $LiCoPO_4$ composites, the dried precursor was ball-milled with 10 wt% glucose for 5 h in ethanol. Then the samples were dried to evaporate ethanol and heated at 350 ℃ for 5 h to synthesize the glucose coated composites. The obtained composite was ball-milled with 1 wt% acetylene black for 5 h. Then the above mixture was calcined at 650 ℃ for 10 h in $Ar/H_2$ (5%) to generate LCP/C@AB. In the similar procedure, the LCP/C@PAS composites are obtained by substituting acetylene black with 3 wt% phenol–formaldehyde resin.

The crystal structure of synthesized materials was evaluated by powder X-ray diffraction (XRD, Model X'TRA, Thermo Electron, USA). The morphology and microstructure features were studied by using a field emission scanning electron microscope (FESEM, JSM-6700F, JEOL, Japan) and a transmission electron microscope (TEM, JEM-1010, JEOL, Japan).

For electrochemical performance testing, the cathode was prepared by coating a slurry of 7 active material, carbon black and PVDF with 75:15:10 wt% on aluminium foil, using N-methylpyrrolidone (NMP) as solvent, followed by vacuum-dried at 120℃ for 12h. The cathode electrode was characterized with CR2032 coin cells assembled in an argon-filled glove box. An electrochemical 2032 coin cell consisted of an active material as the cathode, lithium foil as the counter electrode, 1 M $LiPF_6$ in a 1:1 (by vol) mixture

of dimethyl carbonate (DMC) and ethylene carbonate (EC) as the electrolyte, and celgard 2400 as the separator. The galvanostatic cycling profiles of the cells were recorded at different current densities between 3.0 V-5.0 V under room temperature. The electrochemical impedance spectroscopy of these cells was also tested with an electrochemical workstation (CHI650D, Shanghai Chenhua Instrument Co., Ltd., China) in the frequency ranging from 0.1 Hz to 1 M Hz.

## Results and Discussion

Fig.1 shows the XRD patterns of the LCP samples synthesized by using LC-1 as the precursor. Like LCP-1 in the previous study, the characteristic peaks of carbon and $Li_3PO_4$ were not detected in LCP/C, LCP/C@PAS and LCP/C@AB composite, all peaks were consistent with $LiCoPO_4$ [JCPDS#32-0552]. The refined lattice parameters and crystallite sizes for the as-obtained products are summarized in Table 1. The estimated crystallite size of LCP-1 is much larger than those of carbon coated samples, indicating that the carbon can prevent the growth of $LiCoPO_4$ particles efficiently. In addition, the parameters of LCP/C@PAS and LCP/C@AB are smaller than those of LCP/C, demonstrating that the growth of $LiCoPO_4$ crystallite is highly inhibited by residual carbon particles degraded from double carbon sources.

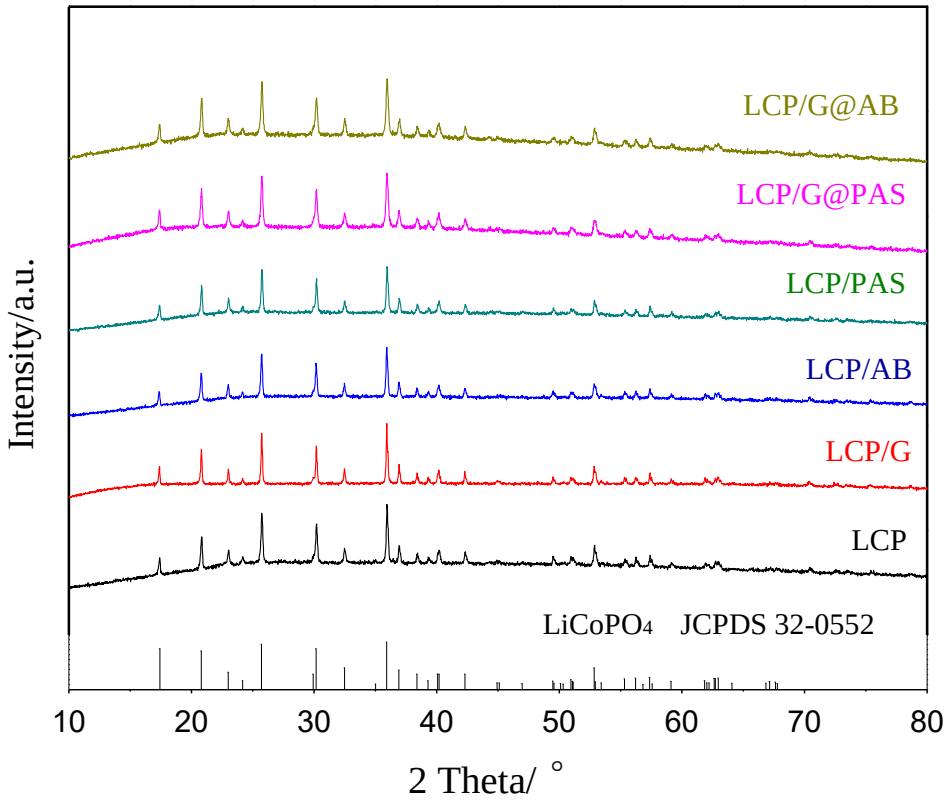


**Fig. 1.** XRD patterns of $LiCoPO_4$ composite samples

**Table 1.** The refined lattice parameters and crystallite sizes of LCP, LCP/C, LCP/G@PAS and LCP/G@AB

| Sample name | A(Å) | b(Å) | c(Å) | V(Å) | Crystal size(nm) |
|---|---|---|---|---|---|
| LCP-1 | 5.9235 | 10.2132 | 4.7003 | 284.35 | 50.8796 |
| LCP/C | 10.2132 | 5.9235 | 4.7003 | 284.3582 | 49.8796 |
| LCP/PAS | 5.9235 | 10.2027 | 4.6992 | 283.99 | 48.8717 |
| LCP/AB | 10.2015 | 5.9131 | 4.6991 | 283.4614 | 47.9743 |
| LCP/C@PAS | 5.9274 | 10.1856 | 4.6220 | 279.05 | 41.3464 |
| LCP/C@AB | 5.9124 | 10.2026 | 4.6873 | 282.75 | 40.9086 |

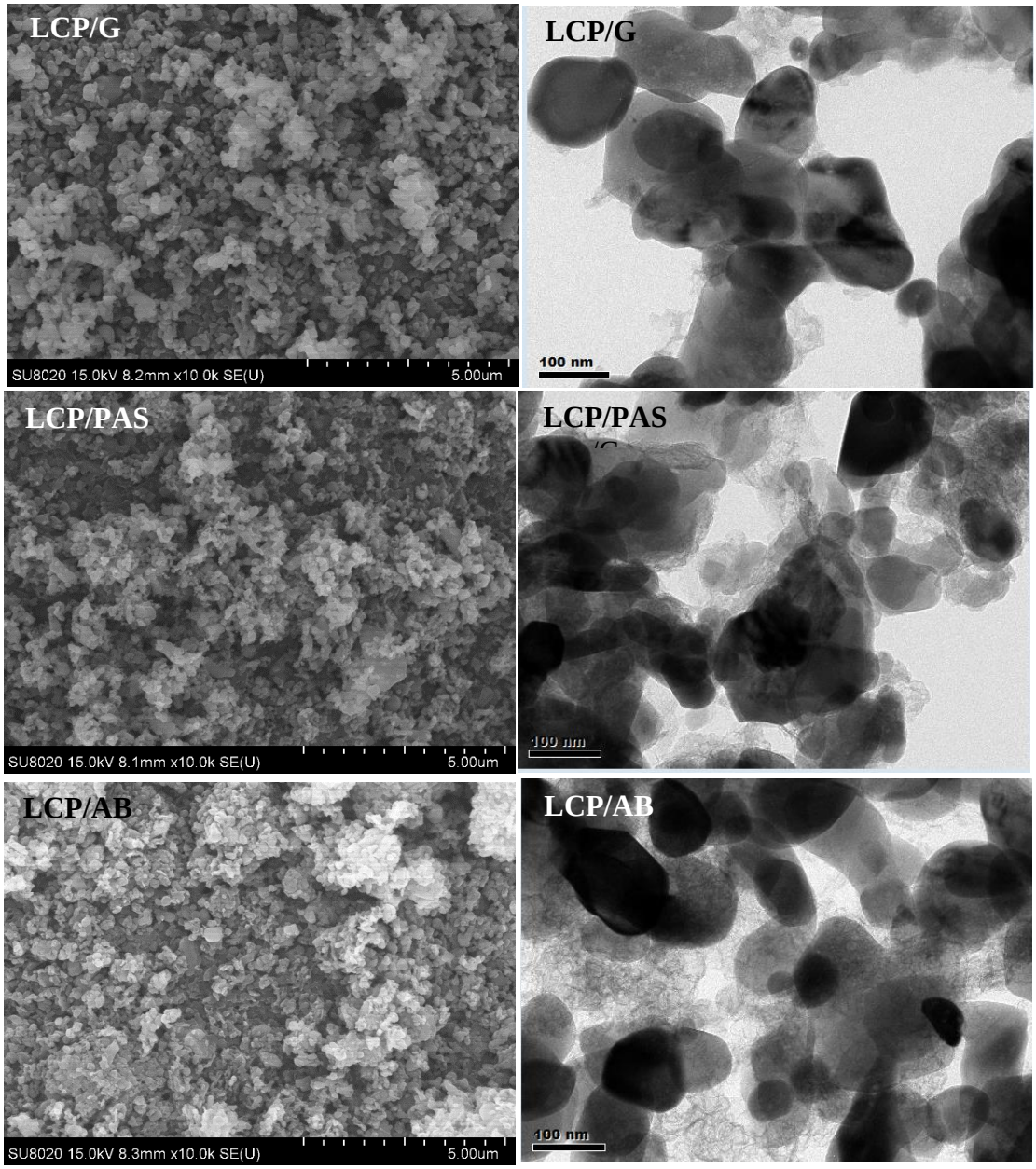


**Fig. 2.** SEM and TEM images of LCP/G, LCP/PAS and LCP/AB

The SEM and TEM images in Fig. 2 show the size, morphologies and carbon layer distribution of LCP/AB, LCP/C and LCP/PAS. The diameter scattering of LCP/G and LCP/PAS particles with slight agglomeration was uniform, in the range of 100-150 nm. The carbon pyrolyzed from organic glucose and phenol formaldehyde resin were different. For LCP/C, the carbon layer was coated on the $LiCoPO_4$ particles more tightly. The conductive polymer PAS layer had an increased thickness and presented a loose layer. Larger particles around 150 μm in size were formed in LCP/AB, and the floc-like pyrolytic products of acetylene black were dispersed among LCP particles, which may promote electronic conduction.

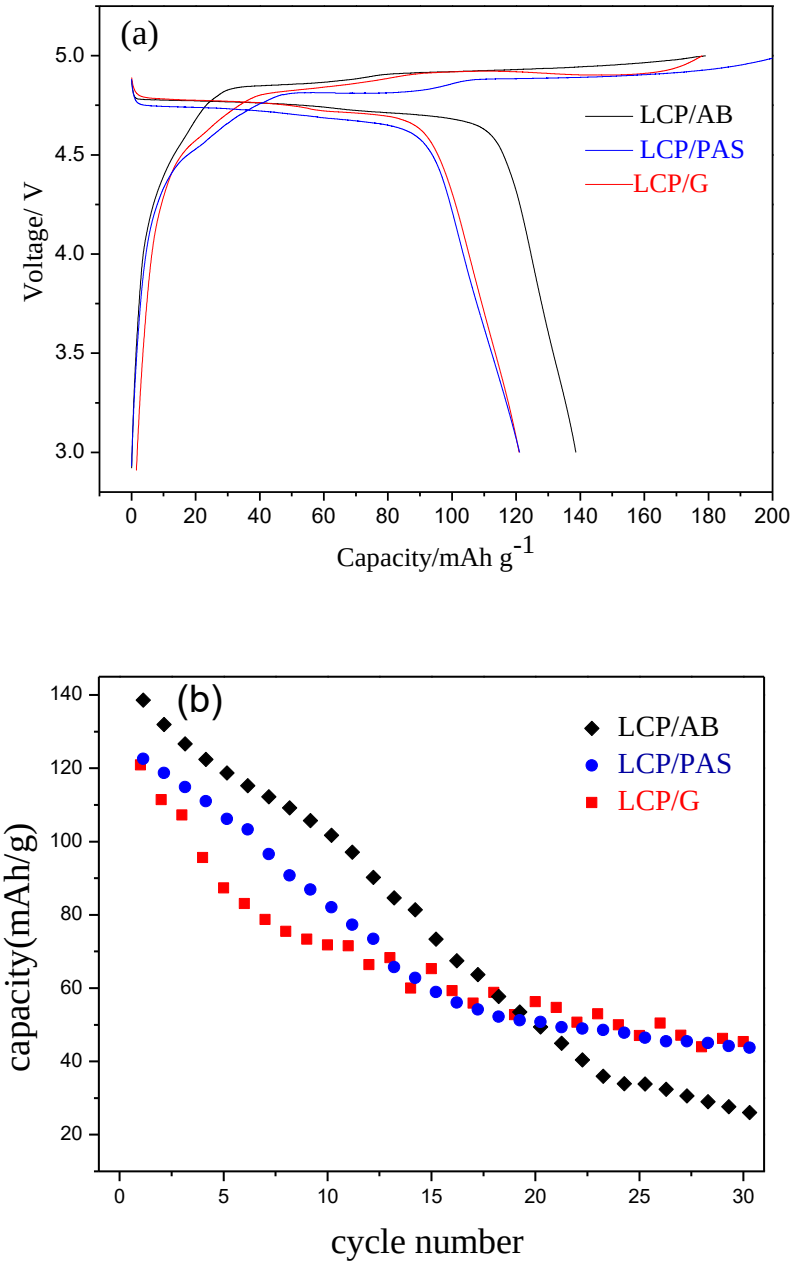


**Fig. 3.** Charge and discharge curves (a) and cycle performances of single carbon coated $LiCoPO_4$ composites at 0.1C (b)

Fig. 3 presents the electrical performance of single carbon coated $LiCoPO_4$ composites at 0.1C rate. Fig. 3a shows that the $LiCoPO_4$/C, $LiCoPO_4$/PAS, $LiCoPO_4$/AB owned a reversible capacity of 120.92, 121.07 and 138.06 mAh $g^{-1}$, respectively. Although LCP/AB presents the highest initial capacity, its capacity fading was very pronounced with a progressive decrease to 21.9 $mAh \cdot g^{-1}$ in the $30^{th}$ cycle. A better performance was achieved by glucose and phenol–formaldehyde resins pyrolytic carbonization. The LCP/G and LCP/PAS composites showed a similar capacity and capacity retention, which were 120.9 $mAh \cdot g^{-1}$, 3.7% and 121.1 $mAh \cdot g^{-1}$, 33.2%, respectively. The capacity curve of sample LCP/C dropped more sharply in the first 10 cycles. The carbon layer produced from pyrolysis of organic glucose and phenol–formaldehyde resins was more homogeneous and coated on the entire particle surface. The carbon decomposed by organic carbon, especially organic polymers was dispersed at the atomic level in the reaction system, which realized the uniform coating on the synthesized products and formed an interconnected conductive carbon film enhancing the structural stability, resulting in better cyclic performance.

Fig. 4 presents the TEM images of double carbon coated $LiCoPO_4$ samples. It is worth noting that the particle size of double carbon coated $LiCoPO_4$ was about 150 nm, which is smaller than those of LCP/C (200 nm on average). In the TEM photographs, it is found that the $LiCoPO_4$ particles were wrapped by two carbon layers. And the TEM images also exhibited the thickness and the boundary of the carbon layer on the surface of $LiCoPO_4$. The distribution of the carbon layer was related to the carbon source additives. In the case of LCP/C@PAS, the TEM images exhibited visually the $LiCoPO_4$ with hierarchical conductive architecture which consisted of 1.59 nm inner residual carbon layer and 1 nm outer polyacene polymer layer. But the outer polyacene layer distributeed unevenly. The sample LCP/C@AB presented a ~2 nm thick inner residual carbon layer and a 2.41 nm thick acetylene black outer layer. Although the carbon layer of LCP/C@AB was thicker than LCP/C@PAS, the outer layer was well-distributed.

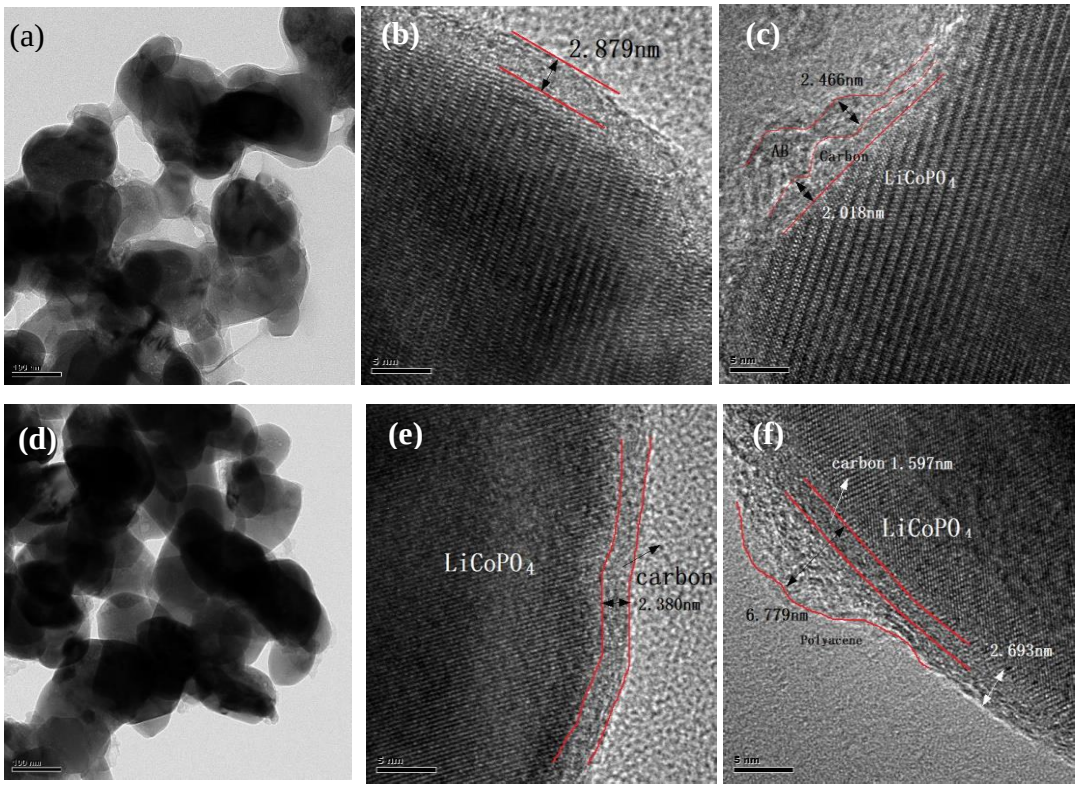


**Fig. 4**. TEM images of LCP/C@AB (a, b, c) and LCP/C@PAS (d,e,f)

The first charge and discharge curves of LCP/C@AB and LCP/C@PAS at 0.1C rate in the voltage of 3.0-5.0 V at room temperature are shown in Fig. 5. The second discharge capacity of LCP/C@PAS and LCP/C@AB were 134.79 and 138.78 $mAh \cdot g^{-1}$, respectively, which were higher than previous samples except LCP-3. All the charge curves displayed two obvious charge plateaus (one at about 4.8 V and the other at about 4.9 V) in the aspect of discharge profiles, and the quite different discharge behavior (shape of curve and evolution of voltage plateau) should be noted. A discharge plateau at ~4.8 V was obvious for LCP/C@PAS, while the LCP/C@AB showed a discharge plateau at 4.6 V. The discharge voltage of the active material fell sharply to the cut-off voltage (3.0 V), indicating a greater polarization. The LCP/C@AB exhibited a reversible specific capacity of 147.12 $mAh \cdot g^{-1}$ which was down to 59.5% and 11.9% after 15 cycles and 50 cycles, respectively. The LCP/C@PAS exhibited a reversible specific capacity of 143.51$mAh \cdot g^{-1}$ which was down to 61.7% after 15 cycles and remained up to 21.6% after 50 cycles. Compared with the samples of LCP/G, LCP/AB, LCP/PAS and LCP/G@AB, LCP/G@PAS showed a much better cyclability, which are mainly attributed to the synergistic effect of double carbon. On the one hand, the double carbon can more uniformly and finely refine the crystal particles, thereby shortening the length of the lithium ion transmission path, increasing the conductivity and modifying the surface of $LiCoPO_4$. On the other hand, the outer carbon layer can make the inner carbon layer more closely contact the active material, prevent the active material from directly contacting HF in the electrolyte, and prevent the inner layer from spalling during the charge and discharge process.

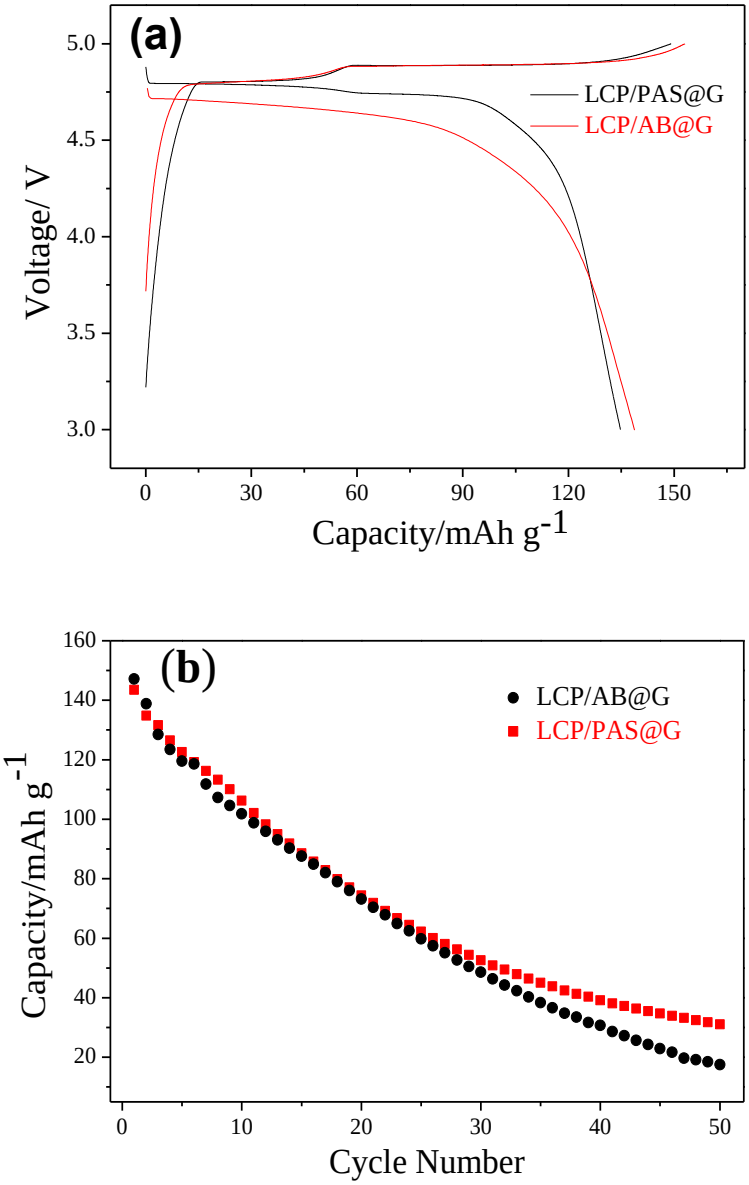


**Fig. 5.** Charge and discharge curves of double carbon coated $LiCoPO_4$ composite (a); Cycle performances of double carbon coated $LiCoPO_4$ composite at 0.1C (b)

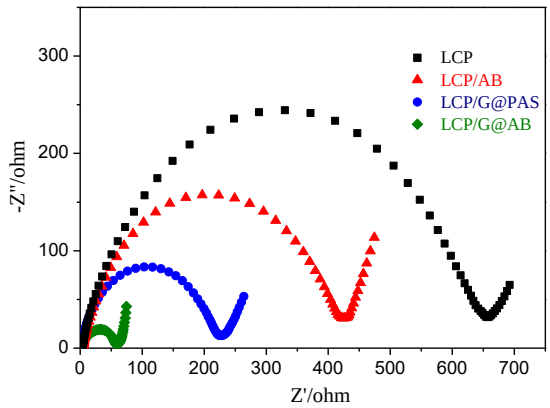


**Fig. 6.** Nyquist plots of the cells using $LiCoPO_4$ samples synthetized with different carbon sources.

Fig.6 presents the EIS impedance curves of the LCP and LCP/AB and double carbon coated samples $LiCoPO_4$/G@PAS and $LiCoPO_4$/G@AB at fully charged state after one cycle. The total impedance of the sample was mainly induced by the charge-transfer impedance between the electrolyte and the electrode interface, which could be assigned by the diameter of the semicircle in the curve. The diameter of the semicircle of the double carbon coated $LiCoPO_4$ was significantly smaller than that of pure LCP and single carbon coated LCP, and the impedance of the sample LCP/G@AB is the smallest. The small charge-transfer impedance of LCP/G@AB is attributed to the finer particles and the more stable architecture of double conducting layers, which benefits to its electrochemistry property distinctly, in accordance with its larger capacity.

## CONCLUSIONS

In summary, the pyrolytic carbon coated $LiCoPO_4$ composites were synthesized by a micro-reactor assisted co-precipitation and then through a single/double carbon source coating route. $LiCoPO_4$/AB presented the largest initial discharge capacity of 138.06 $mAh \cdot g^{-1}$ among all single carbon coated $LiCoPO_4$ samples which could ascribe to the floc-like acetylene distributed in the LCP particles, thereby ameliorating the conductivity. And the discharge capacity and cyclability were further improved by glucose/AB and glucose/PAS coating, with initial capacities of 147.12 and 143.51 $mAh \cdot g^{-1}$, respectively. The longer cycle life of the $LiCoPO_4$/G@PAS sample can be ascribed to the finer particles and the more stable architecture of double conducting layers. The facile routine reported herein may be extended to prolong the cycle life of other electrode materials.

## ACKNOWLEDGMENTS

This work was supported by the Natural Science Foundation of China (Grant No. 21573109), and the Priority Academic Program Development of Jiangsu Higher Education Institutions.

## CONFLICTS OF INTEREST

The authors declare that there is no conflict of interests regarding the publication of this paper.

## REFERENCES


[1] Truong, Q. D., Devaraju, M. K., Ganbe, Y., Tomai, T., and Honma, I. (2014). Controlling the shape of $LiCoPO_4$ nanocrystals by supercritical fluid process for enhanced energy storage properties. *Scientific Reports*, 4(2), 3975.

[2] Liu, X., Yan, P., Xie, Y., Yang, H., Shen, X. and Ma, Z. (2013) Synthesis of superior fast charging–discharging nano-$LiFePO_4$/C from nano-$FePO_4$ generated using a confined area impinging jet reactor approach, *Chemical Communication*, 49, 5396.

[3] Yan, P., Lu, L., Liu, X., Cao, Y., Zhang, Z., Yang, H. and Shen, X. (2013) An economic and scalable approach to synthesize high power $LiFePO_4$/C nanocomposites from nano-$FePO_4$ precipitated from an impinging jet reactor, *Journal of Materials Chemistry A*, 1, 10429

[4] Goodenough, J. B., and Park, K. S. (2013). The Li-Ion Rechargeable Battery: A Perspective. *Journal of the American Chemical Society*, 135(4), 1167-1176.

[5] Wolfenstine, J., Lee, U., Poese, B., and Allen, J. L. (2005). Effect of oxygen partial pressure on the discharge capacity of LiCoPO4. *Journal of Power Sources*, 144(1), 226-230. DOI: 10.1016/j.jpowsour.2004.12.013

[6] Morgan, D., Van der Ven, A., and Ceder, G. (2004). Li conductivity in LixMPO4 (M = Mn, Fe, Co, Ni) olivine materials. *Electrochemical and Solid State Letters*, 7(2), A30-A32. DOI: 10.1149/1.1633511

[7] Gangulibabu, Nallathamby, K., Meyrick, D., and Minakshi, M. (2013). Carbonate anion controlled growth of LiCoPO4/C nanorods and its improved electrochemical behavior. *Electrochimica Acta*, 101, 18-26. DOI: 10.1016/j.electacta.2012.09.115

[8] Wang, F., Yang, J., NuLi, Y., and Wang, J. (2011). Novel hedgehog-like 5V LiCoPO4 positive electrode material for rechargeable lithium battery. *Journal of Power Sources*, 196(10), 4806-4810. DOI: 10.1016/j.jpowsour.2011.01.055

[9] Liu, J., Conry, T. E., Song, X., Yang, L., Doeff, M. M., and Richardson, T. J. (2011). Spherical nanoporous LiCoPO4/C composites as high performance cathode materials for rechargeable lithium-ion batteries. *Journal of Materials Chemistry*, 21(27), 9984-9987. DOI: 10.1039/c1jm10793c

[10] Laszczynski, N., Birrozzi, A., Maranski, K., Copley, M., Schuster, M. E., and Passerini, S. (2016). Effect of coatings on the green electrode processing and cycling behaviour of LiCoPO4. *Journal of Materials Chemistry A*, 4(43), 17121-17128. DOI: 10.1039/c6ta05262b

[11] Wolfenstine, J., Read, J., and Allen, J. L. (2007). Effect of carbon on the electronic conductivity and discharge capacity LiCoPO4. *Journal of Power Sources*, 163(2), 1070-1073. DOI: 10.1016/j.jpowsour.2006.10.010

[12] The Nam Long, D., and Taniguchi, I. (2011). Preparation of LiCoPO4/C nanocomposite cathode of lithium batteries with high rate performance. *Journal of Power Sources*, 196(13), 5679-5684. DOI: 10.1016/j.jpowsour.2011.02.039

[13] Di Lecce, D., Manzi, J., Vitucci, F. M., De Bonis, A., Panero, S., and Brutti, S. (2015). Effect of the iron doping in LiCoPO4 cathode materials for lithium cells. *Electrochimica Acta*, 185, 17-27. DOI: 10.1016/j.electacta.2015.10.107

[14] Yang, S. M. G., Aravindan, V., Cho, W. I., Chang, D. R., Kim, H. S., and Lee, Y. S. (2012). Realizing the Performance of LiCoPO4 Cathodes by Fe Substitution with Off-Stoichiometry. *Journal of the Electrochemical Society*, 159(7), A1013-A1018. DOI: 10.1149/2.051207jes

[15] Ni, J., Wang, H., Gao, L., and Lu, L. (2012). A high-performance LiCoPO4/C core/shell composite for Li-ion batteries. *Electrochimica Acta*, 70, 349-354. DOI: 10.1016/j.electacta.2012.03.080

[16] Zhao, H., Yu, Y., Wang, G., Chen, Y., Liu, X., and Yang, H. (2018). Synthesis of nanosphere-like LiCoPO4 with excellent electrochemical performance via micro reactor assisted co-precipitation method. *Functional Materials Letters*, 11(05), 1850037. DOI: 10.1142/s1793604718500376



Trends in Renewable Energy
OPEN ACCESS ISSN: 2376-2144
Peer-Reviewed Review Article futureenergysp.com/index.php/tre

# Implementation of ANN Technique for Performance Prediction of Solar Thermal Systems: A Comprehensive Review

Ashfaque Ahmad, Harish Kumar Ghritlahre*, Purvi Chandrakar

*Department of Energy and Environmental Engineering, Chhattisgarh Swami Vivekanand Technical University, Bhilai, Chhattisgarh, 491107, India*

Received November 28, 2019; Accepted January 13, 2020; Published January 17, 2020

Solar thermal systems (STS) are efficient and environmentally safe devices to meet the rapid increasing energy demand now a days. But it is very important to optimize their performance under required operating condition for efficient usage. Hence intelligent system-based techniques like artificial neural network (ANN) play an important role for system performance prediction in accurate and speedy way. In present paper, it is attempted to scrutinize the approach of ANN as an intelligent system based method to optimize the performance prediction of different solar thermal systems accurately. Here, 25 research works related to various solar thermal systems have been reviewed and summarized to understand the impact of different ANN models and learning algorithms on performance prediction of STS. Using ANN, a brief stepwise summary of research work on various STS like solar air heaters, solar stills, solar cookers, solar dryers and solar hybrid systems, their predictions (results) and architectures (network and learning algorithms) in the literature till now, are also discussed here. This paper will genuinely help the future researchers to overview the work concisely related to solar thermal system performance prediction using various types of ANN models and learning algorithm and compare it with other global methods of machine learning.

*Keywords: Solar energy; Solar thermal systems; Artificial Neural Network; Learning algorithm*

## 1. Introduction

Energy is a primary feed in for almost all activities and economic development. Therefore, there is an ultimate dependency between the energy availability and the growth of a nation. Since energy is imperative to execute the operation of production, transport, agriculture and household services, the process of economic growth requires higher proportion of energy consumption, which forces us to focus on ensuring its continuous supply to meet our ever-rising demands [1-4].

The two main sources of energy are termed as conventional and non-conventional sources. Besides conventional energy sources like coal, petroleum and natural gas, some non-conventional energy sources also known as renewable energy sources are solar energy, wind energy, tidal energy and bioenergy.

Within these renewable energy sources available on earth, solar energy is the most plentiful and clean source of energy. The sun produces a huge amount of energy which is accumulated through a system and further converted into heat and electricity.

**Corresponding author:* harish.ghritlahre@gmail.com

Tr Ren Energy, 2020, Vol.6, No.1, 12-36. doi: 10.17737/tre.2020.6.1.00110

As energy demand is increasing rapidly for industrial as well as domestic use, it is now becoming crucially important to develop solar thermal systems as an efficient solution for this huge energy demand procurement. It can be achieved well only by maximizing the performance of solar thermal systems under specific operating conditions.

The experimental and mathematical study along with computational techniques, require a long time to come with precise results for a physical problem. On the other hand, the use of ANN technique as a performance prediction tool saves time and also provides key information patterns in a multi-dimensional information domain [5-35].

Compared to other computational techniques, ANN is simpler and more capable of solving complex non-linear relationship between the variables and extracted data [5].

The technique of Artificial Neural Network is used to model, optimize and predict a system's performance. Thanks to its faster processing speed and high accuracy, it has become more popular in the last two decades. Many researchers have used ANN technique in the domain of atmospheric sciences [6], chemical process control [7], energy systems [8, 9], modeling and control of combustion processes [10], photovoltaic applications [11], thermal science and engineering [12], sizing photovoltaic systems [13], refrigeration and heat pumps systems [14], nuclear engineering [15], controlling wind–PV power systems [16], solar radiations prediction [17], heat exchangers [18],wind energy systems [19], solar systems designing [20], hybrid energy systems [21], solid desiccant systems [22], solar collector systems [23] and various thermal systems [24-35].

In the previous years, ANN had been used by numerous researchers in the domain of energy utilization and conversion systems for performance predictions, designing heat pumps and PV systems, air conditioning, wind and PV power systems, hybrid energy systems and many other thermal systems [24-35].

ANN is a powerful data-driven, self-adaptive, flexible computational tool having capability of handling large amount of data sets. Additionally, this technique is found very suitable for implicitly detecting complex non-linear relationship between dependent and independent variables with high accuracy.

This inclusive review paper covers following points:

1. A concise discussion on ANN, its types, its field and methodology of implementation, usage in different solar thermal applications.
2. Different standard statistical performance evaluation criteria used in the evaluation of ANN performance are also discussed here.
3. The application of ANN in various solar thermal systems like solar collectors, solar air and water heaters, photovoltaic/thermal (PV/T) systems, solar dryers, solar stills and solar cookers are summarized here.
4. Conclusion and suggestions for future research are also outlined here.

## 1.1. Solar Thermal Systems

Solar systems are used to harness solar energy for generation of thermal or electrical energy that can be used in industrial and residential regions. Solar energy is used for heating of fluids also. A schematic chart of type of solar thermal systems is described in Figure 1. Chart clearly elaborates the classification of solar thermal systems according to their structure, construction material, and purpose of usage. Its application includes heating/cooling, desalination other than drying of fruits, meat, vegetables, egg incubation and other industrial purposes [1-3].

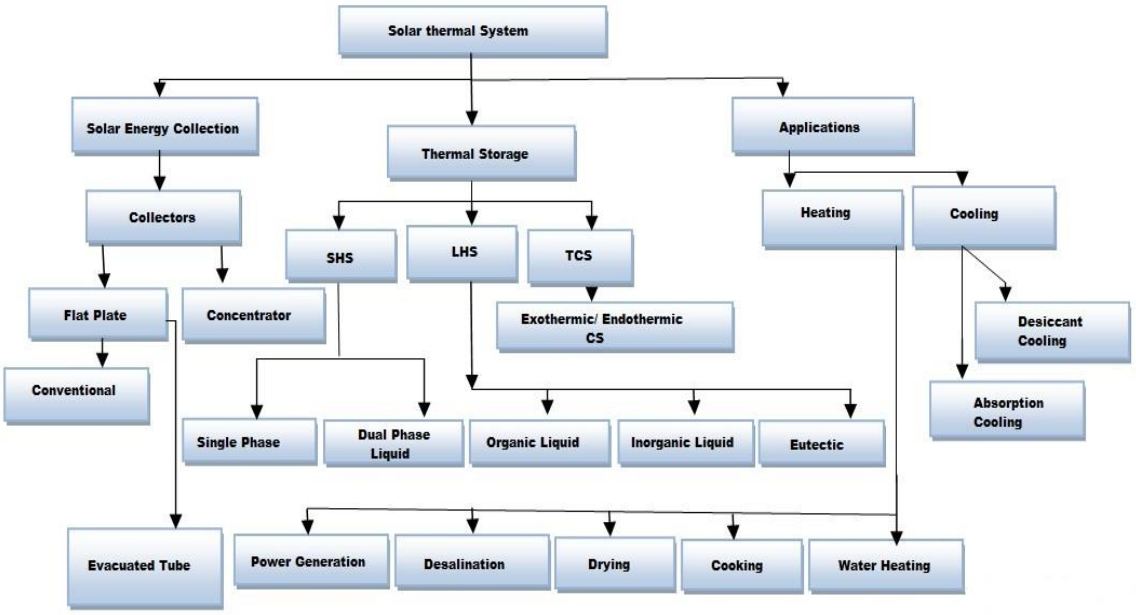


**Figure 1**. Solar thermal systems and their applications

## 2. Artificial Neural Network (ANN)

Artificial neural networks are data processing systems identical to data processing software in the human brain. Figure 2 clearly shows that neurons are basic elements, and dendrites, cell body or soma and synapses are other components, within biological networks. Dendrites receives input signals or information, cell body works as a processor, synaptic works as a reference, and axon transmits output signals to other neurons and performs non-linear operations [5, 23]. ANN system consists of many processing components, known as neurons.

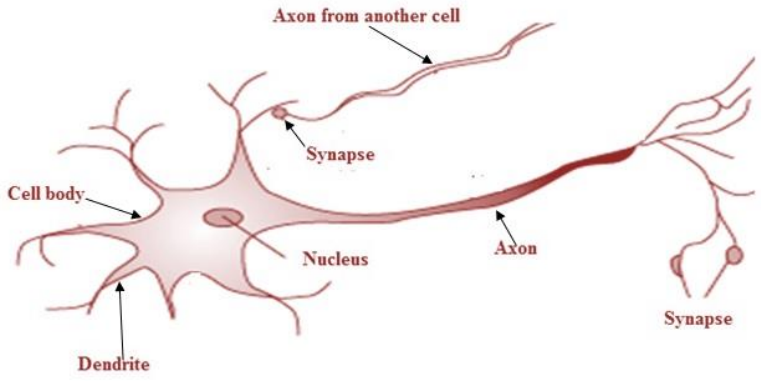


**Figure 2.** Basic structure of biological neurons

ANN functions work like the human brain in two ways: learning and storing information that is called weights in interconnected connections. The neuron collects multiple inputs in combination with attachment weights from other neurons and performs a nonlinear activation process and generates a single output data that can go to the other

neurons. Such input data is analyzed by the neurons and transferred to the next network layer.

In the solar thermal systems, following ANN models are used majorly:

1. Multi-layer feed forward neural network (MLFFNN)
2. Radial basis function (RBF)
3. General Regression Neural Network (GRNN)

## 2.1 Multi-layer Feed Forward Neural Network (MLFFNN)

The basic structure of multi-layer feed forward neural network (MLFFNN) is shown in Figure 3. The MLFFNN model basically contains three layers: one input layer, one or more hidden layers, and one output layer. Every neuron receives information from other neurons and moves over the hidden layers to the output layer. Interconnected nodes of storage termed as neurons, merge to render an ANN. Every neuron's output is the product of weighted inputs. The sum of weighted inputs formed by neurons is given as [5, 72, 73]:

$$X = \left( \sum_{i=1}^{n} w_{ij} a_i \right) + b_j \tag{1}$$

where, n is the number of input data (i = 0, 1, 2, 3……n) and $w_{ij}$ are the interconnecting weights of the input data $a_i$, respectively, and $b_j$ is the bias for the neuron. The information is stored in the form of set of connection weights and biases. A transfer function $F$ through which the sum of weighted inputs with bias is processed and the output is given by Equation (2):

$$F(X) = u_j = F\left[ \sum_{i=1}^{n} w_{ij} a_i + b_j \right] \tag{2}$$

Hidden and output layers generally have a linear or non-linear activation/transfer function. There are many types of learning algorithms available to derive the input-output relationships. The most commonly used algorithm is the learning algorithms for feed forward back propagation [57-59]. The widely used nonlinear activation function is *sigmoid* function whose output lies between 0 and 1, and the *sigmoid* transfer function is given by:

$$F(X) = \frac{1}{1 + e^{-X}} \tag{3}$$

When values are resulted negative at input or output layer, then the *tansig* transfer function is used; which is expressed as:

$$F(X) = \frac{e^{X} - e^{-X}}{e^{X} + e^{-X}} \tag{4}$$

The model is trained in hidden layer, momentum variable, and transfer function with selected number of neurons. MLFFNN is the most common form of neural model to predict the efficiency of the solar thermal system.

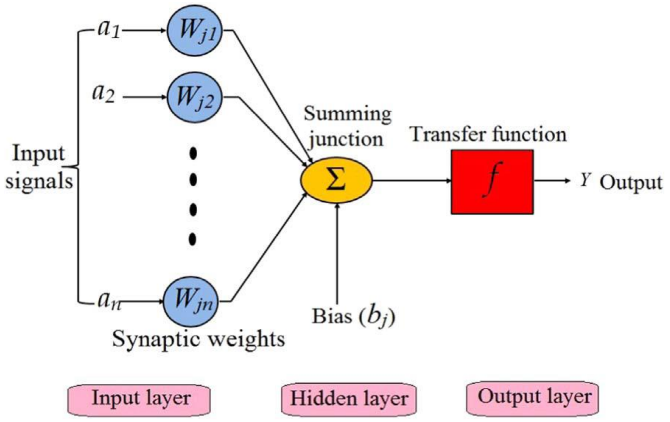


**Figure 3.** Basic structure of MLFFNN structure

## 2.2 Radial Basis Function (RBF)

There are also three layers in the RBF model: input layer, hidden layer and output layer. RBF model's primary structure is shown in Figure 4. This is identical to the MLFFNN model's three layers. RBF and MLFFNN, both models are feed forward neural network. In the RBF model, the signals are collected at the input layer and passed through the hidden layer of the second layer, which generates the output data [48, 49].

The hidden layer of RBF model is Radial basis activation function. The hidden layer's transfer function is normally a Gaussian function, which is expressed as [60, 62]:

$$a_j(x) = \exp\left(-\frac{\|x_i - c_j\|^2}{2\sigma_j^2}\right) \tag{5}$$

where, $\sigma_j$ is the width of the $j^{th}$ neuron, and $x_i$ and $c_j$ are the input and the center of RBF unit respectively. In Equation (6), $a_j$ is the notation for the output of the $j^{th}$ RBF unit.

$$y_k(x) = \sum_{j=1}^{n} w_{jk} a_j(x) + b_k \tag{6}$$

where, $b_k$ is the bias, $y_k$ is the $k^{th}$ output unit for the input vector $x$, $w_{jk}$ is the weight connection between the $k^{th}$ output unit and the $j^{th}$ hidden layer unit.

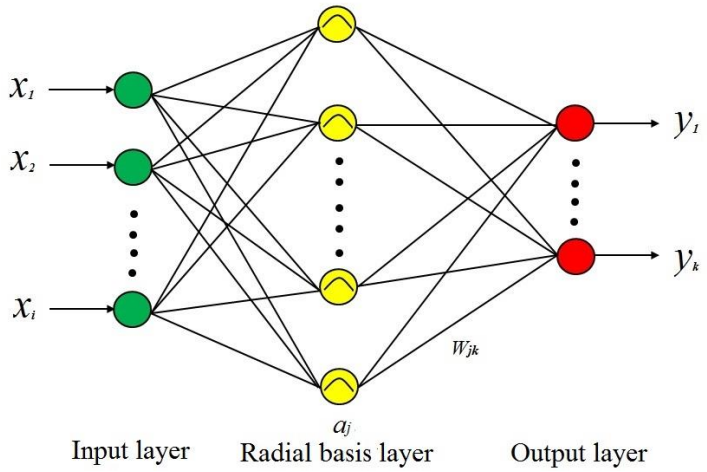


**Figure 4.** Basic design of RBF structure

## 2.3 General Regression Neural Network (GRNN)

Specht (1991) used the GRNN technique for the first time [71]. GRNN is a variant of the kernel regression network-based RBF architecture. In order to simulate the effects such as back propagation algorithms, this method does not need an iterative approach. It has its own capacity to approximate any arbitrary equation between vectors of input and output. [48, 49]. Generalized regression neural network (GRNN) technique is a probabilistic model between an independent (Input) and dependent (Output) variables. Figure 5 shows the basic structure of GRNN.

The structure shows that the GRNN model consist of four layers:

*Input layer*

The first layer is termed as input layer which is fully connected to the second layer. The number of input neurons at this layer depends on the total number of selected observation variables. This layer gathers information and the pattern layer is given.

*Pattern layer*

Pattern layer is used to perform clustering on the training process. Usually the number of pattern layer neurons is equal to the number of data sets of training pairs.

*Summation layer*

Summation layer contains two neurons, namely D Summation and S Summation neuron. These two neurons in the summation layer derive the underlying relation [71]:

$$D = \sum_{i=1}^{n} Y_i \exp\left( -\frac{\left(X - X_i\right)^T \left(X - X_i\right)}{2\sigma^2} \right) \tag{7}$$

$$S = \sum_{i=1}^{n} \exp\left( -\frac{\left(X - X_i\right)^T \left(X - X_i\right)}{2\sigma^2} \right) \tag{8}$$

*Output layer*

The fourth layer, *i.e.* the output layer, accomplishes normalization of output set by dividing the summation results in the summation layer. This results in the predicted value y to input vector x as below [48]:

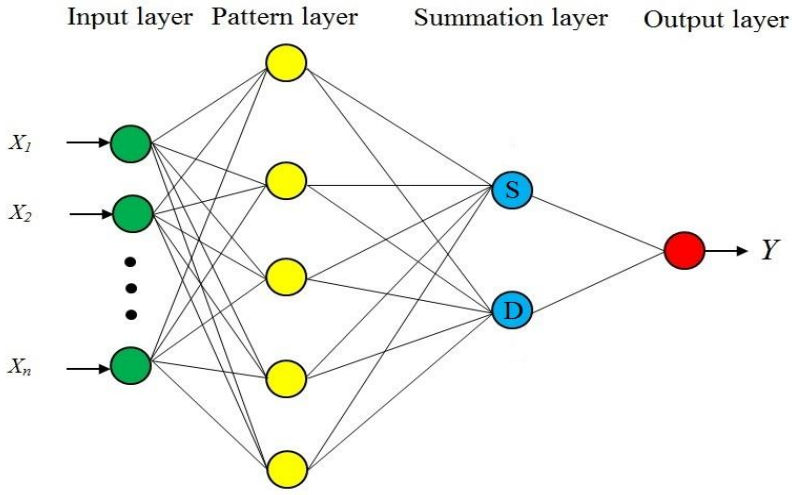


**Figure 5.** Basic structure of GRNN structure

$$Y(X)=\frac{D}{S}=\frac{\sum_{i=1}^{n}Y_i\ \exp\left(-\frac{(X-X_i)^T(X-X_i)}{2\sigma^2}\right)}{\sum_{i=1}^{n}\exp\left(-\frac{(X-X_i)^T(X-X_i)}{2\sigma^2}\right)} \tag{9}$$

## 3. Assessment Criteria for Model Performance

The neural model performance assessment is approved on the basis of the selection of minimum values of the errors of SSE, MSE, RMSE, MAE, MRE and COV. The least values of these errors indicate the most accurate value of ANN predicted results. In addition to this, the best fit of ANN predicted data with actual available data in terms of coefficient of determination ($R^2$) and correlation coefficient (R) are also considered as the selection criteria of model performance [71]. If the values of $R^2$ or R are proximate to unity, the predicted results are confirmed to be more accurate.

*Sum of square error*

$$SSE=\sum_{i=1}^{n}(X_{A,i}-X_{P,i})^2 \tag{10}$$

*Mean square error*

$$MSE=\frac{1}{n}\sum_{i=1}^{n}(X_{A,i}-X_{P,i})^2 \tag{11}$$

*Root mean square error*

$$RMSE=\sqrt{\frac{1}{n}\sum_{i=1}^{n}(X_{A,i}-X_{P,i})^2} \tag{12}$$

*Mean absolute error*

$$MAE=\frac{1}{n}\sum_{i=1}^{n}(X_{A,i}-X_{P,i}) \tag{13}$$

*Mean relative error %*

$$MRE=\frac{1}{n}\sum_{i=1}^{n}100\times\left(\frac{|X_{A,i}-Y_{P,i}|}{X_{A,i}}\right) \tag{14}$$

Coefficient of variance

$$COV=\frac{RMSE}{\frac{1}{n}\sum_{i=1}^{n}X_{P,i}}\times 100 \tag{15}$$

*Coefficient of determination*

$$R^2=1-\frac{\sum_{i=1}^{n}(X_{A,i}-X_{P,i})^2}{\sum_{i=1}^{n}X_{P,i}^2} \tag{16}$$

## 4. ANN Simulation Technique

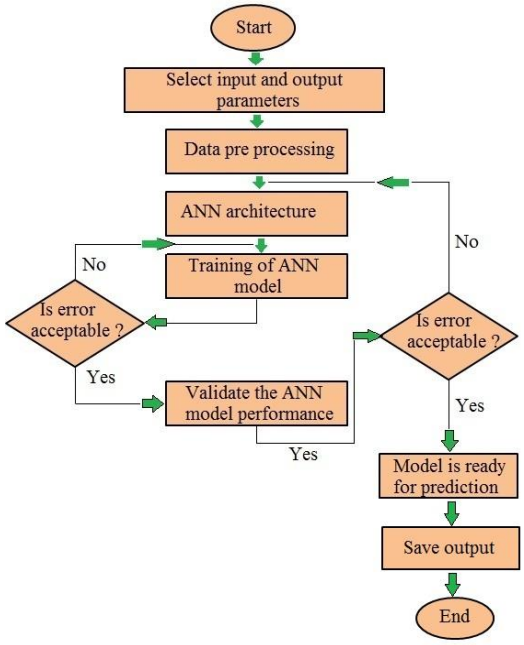


**Figure 6.** Basic steps flow chart of ANN simulation technique [71]

The basic steps of ANN simulation technique are shown in flow chart Figure 6. These important steps are followed in ANN prediction [5, 65].

1. In ANN technique, variables are selected at first.
2. Then data sets are collected by means of analytical and experimental procedure.
3. Data is pre-processed and set into input and output data sets.
4. Input data is divided into training, testing and validation sets.
5. Model is developed by training with standardized input data using different learning algorithms with different number of hidden layers neurons.
6. Based on statistical error analysis, model performance is checked.
7. Now ANN model is ready for prediction.
8. Finally, predicted data is extracted from the optimal model and correlated with actual data obtained through experiments.

## 5. Application of ANN Technique for Performance Prediction of Solar Thermal Systems

In the field of thermal engineering systems, the use of ANN methodology has been very widespread in the last two decades. Several researchers used ANN to model and forecast the thermal performance of solar thermal systems. Present paper explores the use of the ANN method to measure the thermal efficiency of different types of solar heating systems.

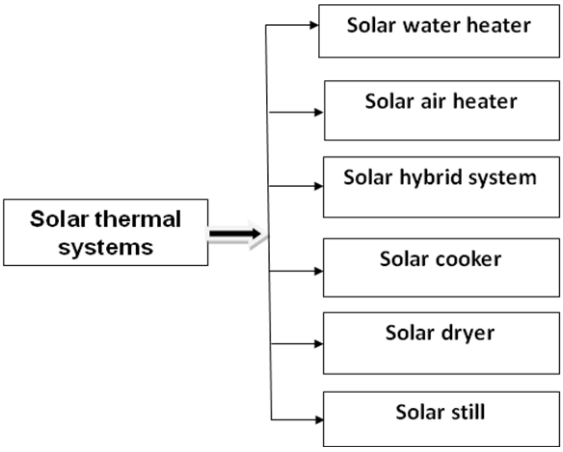


**Figure 7.** Literature review of different solar thermal systems (STS)

Figure 7 shows the classification of solar thermal systems used in the present work. Numerous research works have been carried out for performance prediction of these thermal systems with and without artificial computational techniques.

The important research works related to use of ANN modeling in the field of thermal energy systems are given below.

## 5.1 Performance prediction of solar water/ air heating systems using ANN

Kalogirou *et al.* [36] trained an artificial neural network (ANN) with minimum sets of input data for prediction of solar domestic water heating (SDWH) system's usable energy extraction and stored water temperature rise. He used 18-8-2 (3 hidden layers with 18 neurons) neural model of MLPNN network. For prediction of its performance, BP learning algorithm was used. The statistical $R^2$ value for training data set was obtained as 0.972 and 0.975 for two performance parameters.

Farkas *et al.* [37] used ANN model to predict the performance analysis of flat plate solar collector. The ANN model was constructed with three input parameters of solar intensity, ambient temperature and inlet air temperature, and in output layer single parameter with outlet temperature of air. In the hidden layer, 7 neurons with two layers were taken. Basically, ANN model was structured with FFBP network. For training of the model, LM learning algorithm was used. The tansig and purlin transfer functions were used in hidden and output layer, respectively. The generated data from Hottel-Vhillier (H-V) model and heat network model with measured data for 17 days were used in training process of the model. Finally, they predicted satisfactory results of output temperature of three different types of solar collector. They found that overall average deviation in outlet temperature of solar collector was 0.9°C.

Kalogirou [39] developed six ANN models to predict typical performance collector equation coefficients in both wind and no wind conditions, incidence angle multiplier coefficients in both longitudinal and transverse directions, collector time constant, collector heat capacity and collector temperature stagnation**.** Due to the different nature of the input and output needed in each case, different MLP networks of 3 and 4 layers of neural model were used. This work had helped design engineers, probably with a combination of different materials, to obtain the quality parameters of 'new' collector models without having to perform experiments.

Sozen *et al.* [40] used MLP network of 7-20-20-1 neural model to predict the thermal performance of solar flat plate collector (Figure 8). Author used logistic sigmoid transfer function and Ankara's summer session meteorological information (from July to September) as training data. The network input layer used surface temperature of collector, time, location, solar radiation, angle of decline, angle of tilt and angle of azimuth. The maximum and minimum deviations were found 2.5584 and 0.0019 at 27.2°C and 71.2°C surface temperatures, respectively.

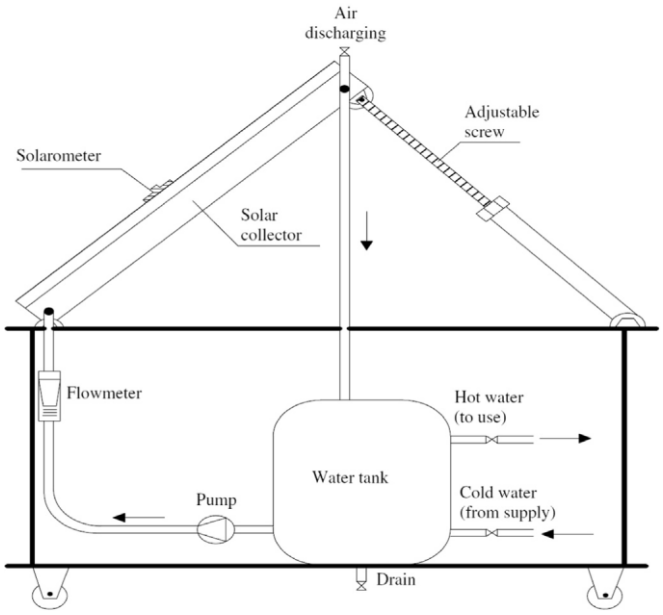


**Figure 8.** Experimental set up of solar water heater [40]

Xie *et al.* [42] also estimated the performance of solar collectors under the meteorological conditions of Beijing using ANN with BP learning algorithm and logistic sigmoid transfer function. For this, authors prepared an experimental setup as shown in Figure 9. In the input layer ambient temperature of collector, solar intensity, declination, tilt and azimuth angle were used along with efficiency and heating capacity for output. Results achieved that ANN of 5-10-10-2 system is the most suitable algorithm with peak correlation coefficient ($R^2$) as 0.9999, (RMSE) as 0.0075 and low variance coefficient (COV) as 0.3384. Results indicated that the ANN predicted precisely matched experimental value for output.

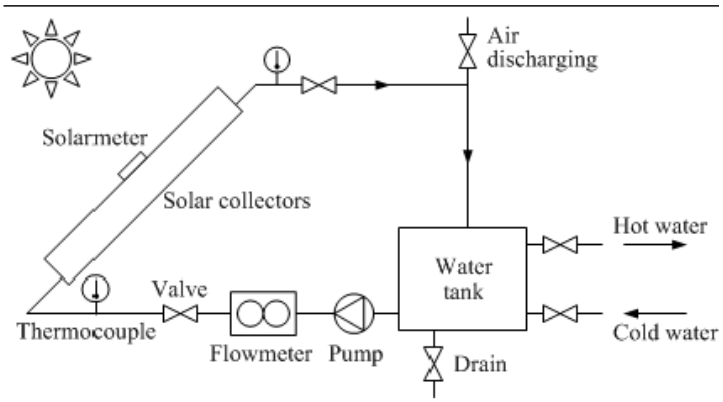


**Figure 9**. Experimental set up of the solar collector under the meteorological conditions of Beijing [42]

Varol *et al.* [43] experimentally measured the performance of the solar collector system using sodium carbonate decahydrate ($Na_2CO_3.10H_2O$) as a substrate for phase change material (PCM) and comparison of collector efficiency was done with conventional systems without PCM (Figure 10). Authors found that use of PCM increases collector efficiency; thus, large amounts of solar energy can be stored while the daytime and used after sunset for water heating. Also performed numerous predictions by using three different soft computing techniques as Artificial Neural Networks (ANN), Adaptive-Network-Based Fuzzy Inference System (ANFIS) and Support Vector Machines (SVM)and found that SVM technique give the best results than that of ANFIS and ANN.

**Figure 10**. Experimental set up of the solar collector system using sodium carbonate decahydrate as PCM [43]

Fischer *et al.* [45] reviewed that although the state-of-the-art approach for collector modelling and testing didn't fit for some designs (*e.g.*, "Sydney" tubes using heat pipes and "water-in-glass" collectors) which are difficult to model with the similar precision than conventional flat plate collectors. Hence authors carried out comparative performance measurements of flat plate and an evacuated "Sydney" tubular collector using NARX (Nonlinear Auto-Regressive model with exogenous inputs) architecture of ANN model. Researchers obtained results showed better agreement for the artificial

neural network (5-5-1 & 5-4-1 neural model) approach between measured and calculated collector output compared to state-of - the-art modelling.

Kalogirou *et al.* [47] structured neural model with 7–24-2 neurons for prediction of thermal performance of thermo-siphon solar water heating system. For this work, they collected 54 data sets, in which 46 were used for training and rest of 8 used for testing. With the use of learning algorithm ANN model was trained and predicted results with maximum deviations 1 MJ and 2.2 °C for two output parameters.

Esen *et al.* [50] had adopted ANN and WNN based methods for efficient modeling of SAH system. Efficiency of collector and air temperature were used as output parameters in those models. The proposed WNN method for 0.03 kg/s air mass flow rate was used to achieve efficiency/air temperature leaving values of 0.0094/0.0034 for RMSE, 0.9992/0.9994 for $R^2$ and 2.7955/2.4100 for COV values. For the air mass flow rate of 0.05 kg/s in the flow pipe, the collector efficiency/air temperature values are 0.0126/0.0058, 0.9992/0.9989 and 2.8047/3.9574. Authors found that WNN is reliable option for of SAH system efficiency prediction with satisfactory accuracy than that of the methods reported before.

Caner *et al.* [52] experimentally examined two types-zigzagged and flat absorber surface type of solar air collectors (Figure 11) with 40 sample data sets each for 5 days. Authors calculated thermal performance by using data obtained from experimental setup and designed ANN model for calculation of solar air collector thermal performances for comparison with predicted values. Researchers proposed that LM based MLP network of 8-20-1 neural model gave the best prediction results with 0.9967 errors by stepwise regression analysis.

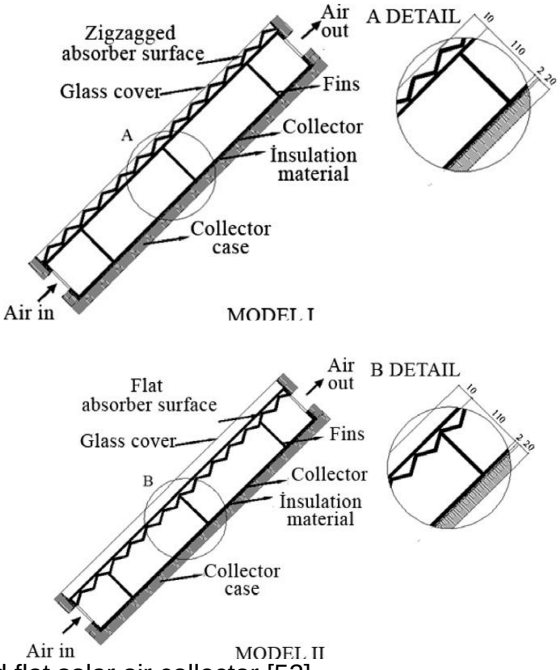


**Figure 11.** Zig-zaged and flat solar air collector [52]

Benli [54] applied ANN technique with 8-3-1 ANN system with LM learning algorithm to assess the SAH thermal efficiency of 2 different types (trapeze and corrugated shaped absorber plate). He had a maximum $R^2$ value of 99.71% for LM-3, a

minimum RMSE value of 4.18% for LM-3 for Type-I SAC and a maximum $R^2$value of 99.85% for LM-3 and a minimum RMSE value of 2.62% for LM-3 for Type-II SAC.

Hamdan *et al.* [55] developed a 5-20-5 neural ANN model of an unglazed flat-plate solar collector with air passing behind the absorbing plate to study the heat transfer. A NARX model estimated the mean indoor temperature at each solar collector surface and the heat given to the air flow. The results obtained were tested against the mathematical calculation used by the optimization technique to find the above values. Author found that the NARX model can be used for estimation of mean inside temperature at each surface of the flat-plate collector with coefficient of determination of 0.99997.

Kalogirou [67] used ANN method to predict the expected daily energy output for typical operating conditions, as well as the temperature level of large solar systems. For about 1 year (226 days) experimental measurements had been taken to estimate the ANN ability. Author found that 3-5-5-5-2 neural model of MLPNN network type with BP learning algorithm effectively predicts everyday system energy output (Q) and $Ts_{max}$ (Maximum water temperature in the storage tank at the end of the day). The statistical $R^2$-value obtained for the training and validation data sets was better than 0.95 and 0.96 for the two performance parameters, respectively.

Ghirtlahre and Prasad [56] have done prediction of thermal performance of unidirectional porous bed solar air heater. A process diagram of unidirectional flow SAH is shown in Figure 12. Authors used neural model to predict the performance of SAH using 4-5-3 neutral structure. They used in learning process four different types of transfer functions such as LM, CGP, SCG, and OSS. Authors concluded that trained LM training function are optimal transfer function for accurate prediction.

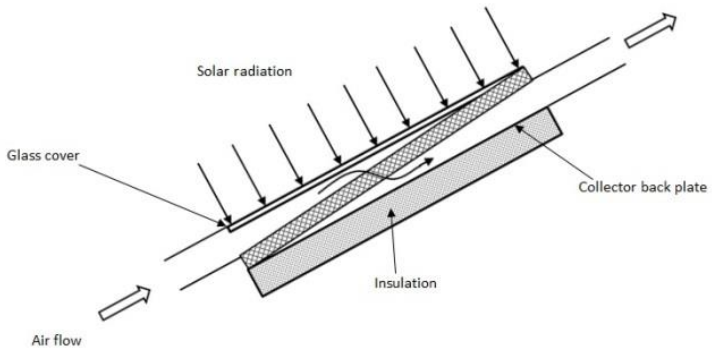


**Figure 12.** Unidirectional flow solar air heater [56]

Ghirtlahre and Prasad [62] have done exergetic performance prediction of SAH with different types of neural models as MLP, GRNN and RBF models of ANN technique. For that aim, they collected 210 data sets from experiments. They found that RBF model with 6-6-2 NN with LM training function is the best prediction model on basis of ANN analysis.

Ghirtlahre and Prasad [61] used two different types of ANN learning algorithms such as LM and SCG to estimate performance of roughened SAH. They found that the model 6-6-1 and 6-7-1 with LM and SCG learning algorithm respectively was optimal for prediction. They also concluded that the LM based ANN model was best model.

Ghritlahre and Prasad [65] developed feed forward neural network model to predict the energy and exergy efficiency of transverse wire rib roughened solar air heater. To achieve this aim, they collected 50 sets of experimental data and calculated values of energy and exergy efficiencies. They structured NN model with 6 input parameters and 2 output parameters. 4 to 7 numbers of neurons were used with LM and SCG learning algorithms for obtaining best model. It was found that the 6-6-2 neural model successfully predicted the data using LM learning algorithm.

Cetiner *et al.* [66] constructed an experimental setup of solar water heater (Figure 13), which consists of a cylindrical concentrator, an absorber, a heat exchanger, a pump, water storage and a control unit. Authors used MLP network of 4-7-3 neural model with LM learning algorithm to forecast system performance. Author executed a plot between easily measurable traits such as environmental conditions, input and output water temperatures, solar radiation and flow rate of hot water and obtained 40% system efficiency at power supplied of 18 kW maximum at noon and 6 kW minimum in the afternoon.


**Figure 13.** Experimental set up of solar hot water generator [66]

## 5.2 ANN Model for Performance Prediction of Solar Hybrid System (SHS)

Facao *et al.* [38] did the prediction of performance of two hybrid types solar air collectors (plate and tube heat pipe type) using ANN. Authors constructed MLPNN model of 8-9-1, 9-3-1, 9-6-1 neural model and 9-84-1 neural model of RBFNN to calculate the solar efficiency and useful heat gained. MLP configuration with 6 hidden neurons found to be an excellent alternative to calculate useful heat and thermal efficiency for both designs. The networks were trained using results from mathematical models generated by Monte Carlo simulation. Between the two neural models, MLPs performed slightly better than RBFs.

Kamthania and Tiwari [53] had used ANN very uniquely for performance evaluation (thermal energy, electrical energy, and overall exergy) of a semi-transparent hybrid photovoltaic thermal double pass air collector (Figure 14). That ANN model used 200 sets of data of ambient air temperature, global solar radiation, diffuse radiation and number of cloudless days as input parameters from 4 weather conditions (Srinagar, jodhpur, Mumbai and Bangalore) for training and the 5$^{th}$ weather station (New Delhi) data has been used for testing purpose. Author finally found that MLPNN model of LM algorithm with 15 neurons in the hidden layer is the most suitable algorithm with RMSE ranges from 0.10–2.23% for various output parameters.

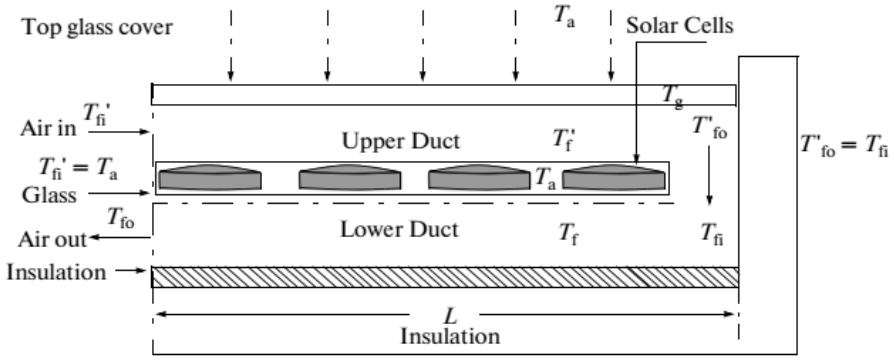


**Figure 14.** Hybrid PV/T double pass SAH [53]

Ammar *et al.* [46] proposed a PV/T (hybrid system) controlled algorithm based on ANN to detect the optimal power operating point (OPOP). The OPOP computes the optimum mass flow rate of PV/T for an acknowledged radiation and ambient temperature. Finally, the researchers constructed a FFNN network of 2-5-1 neural model for its estimation of OPOP of different mass flow rates at solar radiation (300-950 w/m$^2$) and corresponding ambient temperatures (5-35 °C). Model performance estimated by calculating the Normal Mean Bias Error (NMBE) was found to be -13.05%

## 5.3 ANN Model for Performance Prediction of Solar Dryers (SD)

Cakmak and Yildiz [51] developed a novel type of dryer (Figure 15) particularly included an expanded surface SAC, a solar air collector with PCM and drying room with swirl element and estimated the drying rate using nonlinear regression analysis at 3 different air velocities. Finally, authors estimated drying rate using FFNN and compared performance of this model with those nonlinear and linear regression models by RMSE, ME, and the correlation coefficient statistics. Based on error analysis results, authors achieved that 3-10-1 neural model of LM technique and hyperbolic tangent sigmoid activation function was the most suitable FNN configuration for transient drying rate prediction.

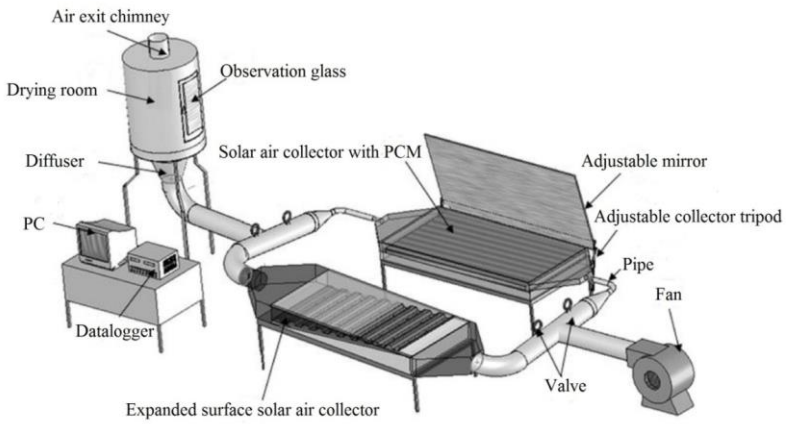


**Figure 15.** Complete Experimental set up of solar dryer [51]

Tripathy and Kumar [41] investigated application of ANN for prediction of temperature variation of food product (potato cylinders and slices) with experimental data of 9 typical days of different months in a year. Researchers prepared various MLP network models of SCG (scaled conjugate gradient), CGP (Polak-Ribiere conjugate gradient), BFGS quasi-newton and LM training algorithms with *logsig*, *tansig*, *poslin* and *satlin* transfer functions for comparative analysis of performance. An experimental setup of solar dryer is shown in Figure 16. Researchers also proposed an analytical heat diffusion model and a statistical model and concluded that 4 neurons (2-4-1) network of LOGSIG transfer function and TRAINRP back propagation algorithm were the best model with minimum error for potato slices and cylinder both.

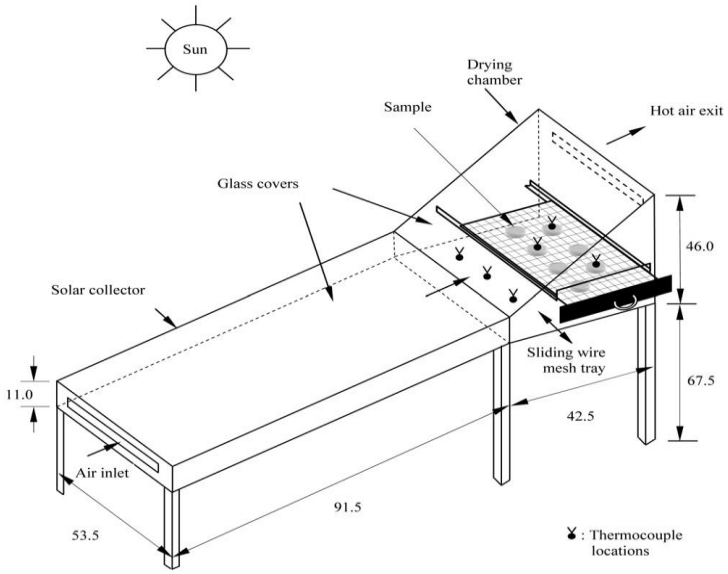


**Figure 16.** Experimental setup of solar dryer [41]

Nazghelichi *et al.* [44] did the energy and exergy prediction of carrot cubes in a fluidized air dryer by ANN. He conducted experiments with different air temperatures, bed width and square cubed dimensions and compiled total 518 data and determine energy and exergy of carrot cubes in fluidized bed dryer. By using these data, 4-30-4

ANN model was constructed and it successfully predicted energy and exergy with minimum error.

## 5.4 ANN Model for Performance Prediction of Solar Cookers (SC)

Kurt *et al.* [68] successfully predicted thermal performance of the experimentally investigated box type solar cooker including parameters such as enclosure air ($T_a$), absorber plate temp ($T_p$), and pot water temperatures ($T_w$) by using the ANN for the very first time. Cross section of that solar cooker is presented below in Figure 17. Authors used 126 experimental data sets, *i.e.* 96 for training/learning and 30 for validation of network performance. Researchers concluded that 5-10-3 neural model of FFNN of BP algorithm showed the best prediction results with the correlation coefficients ranging between 0.9950–0.9987 and MREs ranging 3.925–7.040 %.

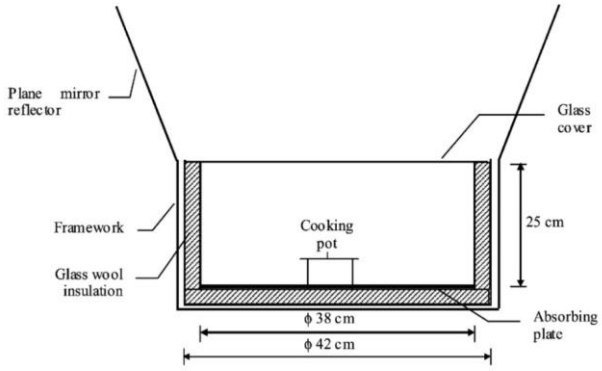


**Figure 17.** Cross section of solar cooker [68]

## 5.5 ANN Model for Performance Prediction of Solar Stills (SS)

Mashaly *et al.* [69] determined the modelling feasibility instantaneous thermal efficiency ($\dot{\eta}_{ith}$) of a solar still by using weather and operational data with MLP neural network and multiple linear regressions (MLR). Authors used nine variables as input parameters: Julian day, ambient temperature, relative humidity, wind speed, solar radiation, temperature of feed and brine water, total dissolved solids of feed water and brine water for both models. Performance evaluation revealed that COD for MLP model was 11.23% higher than for the MLR model. The average value of RMSE for the MLP model (2.74%) was lower compared to the MLR model.

Hidouri *et al.* [70] had determined performance of single slop hybrid solar still integrated with heat pump (SSDHP) by experimental study and compared with suitable ANN model. Authors evaluated the effect of an air compressor on productivity of SSDHP and predicted ANN models for different combination of most influential parameters (the solar radiation, glass cover temperature, basin temperature, water temperature and temperature of the evaporator). Authors concluded that SSDHP with air was recorded 33.33% higher yield as compared to the SSDHP without air. For training, validation, test and all, value of R was found equal to 0.99454, 0.99121, 0.99974 and 0.99374, respectively, in ANN's proposed model which shows very good agreement with the experimental result.

**Table 1.** Summary report of literature survey on application of ANN technique used in solar thermal systems

| S. No. | Authors | Year | System Used | Neural Model | Network Type | Learning Algorithm | Work carried out/ Result |
|---|---|---|---|---|---|---|---|
| 1. | Kalogirou *et al.* [36] | 1999 | Solar domestic water heater | 8-18-2 | MLPNN | BP | Found statistical $R^2$ value approx. 0.97 |
| 2. | Kalogirou *et al.* [47] | 1999 | Solar water heater | 7-24-2 | MLPNN | BP | Found maximum deviations of 1 MJ and 2.2°C. |
| 3. | Cetiner *et al.* [66] | 2005 | Solar water heater | 4-7-3 | MLPNN | LM | Obtained 40% system efficiency at power supplied of 18kW max. and 6kW min. at noon |
| 4. | Farkas *et al.* [37] | 2003 | Flat plate solar collector | 3-7-1 | MLPNN | TRAINLM | Found 3-7-1 MLP network for optimal performance analysis. |
| 5. | Facao *et al.* [38] | 2004 | Hybrid solar collector / heat pipe system | ANN: 8-9-1, 9-3-1, RBF: 9-84-1 | MLPNN RBFNN | BP, RBF | Found MLP better than RBF |
| 6. | Kalogirou [39] | 2006 | Flat plate solar collector | Six models | MLPNN | BP | Found ANN fast and precise than conventional methods |
| 7. | Sozen *et al.* [40] | 2008 | Flat plate solar collector | 7-20-20-1 | MLPNN | BP | Collected experimental data from July to September for constructing ANN model with **7**-20-20-1 neurons |
| 8. | Esen *et al.* [50] | 2009 | Double flow SAH | 6-4-2, 6-5-2 | ANN, WNN | ANN: LM, SCG, CGP WNN: LM | WNN model found best compared to ANN model |
| 9. | Kurt *et al.* [68] | 2007 | Solar cooker | 5-10-3 | FFNN | BP | $R^2$ ranging 0.9950–0.9987 and MREs ranging 3.925–7.040% |
| 10. | Tripathy and Kumar [41] | 2009 | Solar air dryer | 2-4-1 | MLPNN | SCG, CGP,LM, RP,BFG | Found 2-4-1 TRAINRP model as most appropriate |
| 11. | Xie *et al.* [42] | 2009 | Solar collector | 5-10-10-2 | MLPNN | BP | Results found as $R^2$=0.999, RMSE=0.0075, COV=0.3384 |

| | | | | | | | |
|---|---|---|---|---|---|---|---|
| 12. | Varol *et al.* [43] | 2010 | Solar collector (phase change material) | 5-7-1 | MLPNN | LM | SVM > ANFIS, ANN |
| 13. | Caner *et al.* [52] | 2011 | zigzag and flat absorber surface SAH | 8-20-1 | MLPNN | LM | Found 8-20-1 best neuron model of LM learning algorithms |
| 14. | Nazgheli-Chi *et al.* [44] | 2011 | Fluidized bed solar dryer | 4-30-4 | MLPNN | LM | Found 4-30-4 ANN model prediction with min error |
| 15. | Kamthania *et al.* [53] | 2012 | hybrid PV/T double pass air collector | 4-15-4 | MLPNN | LM | Taken input parameters from 4 weather conditions for training and 5th weather station data used for testing. |
| 16. | Fischer *et al.* [45] | 2012 | Flat plate and Sydney tubular solar collector | 5-5-1, 5-4-1 | NARX | LM | Used conventional flat plate and an evacuated "Sydney" tubular collector. |
| 17. | Benli [54] | 2013 | Corrugated and trapeze shaped collector SAH | 8-3-1 | MLPNN | LM | Used 8-3-1 ANN model with LM training algorithm |
| 18. | Ammar *et al.* [46] | 2013 | Hybrid PV/T SAH | 2-5-1 | FFNN | LM | Found NMBE to be -13.05% for OPOP estimation |
| 19. | Hamdan *et al.* [55] | 2014 | Flat plate solar air collector (unglazed) | 5-20-5 | NARX | Rprop | Concluded with a NARX model with $R^2$ values as 0.99997 |
| 20. | Kalogirou *et al.* [67] | 2014 | Solar air collector | 3-5-5-5-2 | MLPNN | BP | Found $R^2$ values for training & validation = 0.95 & 0.96 |
| 21. | Ghritlahre and Prasad [56] | 2017 | Porous bed solar air heater | 4-5-3 | MLPNN | LM, CGP, SCG, and OSS | Found 4-5-3 LM model as optimal transfer function with min. error |
| 22. | Ghritlahre and Prasad [60] | 2018 | Porous bed solar air heater (unidirectional flow) | 6-6-2 | MNP, GRNN, RBF | LM | Observed RBF model is best wrt MLP and GRNN for exergy prediction $R^2$ as 0.9999 |
| 23. | Ghritlahre and Prasad [61] | 2018 | Transverse wire rib roughened SAH | 6-6-1 6-7-1 | MLPNN | LM, SCG | Found 6-6-1 LM based ANN model as optimal wrt 6-7-1 SCG model |
| 24. | Mashaly *et al.* [69] | 2016 | Hybrid Solar Still | 9-12-1 | MLP MLR | LM | RMSE for MLP model (2.74%) was lower compared to the MLR model |

| | | | | | | | |
|---|---|---|---|---|---|---|---|
| 25. | Cakmak and Yildiz [51] | 2011 | Solar Dryer | 3-10-1 | FFNN | LM | Predicted drying rate using optimal model with 3-10-1 |

## 6. Suggestions for Future Research

It is reviewed above that many researchers have done performance prediction of different types of solar thermal systems successfully by applying ANN. Although researchers had approached almost every type of solar thermal systems for implementation of ANN and suggested to utilize it as more efficient, simple and speedy tool than conventional computational methods for designing and performance prediction; there are still many aspects untouched. Some potential points that can be carried forward for further research are pointed below:

(i) Researchers had used different input parameters for performance prediction of solar thermal systems, but the relevant input parameters are not classified yet.
(ii) Comparative analysis of ANN modeling with conventional approach like SVM, RSM, GA and MLR has not been done.
(iii) Hybrid technology like GA with ANN has not been used effectively.
(iv) Very limited number of training algorithms has been used for ANN modeling.
(v) The numbers of neurons in hidden layer can be estimated by various formulas to predict the best results which are given by various researchers [63, 64].
(vi) By the use of SA approach ANN model may be optimized.
(vii) Neural models can be optimized by ANT colony algorithm.

## 7. CONCLUSION

In this paper, a comprehensive review has been carried out for performance prediction of different solar thermal systems using ANN technique. This review covers performance prediction of various solar thermal systems like solar air heater, solar cooker, solar dryer, solar stills, solar water heater and solar hybrid systems through different ANN modeling (MLP, RBF, GRNN, NARX and WNN) and different learning algorithms (LM, SCG, CGP, OSS) successfully presented by previous researchers. It is outlined by most of the researchers that ANN is potentially superior for modeling of these devices due to its high accuracy, simplicity and short computing time with respect to other modeling techniques.

This paper will genuinely help the future researchers to overview the work concisely related to solar thermal system performance prediction using various types of ANN models and learning algorithm and compare it with other global methods of machine learning.

## CONFLICTS OF INTEREST

The authors declare that there is no conflict of interests regarding the publication of this review article.

## REFERENCES


[1] Sukhatme, S.P., Nayak, J.K. (1996). *Solar Energy: Principles of thermal collection and storage*. Tata McGraw Hill, New Delhi.

[2] Garg, H.P., Prakash, J. (2006). *Solar energy fundamentals and applications*, Tata McGraw Hill publishing Co. Ltd.

[3] Duffie, J.A., Beckman, W.A. (2006). *Solar Engineering of Thermal Processes, third ed*. Wiley Inter science, New York.

[4] Goswami, D.Y. (2015). *Principles of Solar Engineering, third ed.*, CRC Press, Taylor & Francis Group.

[5] Haykin, S. (1994). *Neural networks: a comprehensive foundation*. New York: Macmillan.

[6] Gardner, M.W., Dorling, S.R. (1998). Artificial Neural Networks (The Multilayer Perceptron): a review of applications in the atmospheric sciences. *Atmos. Env.,* 32: 2627-2636.

[7] Hussain, M.A. (1999). Review of the applications of neural networks in chemical process control- simulation and online implementation. *Artif. Intell. Eng.*, 13: 55-68.

[8] Kalogirou, S.A. (2000). Applications of artificial neural networks for energy systems. *Appl. Energy*, 67: 17-35.

[9] Kalogirou, S.A. (2001). Artificial neural networks in renewable energy systems applications: a review. *Renew. Sustain. Energy Rev.*, 5: 373-401.

[10] Kalogirou, S.A. (2003). Artificial intelligence for the modeling and control of combustion processes: a review. *Progress in Energy and Combustion Science*, 29(6): 515-566.

[11] Mellit, A., Kalogirou, S.A. (2008). Artificial intelligence techniques for photovoltaic applications: a review. *Prog. Energy Combust. Sci.*, 34: 574-632.

[12] Yang, K.T. (2008). Artificial neural networks (ANNs): A new paradigm for thermal science and engineering. *ASME J. Heat Transf.*, 130(9): 093001-5–093001-19

[13] Mellit, A., Kalogirou, S.A., Hontoria, L., Shaarid, S. (2009). Artificial intelligence techniques for sizing photovoltaic systems: A review. *Renewable and Sustainable Energy Reviews,* 13(2): 406-419.

[14] Mohanraj, M., Jayaraj, S., Muraleedharan, C. (2012). Applications of artificial neural networks for refrigeration, air-conditioning and heat pump systems—a review. *Renew Sustain Energy Rev,* 16: 1340–58.

[15] Cong, T., Su, G., Qiu, S., Tian, W. (2013). Applications of ANN in fluid flow and heat transfer problems in nuclear engineering: a review work. *Prog Nucl Energy,* 62:54–71.

[16] Karabacak, K., Cetin, N. (2014). Artificial neural networks for controlling wind–PV power systems: a review. *Renew Sustain Energy Rev,* 29:804–27.

[17] Yadav, A.K., Chandel, S.S. (2014). Solar radiation prediction using Artificial Neural Network techniques: a review. *Renew Sustain Energy Rev,* 33: 772–81.

[18] Mohanraj, M., Jayaraj, S., Muraleedharan, C. (2015*).* Applications of artificial neural networks for thermal analysis of heat exchangers- A review. *International Journal of Thermal Sciences*, 90: 150-172.

[19] Ata, R. (2015). *Artificial neural networks applications in wind energy systems: a review*. *Renewable and Sustainable Energy Reviews*, 49: 534–562.

[20] Qazi, A., Fayaz, H., Wadi, A., Raj, R.G., Rahim, N.A., Khan, W.A. (2015*)*. The artificial neural network for solar radiation prediction and designing solar systems: a systematic literature review. *J Clean Prod;* 104:1–12

[21] Zahraee, S.M., Assadi, M.K., Saidur, R. (2016). Application of Artificial Intelligence Methods for Hybrid Energy System Optimization. *Renew Sustain Energy Rev*, 66: 617–30.

[22] Jani, D.B., Mishra, M., Sahoo, P.K. (2017). Application of artificial neural network for predicting performance of solid desiccant cooling systems – a review. *Renew Sustain Energy Rev*, 80: 352–66.

[23] Ghritlahre, H.K., Prasad, R.K. (2018). Application of ANN technique to predict the performance of solar collector systems – a review. *Renew Sustain Energy Rev*, 84: 75–88.

[24] Pacheco-Vega, A., Sen, M., Yang, K.T., McClain, R.L. (2001). Neural network analysis of an-tube refrigerating heat exchanger with limited experimental data. *International Journal of Heat and Mass Transfer*, 44: 763–70.

[25] Arcaklioglu, E., Erisen, A., Yilmaz, R. (2004). Artificial neural network analysis of heat pumps using refrigerant mixtures. *Energy Conversion Management*, 45 (11-12): 1917–1929.

[26] Abbassi, A., Bahar, L. (2005). Application of neural network for the modeling and control of evaporative condenser cooling load. *Applied Thermal Engineering* , 25 (17-18): 3176–86.

[27] Yigit, K.S., Ertunc, H.M. (2006). Prediction of the air temperature and humidity at the outlet of a cooling coil using neural networks. *International Communications in Heat and Mass Transfer*, 33: 898–907.

[28] Hosoz, M.H., Ertunc, M. (2006). Modeling of a cascade refrigeration system using artificial neural networks. *International Journal of Energy Research*, 30: 1200–15.

[29] Ertunc, H.M., Hosoz, M. (2006). Artificial neural network analysis of a refrigeration system with an evaporative condenser. *Applied Thermal Engineering*, 26: 627–35.

[30] Movagharnejad, K., Nikzad, M. (2007). Modeling of tomato drying using artificial neural network. *Computers and electronics in agriculture*, 59: 78-85.

[31] Hosoz, M., Ertunc, H.M., Bulgurcu, H. (2007). Performance prediction of a cooling tower using artificial neural network. *Energy Conversion and Management*, 48: 1349–59.

[32] Hosoz, M., Ertun, H.M., Ozguc, A.F. (2008). Modelling of a direct evaporative air cooler using artificial neural network. *International Journal of Energy Research*, 32: 83–89.

[33] Sanaye, S., Dehghandokht, M., Beigi, M.H., Bahrami, S. (2011). Modeling of rotary vane compressor applying artificial neural network. *International Journal of Refrigeration*, 34:764–772.

[34] Jani, D.B., Mishra, M., Sahoo, P.K. (2016). Performance prediction of solid desiccant - vapor compression hybrid air-conditioning system using artificial neural network. *Energy* ,103: 618-629.

[35] Jani, D.B., Mishra, M., Sahoo, P.K. (2016). Performance prediction of rotary solid desiccant dehumidifier in hybrid air-conditioning system using artificial neural network. *Applied Thermal Engineering*, 98:1091-1103.

[36] Kalogirou, S.A., Sophia, P., Argiris, D. (1999). Modeling of solar domestic water heating system using artificial neural network. *Solar energy,* 65; 335-342.

[37] Farkas, I., Geczy Vig., P. (2003). Neural network modeling of flat plate solar collectors. *Computers and Electronics in Agriculture*, 40 (1–3): 87-102.

[38] Facao, J., Varga, S., Oliviera, A. (2004). Evaluation of the Use of Artificial Neural Networks for the Simulation of Hybrid Solar Collectors. *International journal of green energy*, 1(3): 337-352.

[39] Kalogirou, S.A. (2006). Prediction of flat plate collector performance parameters using ANN. *Solar energy*, 80 (3): 248-259.

[40] Sozen, A., Menlik, T., Unvar, S. (2008). Determination of efficiency of flat plate solar collector using ANN approach, *Expert system with applications*, 35: 1533-1539. DOI: 10.1016/j.eswa.2007.08.080

[41] Tripathy, P., Kumar, S. (2009). ANN approach for food temp. prediction during solar drying. *International journal of thermal sciences*, 48 : 1452-1459.

[42] Xie, H., Lui, L., Ma, F., Fan, H, (2009). Performance prediction of solar collectors using artificial neural networks. DOI: 10.1109/AICI.2009.344

[43] Varol, Y., Koca, A., Oztop, H., Avci, E. (2010). Forecasting of thermal energy storage performance of phase change material in a solar collector using soft computing technique. *Expert Systems with Applications*, 37(4): 2724–2732.

[44] Nazghelichi, T., Aghbaslo, M., Kianmehr, M., Omid, M. (2011). Prediction of energy and exergy of carrot cubes in a fluidized bed dryer by ANN. *Drying technology: An international journal*, 29(3): 295-307.

[45] Fischer, S., Frey, P., Druck, H. (2012). A comparison between state of the art and neural network modeling of solar collectors. *Solar Energy*, 86: 3268–3277.

[46] Ammar, M., Chaabene, M., Chtourou, Z. (2013). ANN based control for PV/T to track optimum thermal and electrical power. *Energy Conversion and Management* 65: 372–380.

[47] Kalogirou, S.A. Panteliou, S., Dentsoras, A. (1999). Artificial neural network used for performance prediction of thermosiphon solar water heater. *Renewable energy* 18: 87-99.

[48] Kisi, O., Tombul, M., Kermani, M.Z. (2014). Modeling soil temperatures at different depths by using three different neural computing techniques. *Theoretical and Applied Climatology*, 121(1–2): 377–387.

[49] Wang, L., Kisi, O., Kermani, M.Z., Salazar, G.A., Zhu, Z., Gong, W. (2016). Solar radiation prediction using different techniques: model evaluation and comparison. *Renewable and Sustainable Energy Reviews*, 61: 384-397.

[50] Esen, H., Ozgen, F., Esen, M., Sengur, A. (2009). Artificial neural network and wavelet neural network approaches for modeling of a solar air heater. *Expert Systems with Applications*, 36:11240–11248.

[51] Cakmak, G., Yıldız, C. (2011). The prediction of seedy grape drying rate using a neural network method. *Computers and Electronics in Agriculture*, 75 :132–138.

[52] Caner, M., Gedik, E., Keçebas, A. (2011). Investigation on thermal performance calculation of two type solar air collectors using artificial neural network. *Expert Systems with Application*s, 38:1668–1674.

[53] Kamthania, D., Tiwari, G.N. (2012). Performance Analysis of a Hybrid Photovoltaic Thermal Double Pass Air Collector Using ANN. *Applied Solar Energy*, 48(3): 186–192.

[54] Benli, H. (2013). Determination of thermal performance calculation of two different types of solar air collectors with the use of artificial neural networks. *International Journal of Heat and Mass Transfer*, 60: 1–7.
[55] Hamdan, M.A., Abdelhafez, E.A., HajKhalil, R.A. (2014). Heat Transfer Analysis of a Flat-Plate Solar Air Collector by Using an Artificial Neural Network. *J. Infrastruct. Syst.*, doi/abs/10.1061/(ASCE)IS.1943-555X.0000213
[56] Ghritlahre, H.K., Prasad, R.K. (2017). Prediction of thermal performance of unidirectional flow porous bed solar air heater with optimal training function using Artificial Neural Network. *Energy Procedia*, 109:369 – 376.
[57] Ghritlahre, H.K., Prasad, R.K. (2017). Energetic and exergetic performance prediction of roughened solar air heater using artificial neural network. *Ciência e TécnicaVitivinícola*, 32 (11): 2-24.
[58] Ghritlahre, H.K., Prasad, R.K. (2018). Investigation on heat transfer characteristics of roughened solar air heater using ANN technique. *International Journal of Heat and Technology*, 36 (1): 102-110.
[59] Ghritlahre, H.K., Prasad, R.K. (2018). Exergetic Performance Prediction of roughened Solar Air Heater Using Artificial Neural Network. *Strojniškivestnik - Journal of Mechanical Engineering*, 64 (3):195–206.
[60] Ghritlahre, H.K., Prasad, R.K. (2018). Investigation of thermal performance of unidirectional flow porous bed solar air heater using MLP, GRNN, and RBF models of ANN technique. *Thermal Science and Engineering Progress*, 6: 226-235. DOI: 10.1016/j.tsep.2018.04.006
[61] Ghritlahre, H.K., Prasad, R.K. (2018). Development of Optimal ANN Model to Estimate the Thermal Performance of Roughened Solar Air Heater Using Two Different Learning Algorithms. *Annals of Data Science*, 5(3):453–467.
[62] Ghritlahre, H.K., Prasad, R.K. (2018). Exergetic performance prediction of solar air heater using MLP, GRNN and RBF models of artificial neural network technique. *Journal of Environmental Management*, 223: 566-575.
[63] Witten, I.H., Frank, E. (2005). Data mining: Practical machine learning tools and techniques, Morgan Kaufmann, San Francisco, CA: 560.
[64] Shibata, K., Ikeda, Y. (2009). Effect of number of hidden neurons on learning in large-scale layered neural networks. *In Proceedings of the ICROS-SICE International Joint Conference*: 5008–5013.
[65] Ghritlahre, H.K. (2018). Development of feed-forward back-propagation neural model to predict the energy and exergy analysis of solar air heater. *Trends Renew Energy*, 4:213–235. DOI: 10.17737/tre.2018.4.2.0078
[66] Cetiner, C., Halici, F., Cacur, H., Taymaz, I. (2005). Generating hot water by solar energy and application of neural network. *Applied Thermal Engineering*, 25 :1337–1348.
[67] Kalogirou, S.A, (2014). Artificial neural networks for the performance prediction of large solar systems. *Renewable Energy*, 63: 90-97.
[68] Kurt, H., Atik, K., Ozkaymak, M., Recebli, Z. (2008). Thermal performance parameters estimation hot box type solar cooker by using ANN. *International Journal of Thermal Sciences*, 47: 192–200.
[69] Mashaly, A., Alazba, A. (2016). MLP and MLR models for instantaneous thermal efficiency prediction of solar still under hyper-arid environment. *Computers and Electronics in Agriculture*, 122: 146–155.

[70] Hidouri, K., Mishra, D., Benhmidini, A., Chouachi, B. (2017). Experimental and theoretical evaluation of a hybrid solar still integrated with an air compressor using ANN. *Desalination and Water Treatment*, 88: 52–59. DOI:10.5004/dwt.2017.21333

[71] Ghritlahre, H.K., Chandrakar, P., Ahmad, A. (2019). A comprehensive review on performance prediction of solar air heater using ANN. *Annals of data science*, doi:10.1007/s40745-019-00236-1.

[72] Ghritlahre, H.K., Prasad, R.K. (2018). Prediction of exergetic efficiency of arc shaped wire roughened solar air heater using ANN model. *Int J Heat Technol*, 36(3):1107–1115.

[73] Ghritlahre, H.K., Prasad, R.K. (2018). Prediction of heat transfer of two different types of roughened solar air heater using Artificial Neural Network technique. Thermal Science and Engineering Progress, 8: 145-153. DOI:10.1016/j.tsep.2018.08.014



Trends in Renewable Energy
OPEN ACCESS ISSN: 2376-2144
Peer-Reviewed Article futureenergysp.com/index.php/tre

# A Comprehensive Study on Re-arrangement of Modules Based TCT Configurations of Partial Shaded PV Array with Shade Dispersion Method

V. Bala Raju, Dr. Ch. Chengaiah

*Dept. of EEE, SVU College of Engg., SV University, Tirupati, India*

Received December 23, 2019; Accepted January 29, 2020; Published February 12, 2020

The conventional Total-Cross-Tied (TCT) Solar photovoltaic (SPV) array configuration has the highest power output as compared to other configurations or topologies in most cases of partial shading. But the performance of TCT configuration is affected under shading conditions, resulting in multiple peaks occurring in the output PV characteristics. To improve the performance of TCT array configuration under different shading scenarios, it is only necessary to reposition or rearrange the PV modules in the TCT Solar PV array based on the arrangement of puzzle numbers, without altering the electrical contacts of the TCT array configuration. The main objective of this study is to investigate the performance of rearrangement of modules in SPV array based new TCT array configurations with shade dispersion technique and compare the global maximum peak power (GMPP) of SPV array, mismatch losses, Fill-Factor, efficiency and number of required electrical connections or ties between array modules with proposed optimal arrangement of modules under shading (non-uniform irradiance) conditions. For this study, one uniform irradiance case and total 14 partial shading patterns were considered. MATLAB/Simulink software was used for modeling and simulation of 6×6 size different rearrangement based TCT array and proposed optimal SPV array configurations.

*Keywords: Photovoltaic cells and modules; Array output power; Interconnections; Mismatch power losses; Fill-factor; Efficiency; Partial shading*

## 1. Introduction

The freely available irradiance in the atmosphere is directly converted into electricity through the photovoltaic (PV) effect with the help of solar photovoltaic (SPV) cells in a PV module. The freely available solar energy is used for different applications in our daily life. The first solar photovoltaic cell was developed in 1954 with a very low efficiency of 5% which has now reached up to 25%. The efficiency of PV modules gradually reduced to a lower value of less than 10%, because of partial shading effect in an array [1-4]. The performance of a SPV array under shading conditions can be improved by means of reconfiguration methods. The main conventional PV array configurations are parallel, series, series-parallel(S-P), Honeycomb (HC), bridge linked (BL) and total cross-tied (TCT) type [5-6] of connections. Among all conventional type, the TCT has the highest power output and minimum mismatch losses under various shading scenarios as presented in the literature [6-8]. The main I-V characteristic

*Corresponding author: vbrajuu@gmail.com

Tr Ren Energy, 2020, Vol.6, No.1, 37-60. doi: 10.17737/tre.2020.6.1.00111

parameters are $V_{oc}$, $V_m$, $I_{sc}$, $I_m$ and $P_m$. The factors including manufacturer tolerance, uneven surface soiling, light-induced power degradation, discoloration and cracking are responsible for the I-V mismatch (differences of I-V parameters of PV modules in the SPV array) in modules, which causes mismatch losses in the SPV array and typically 4% to 7% energy loss. The performance of the TCT configuration is improved under shading conditions by repositioning or rearrangement of the modules based on puzzle patterns in an array configuration. In the TCT configuration based on number puzzles, the arrangement of modules mainly includes Sudoku, Arrow Sudoku, Ken-Ken, Skyscrapers, Non-symmetric, Chaotic-Based-Map, Odd-Even, Futoshiki, Latin square, Magic square, current based arrangement ($I_m$ based TCT) and voltage based arrangement ($V_m$ based TCT) photovoltaic configurations [8-10]. Based on the shading pattern, the optimal location of each module in the TCT SPV array is determined with the help of puzzle number analysis without modifying the electrical interconnections among the modules. In this article, the various rearrangement methods used for enhancing the maximum power of the SPV array under shaded conditions presented in the literature are analyzed, and the parameters such as global maximum power (PGMPP), mismatch losses (mmlosses), fill-factor (FF) and efficiency are compared. This paper proposes an optimal interconnection for a 6×6 size TCT array configuration under 14 different possible shading scenarios. Compared to S-P and rearrangement-based TCT SPV array connections, the proposed optimal interconnection technique minimizes the requirement of number of electrical interconnections or ties among modules and also reduces mismatched power losses. The optimal method proposed creates an alternative path for current distribution between modules under unshaded and partially shaded conditions with minimum number of interconnections or ties. The performance of the TCT array topology is improved by rearrangement of modules to the optimal location, but wiring losses increase due to repositioning of every module in an entire array configuration. The proposed method minimizes the installation cost, requirement of wires, wiring installation time and complexity of interconnections among modules as compared to rearrangement modules based TCT configurations of the SPV system. The output array power of the optimal method is nearly same as rearranged based TCT configuration by considering wiring losses of repositioning modules in an array.

## 2. System Design

### 2.1 Mathematical Modelling of Solar PV Cell and Array

The solar PV cell converts solar PV energy into electrical energy. Figure 1 shows the equivalent circuit of a single diode PV cell and symbol of PV cell.

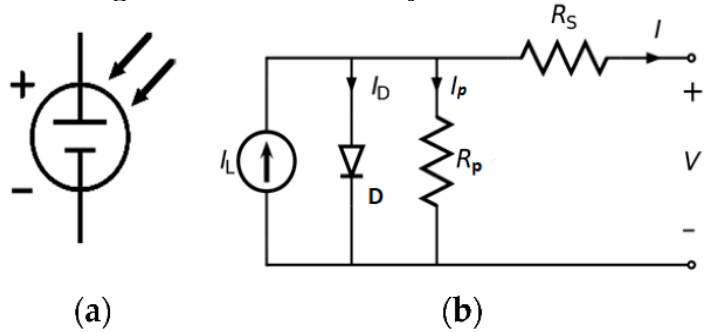


**Figure 1.** Modeling of solar PV cell: (a) symbol (b) equivalent circuit of a PV cell

The mathematical representation of the solar photovoltaic cell is given by in Equation1 [11].

$$\mathbf{I = I_L - I_{RS}\left[\exp\left\{\frac{q(V + IR_S)}{V_{Th}\, a}\right\} - 1\right] - \frac{(V + IR_S)}{R_P}} \quad \ldots\ldots\ldots\ldots (1)$$

Where ***V*** and ***I*** are the solar PV cell voltage and current respectively. $I_L$ is the photo generated current of the PV module and represented as

$$\boldsymbol{I_L = \frac{G}{G_0}[I_{LSTC} + K_{isc}(T_c - T_{STC})]} \quad \ldots\ldots\ldots\ldots (2)$$

$K_{isc}$ is the module short-circuit co-efficient. $I_{LSTC}$ is the module light generated current at standard test conditions (STC). G is the incident irradiation and $G_0$ is standard irradiation. $T_c$ and $T_{STC}$ are the actual and STC temperatures in Kelvin.

The PV array consists of $\mathbf{N_P}$ and $\mathbf{N_S}$ number of PV modules that are connected in parallel and series, respectively, is shown in Figure 2.

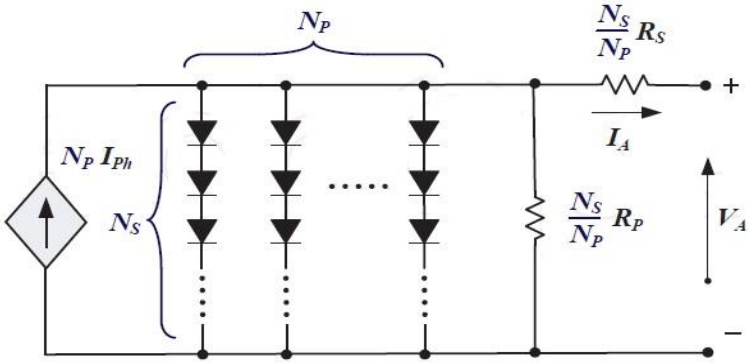


**Figure 2.** Solar PV array with number of modules

The PV array current is mathematically represented in Equation 3[12].

$$\mathbf{I_A = I_{ph}N_P - I_{RS}N_P\left[\exp\left(\frac{q\left(V_A + R_S\left(\frac{N_S}{N_P}\right)I_A\right)}{V_{Th}\, a}\right) - 1\right] - \left[\frac{V_A + R_S\left(\frac{N_S}{N_P}\right)I_A}{R_P\left(\frac{N_S}{N_P}\right)}\right]} \ldots\ldots (3)$$

where $I_A$: array current; $V_A$: array voltage [V]; $I_{ph}$ and $I_{RS}$ are solar cell photo current[A] and diode reverse saturation current [A], respectively; $R_S$ and $R_P$ are series and parallel resistances[Ω], respectively; A: Diode ideality factor (value 1 to 5); $V_{Th}$: cell thermal voltage [V] as $V_{Th}=kT_C/q$; $T_C$: solar cell absolute operating temperature [K]; q: electron charge [$1.602\times10^{-19}$ coulombs]; k: Boltzmann's constant [$91.38065e^{-23}$ J/K].

The simple 6×6 size PV plant with series-parallel (SP) connection is shown in Figure 3. Each string consists of 6 (M) series connection modules and connects 6 number of strings (N) in parallel to form a SP configuration.

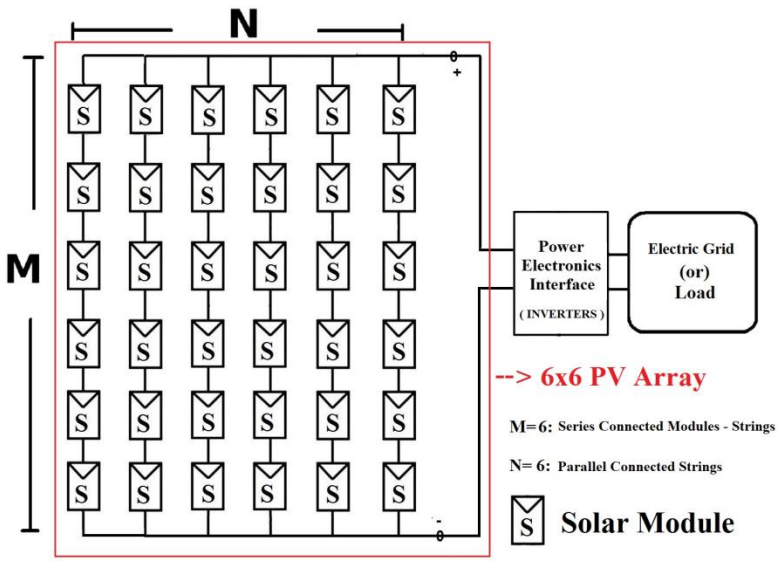


**Figure 3.** Simple 6 x 6 size series-parallel connection type PV Plant

Solar PV array configuration is formed by number of modules connected in parallel and series [12-13]. $V_{\mathbf{m}}$ and $I_{\mathbf{m}}$ are the un-shaded SPV module voltage and current, respectively. If the **n** number of modules are connected in series, the current through series modules is the same, but the voltage across the array is the sum of individual module voltages. In series connection, the total power is calculated by Equation 4,

$$\left.\begin{aligned} I_{\text{array}} = I_{\text{string}} = I_{\text{m1}} = I_{\text{m2}} = \cdots = I_{\text{mn}} = I_{\text{m}} \\ V_{\text{array}} = V_{\text{m1}} + V_{\text{m2}} + V_{\text{m3}} + \cdots + V_{\text{mn}} = nV_{\text{m}} \\ P_{array} = nV_m I_m \end{aligned}\right\} \quad \text{---- (4)}$$

When the SPV modules are connected in parallel, the voltage across each module is the same, but the total current of array is the sum of currents of each module. In parallel connection, the total power is calculated by Equation 5,

$$\left.\begin{aligned} V_{\text{array}} = V_{\text{m1}} = V_{\text{m2}} = \cdots = V_{\text{mn}} = V_{\text{m}} \\ I_{\text{array}} = I_{\text{m1}} + I_{\text{m2}} + \cdots + I_{\text{mn}} = nI_{\text{m}} \\ P_{\text{array}} = nV_{\text{m}} I_{\text{m}} \end{aligned}\right\} \quad \text{---- (5)}$$

The current and voltage of the SPV array for $i^{th}$ row and $j^{th}$ column (i × j = n) in array configuration are given by Equation 6.

$$\left.\begin{aligned} I_{\text{array}} = jI_{\text{m}} \\ V_{\text{array}} = iV_{\text{m}} \\ P_{\text{array}} = (\text{i x j})\, V_{\text{m}} I_{\text{m}} = n\, V_{\text{m}} I_{\text{m}} \end{aligned}\right\} \quad \text{---- (6)}$$

The power will be reduced, when all modules in the SPV array configuration are uniformly shaded with shading factor $S_f$. The array power is given by Equation 7,

$$P_{\text{array}} = S_{\text{f}} \text{ x } n \text{ x } V_{\text{m}} \text{x } I_{\text{m}} \quad \text{---- (7)}$$

## 2.2 Specifications of Solar PV Module

In this paper, in order to model and simulate different rearranged based SPV array configurations, the Vikram Solar ELDORA 270 PV module available in MATLAB/ Simulink is considered. The PV module specifications under STC (1000 W/m$^2$ and 25°C) are tabulated in Table 1.

**Table 1.** Specifications of Vikram Solar ELDORA 270 module

| Parameters | | Values |
|---|---|---|
| Maximum Power | | 270 W |
| Cells per module | $N_{cell}$ | 72 |
| Open circuit voltage | $V_{OC}$ | 44 V |
| Short-circuit current | $I_{SC}$ | 8.1A |
| Voltage at maximum power point | $V_{MP}$ | 34.7 V |
| Current at maximum power point | $I_{MP}$ | 7.8A |
| Temperature coefficient of | $V_{oc}$ | -0.3583% /°C |
| Temperature coefficient of | $I_{sc}$ | 0.024975%/°C |
| Light generated current | $I_L$ | 8.1924 A |
| Diode saturation current | $I_o$ | 2.4871e-10 |
| Diode ideality factor | | 0.98223 |
| Shunt resistance | $R_{sh}$ | 3126.5623 Ω |
| Series resistance | $R_s$ | 0.52303 Ω |
| Module Area (LxWxH) mm | | 1955x982x36 |

## 2.3 Solar Photovoltaic Array Configurations

The main conventional configurations or topologies based on type of connections of PV modules in SPV array are classified as:

a. Series (S) connection type configuration
b. Parallel (P) connection type configuration
c. Series-Parallel (S-P) connection type configuration
d. Bridge-Linked (B-L) connection type configuration
e. Honey-Comb (H-C) connection type configuration
f. Total-Cross-Tied (TCT) connection type configuration

In the series connection type, all modules are connected in series. In the parallel connection type, all modules are connected in parallel as shown in Figure 3. The S and P type of connections are not suitable for applications, because high currents exist in the parallel type and high voltages in the series type [14-15]. In the SP connection, series connected modules known as strings are connected in parallel. In the TCT type of connection, ties are connected among modules to get more power. The formation of different types of SPV array topologies from photovoltaic cell to array configurations is shown in Figure 4.

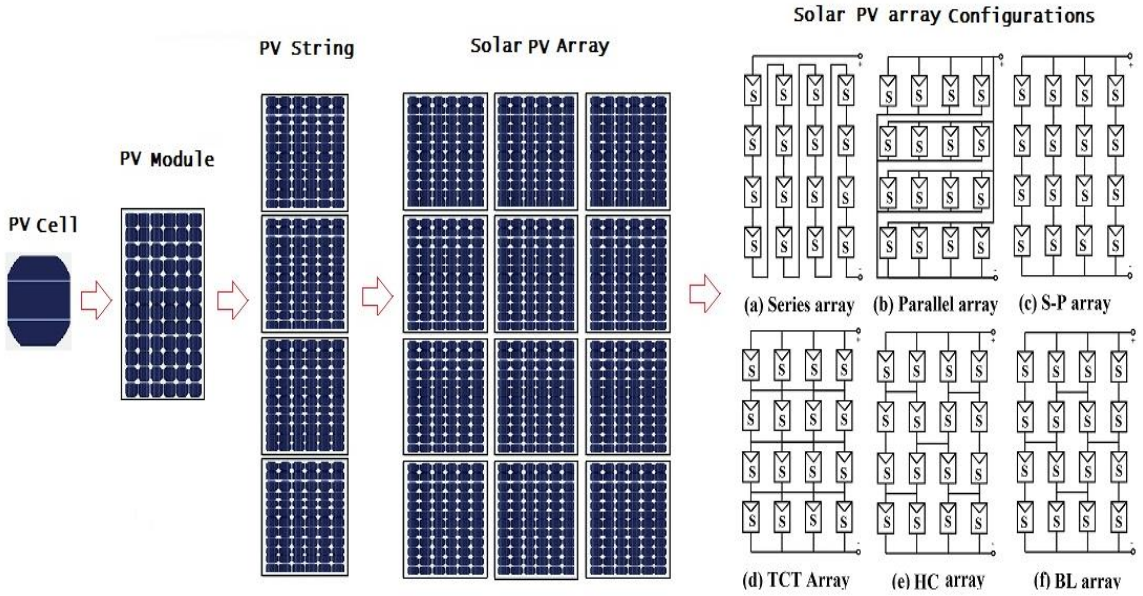


**Figure 4.** Formation of 4×4 size solar PV array topologies

## 2.4 Rearrangement of SPV modules based Total Cross Tied (TCT) configurations:

The modules in each row and column of TCT topologies are rearranged for enhancing the output power of the SPV array. Based on the rearrangement of modules, the TCT topologies are classified into,

*i. Su-Do-Ku based TCT configuration*
*ii. Arrow Su-Do-Ku based TCT configuration*
*iii. Ken Ken- TCT configuration*
*iv. Skyscrapers- TCT configuration*
*v. Non-Symmetric TCT configuration*
*vi. Chaotic Baker Map (CBM)-TCT configuration*
*vii. Odd-Even TCT configuration*
*viii. Futoshiki – TCT configuration*
*ix. Latin Square-TCT configuration*
*x. Magic square-TCT configuration*
*xi. Current based (Im based) TCT configuration*
*xii. Voltage based (Vm based) TCT configuration*

The above module re-arrangements in a 6×6 SPV array are based on the puzzle pattern arrangement. In this method, the electrical contacts of modules in the SPV array configuration are un-changed and repositioning the existing modules to new place according to puzzle-based numbers [6-10]. The performance of TCT configuration under this rearranged method is improved compared to conventional TCT configuration.

*Proposed Optimal Configuration*

The proposed optimal interconnection topology for the TCT array is developed from the connection switch (CS= 0 or 1) method as explained in Section 3.1. In this proposed method, the electrical connections between modules in SPV array

configurations are minimized. These interconnections are based on the shading pattern in the array configuration.

## 3. Proposed Optimal TCT Array Configuration

### 3.1 Methodology

In the proposed optimal interconnections among modules, the entire PV array system (any PV plant has a capacity of few KW to MW) is sub-divided into a small 2×2 size SPV sub arrays. The simulation results of a 2×2 sub array with tie connection switch (TCS=0/1) analysis [11], *i.e.*, if tie connection (tie) or interconnection is present means TCS=1 or absent means TCS=0, among the PV modules under seven possible shading cases for irradiances 500 W/m$^2$ and 700 W/m$^2$ are tabulated in Table 2. Figure 5 shows the PV modules S1, S2, S3 and S4 of 2×2 sub array with possible shading cases [11].

In Case I, all modules receive a constant solar irradiance of 1000 W/m$^2$ and the maximum power generated with tie connection and without tie connection is 6676 W. So, a tie connection is required. In Case II, the irradiance of module S1 is 500 W/m$^2$ and S2, S3, S4 modules receive an irradiance of 1000 W/m$^2$. Under this case the array power without tie connection is less than that with tie connection, so a tie is required among modules. In Cases III, IV and V, two modules are shaded as shown in Figure-5. If the two modules are shaded in horizontal (S1, S2) or vertical (S1, S3) positions in four positions, the array output power is the same, so tie is not required. If the diagonally connected modules are shaded, a tie between the SPV modules is required for the maximum array power. In Case VI: modules S1, S2 and S3 are shaded and module S4 is un-shaded. The output power of 2×2 array with tie connection is higher than that without tie connection, so a tie is required. In Case VII: all four modules are shaded and the power of SPV array with and without tie is the same, so a tie connection is not required among the modules.

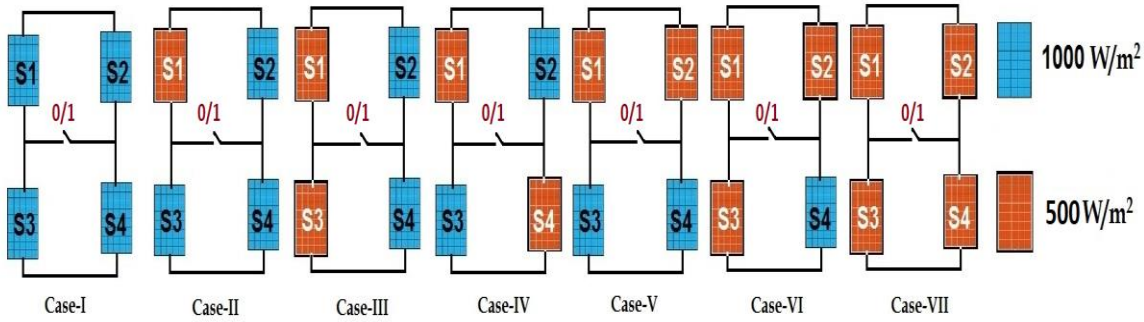


**Figure 5.** Possible shaded cases for 2×2 PV array

In Cases I, III, V and VII, the array power is equal in with and without the tie connection, so the tie is not required. But in Cases II, IV, VI, the global maximum power of the SPV array with a tie connection is higher than that without a tie connection. In this condition, a tie connection is required among modules for maximizing power. According to the above cases, it can be concluded that the power output of the SPV array depends on the location of number of shaded modules in an array configuration. In most cases, the requirement of a tie among SPV modules in the proposed optimal method is less and the number of electrical connections among the modules is minimized. From Table 2, it is concluded that the tie among the modules in an array is required for one shaded module,

two diagonally shaded modules or three shaded modules cases, while the interconnection or tie is not necessary among modules for other cases.

**Table 2.** Maximum powers for different irradiance levels

| Case | Shadow type | Maximum Power $P_m$(W) of shaded modules of irradiance 500 W/m² | | Maximum Power $P_m$(W) of shaded modules of irradiance 700 W/m² | | Tie Required (Yes/No) |
|---|---|---|---|---|---|---|
| | | CS=0 | CS=1 | CS=0 | CS=1 | |
| I | No Shade | 1062 | 1062 | 1062 | 1062 | No |
| II | One shaded module | 815 | **851.5** | 930.2 | **948.4** | **Yes** |
| III | Two shaded modules in Series | 801.6 | 801.6 | 908.1 | 908.1 | No |
| IV | Two diagonally shaded modules | 589.8 | **801.6** | 804.3 | **908.1** | **Yes** |
| V | Two shaded modules in Parallel | 589.8 | 589.8 | 804.3 | 804.3 | No |
| VI | Three Shaded module | 560.6 | **579.2** | 776.9 | **790.9** | **Yes** |
| VII | All modules are shaded | 542.7 | 542.7 | 755.3 | 755.3 | No |

## **3.2** Modeling of Optimal Interconnection Configuration for Shading Case 9 and Case 14

In this section, the modeling of 6×6 size solar PV array configurations by the proposed optimal interconnection method are presented.

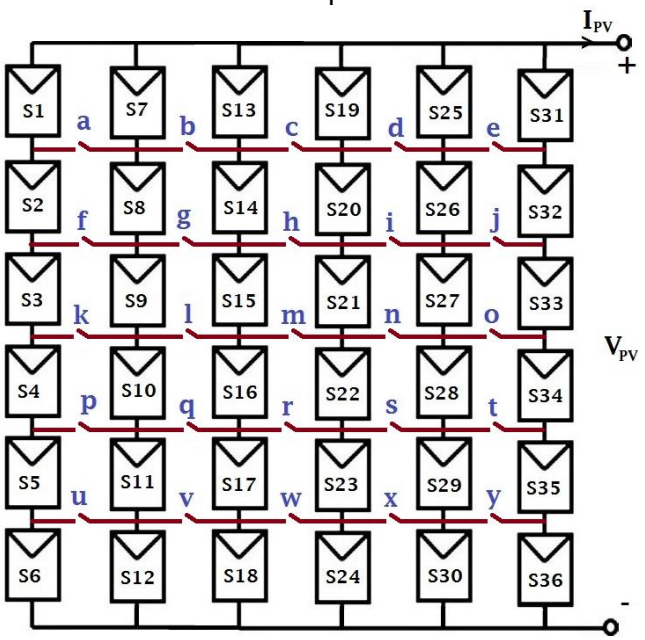


**Figure 6.** 6×6 size solar S-P PV array with interconnections among modules

In the proposed method, the entire 6×6 size PV array is sub-divided into a small number of 2×2 arrays, and the number of electrical connections, *i.e.*, interconnections required for connection of modules in an array configuration, is developed with the concept of proposed tie connection switch (TCS) method as described in Figure 6 in Section 3.1. TCS=1 means a tie connection present and TCS=0 means a tie connection absent between SPV array modules. The a, b, c, d, e, f, g, h, i, j, k, l, m, n, o, p, q, r, s, t, u, v, w, x and y are the proposed interconnections/ties among the modules in the 6×6 size PV array system. The number of inter-connections required in the SP configuration is 0, while the number of interconnects required in the TCT array configuration is a maximum

of 25. In the proposed optimal topology, it depends on the number of shaded modules in the SPV array configuration. If the shaded modules in a 2×2 sub array are one, diagonally shaded two modules or three shaded modules, the tie/ interconnection required. In other cases, *i.e.*, two shaded modules either horizontally shaded or vertically shaded, all four modules shaded or all four modules unshaded conditions, the tie is not required. This method reduces the wiring losses and wiring cost at the time of installation. The array output power of the proposed optimal topology is higher than that of the SP configuration and less than that of the TCT topology. By considering the wiring losses of rearranged based TCT configurations, the power output of proposed optimal configuration method is almost equal to that of the TCT configuration. The different partial shading cases (1 to 14) and uniform case-U are shown in Figure 7. The number of interconnections in SP, re-arranged based TCT and optimal TCT configurations for cases 9 and 14 are tabulated in Table 3 and for all cases 1 to 14 are tabulated in Table 4.

**Table 3.** Optimal interconnection results for cases 9 and 14

| Configurations | Interconnections/ Ties between PV Modules in 6x6 Array | | | | | | | | | | | | | | | | | | | | | | | | |
|---|---|---|---|---|---|---|---|---|---|---|---|---|---|---|---|---|---|---|---|---|---|---|---|---|---|
| | a | b | c | d | e | f | g | h | i | j | k | l | m | n | o | p | q | r | s | t | u | v | w | x | y | Total |
| SP | 0 | 0 | 0 | 0 | 0 | 0 | 0 | 0 | 0 | 0 | 0 | 0 | 0 | 0 | 0 | 0 | 0 | 0 | 0 | 0 | 0 | 0 | 0 | 0 | 0 | 0 |
| TCT/Sudoku/Arrow Sudoku/ Ken-ken/ Skyscrapers/ NS/ CBM/Odd-Even/ Futoshiki/LS/MS/ Im / Vm based TCT | 1 | 1 | 1 | 1 | 1 | 1 | 1 | 1 | 1 | 1 | 1 | 1 | 1 | 1 | 1 | 1 | 1 | 1 | 1 | 1 | 1 | 1 | 1 | 1 | 1 | 25 |
| Optimal TCT | | | | | | | | | | | | | | | | | | | | | | | | | | |
| For Case-9 | 1 | 0 | 0 | 0 | 1 | 0 | 0 | 0 | 0 | 0 | 0 | 0 | 0 | 0 | 0 | 0 | 0 | 0 | 0 | 0 | 1 | 0 | 0 | 0 | 1 | 04 |
| For Case-14 | 1 | 1 | 0 | 0 | 0 | 0 | 1 | 1 | 0 | 0 | 0 | 0 | 1 | 1 | 0 | 0 | 0 | 0 | 1 | 1 | 0 | 0 | 0 | 0 | 1 | 09 |

**Table 4.** Optimal interconnection results for different cases

| Cases | Interconnections/ Ties between PV Modules in 6x6 Array | | | | | | | | | | | | | | | | | | | | | | | | |
|---|---|---|---|---|---|---|---|---|---|---|---|---|---|---|---|---|---|---|---|---|---|---|---|---|---|
| | a | b | c | d | e | f | g | h | i | j | k | l | m | n | o | p | q | r | s | t | u | v | w | x | y | Total |
| U | 0 | 0 | 0 | 0 | 0 | 0 | 0 | 0 | 0 | 0 | 0 | 0 | 0 | 0 | 0 | 0 | 0 | 0 | 0 | 0 | 0 | 0 | 0 | 0 | 0 | 0 |
| 1 | 0 | 0 | 0 | 0 | 0 | 0 | 0 | 0 | 0 | 0 | 0 | 0 | 0 | 0 | 0 | 0 | 0 | 0 | 0 | 0 | 0 | 0 | 0 | 0 | 0 | 0 |
| 2 | 0 | 0 | 0 | 0 | 0 | 0 | 0 | 0 | 0 | 0 | 0 | 0 | 0 | 0 | 0 | 0 | 0 | 0 | 0 | 0 | 0 | 0 | 0 | 0 | 0 | 0 |
| 3 | 0 | 1 | 1 | 1 | 0 | 1 | 0 | 1 | 1 | 1 | 1 | 1 | 0 | 0 | 0 | 0 | 1 | 1 | 1 | 1 | 1 | 1 | 1 | 1 | 0 | 17 |
| 4 | 1 | 1 | 0 | 0 | 0 | 1 | 1 | 1 | 0 | 0 | 0 | 1 | 1 | 1 | 0 | 0 | 0 | 1 | 1 | 1 | 0 | 0 | 0 | 1 | 1 | 13 |
| 5 | 0 | 0 | 0 | 0 | 0 | 1 | 1 | 0 | 0 | 0 | 1 | 0 | 0 | 0 | 0 | 0 | 0 | 0 | 0 | 0 | 0 | 0 | 0 | 0 | 0 | 03 |
| 6 | 0 | 0 | 0 | 0 | 0 | 0 | 1 | 1 | 0 | 0 | 0 | 0 | 0 | 0 | 0 | 0 | 0 | 0 | 0 | 0 | 0 | 1 | 0 | 0 | 0 | 03 |
| 7 | 0 | 0 | 0 | 0 | 0 | 0 | 0 | 0 | 0 | 0 | 0 | 1 | 0 | 0 | 0 | 0 | 1 | 0 | 0 | 0 | 0 | 0 | 0 | 0 | 0 | 02 |
| 8 | 0 | 0 | 0 | 0 | 0 | 0 | 0 | 0 | 0 | 0 | 0 | 1 | 0 | 0 | 0 | 0 | 0 | 0 | 0 | 0 | 0 | 0 | 0 | 0 | 0 | 01 |
| 9 | 1 | 0 | 0 | 0 | 1 | 0 | 0 | 0 | 0 | 0 | 0 | 0 | 0 | 0 | 0 | 0 | 0 | 0 | 0 | 0 | 1 | 0 | 0 | 0 | 1 | 04 |
| 10 | 1 | 0 | 0 | 0 | 1 | 0 | 0 | 0 | 0 | 0 | 0 | 0 | 0 | 0 | 0 | 0 | 0 | 0 | 0 | 0 | 1 | 0 | 0 | 0 | 1 | 04 |
| 11 | 0 | 0 | 0 | 0 | 0 | 0 | 0 | 0 | 0 | 0 | 0 | 0 | 0 | 0 | 0 | 0 | 0 | 0 | 0 | 0 | 0 | 0 | 0 | 0 | 0 | 0 |
| 12 | 1 | 1 | 0 | 1 | 1 | 1 | 1 | 0 | 1 | 1 | 0 | 0 | 0 | 0 | 0 | 1 | 1 | 0 | 1 | 1 | 1 | 1 | 0 | 1 | 1 | 16 |
| 13 | 1 | 0 | 0 | 0 | 0 | 0 | 0 | 0 | 0 | 0 | 0 | 0 | 0 | 0 | 0 | 0 | 0 | 0 | 0 | 0 | 0 | 0 | 0 | 0 | 0 | 01 |
| 14 | 1 | 1 | 0 | 0 | 0 | 0 | 1 | 1 | 0 | 0 | 0 | 0 | 1 | 1 | 0 | 0 | 0 | 0 | 1 | 1 | 0 | 0 | 0 | 0 | 1 | 09 |

## 3.3 Partial Shaded Photovoltaic Array

The irradiance received by an SPV array is less than 1000 W/m$^2$, *i.e.*, non-uniform irradiance due to the shading effect. The main reason for shading is due to changes in tilt angles of modules, shading nearby buildings, clouds, bird litters, falling tree leaves on modules, and dust formed on modules because of pollution. In this work, for the performance analysis of 6×6 size re-arrangement based TCT SPV array configurations and proposed optimal TCT configurations, total fourteen partial shading

scenarios and one uniform case-U are considered, and the results including global maximum peak array power, shading losses, fill-factor, efficiency and number of ties required among modules in SPV array configurations are compared. Figure 7 shows the different irradiance values for partial shaded photovoltaic array for cases 1 to 14.

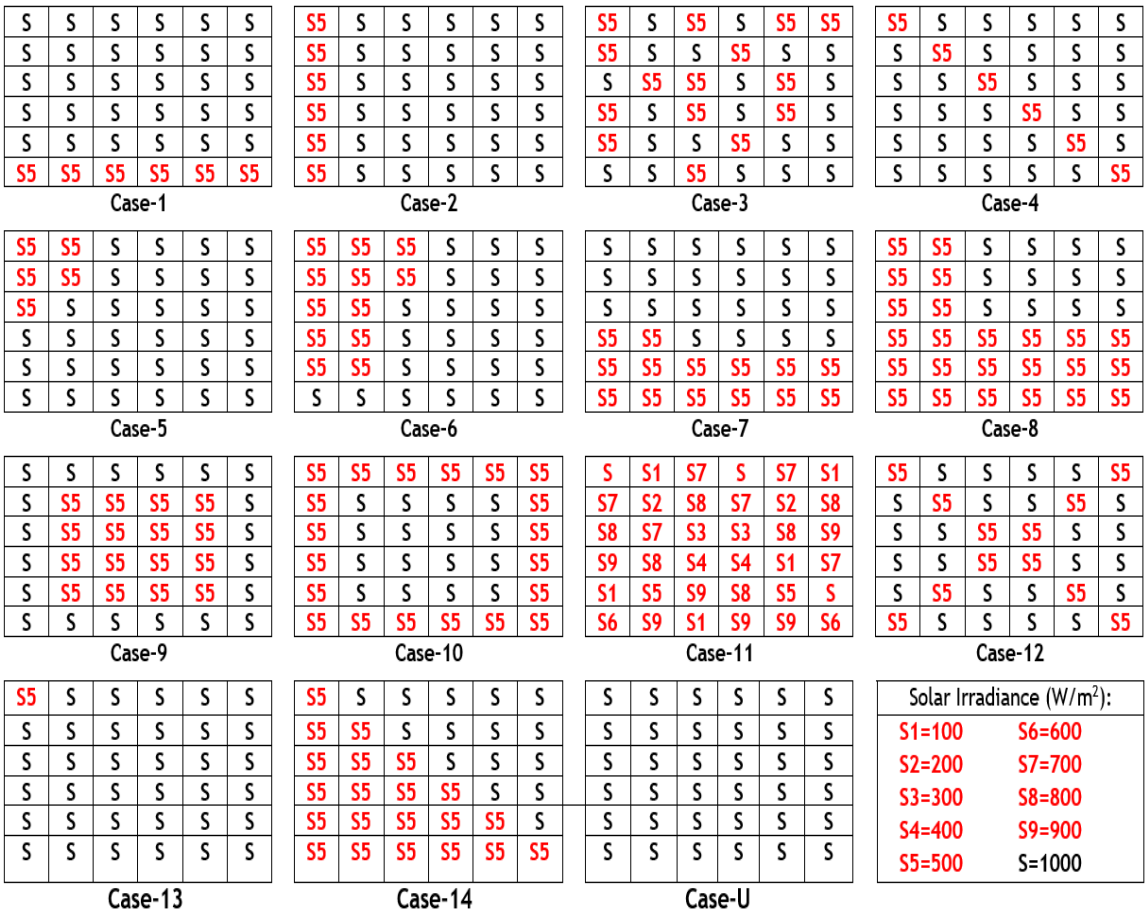


**Figure 7.** Proposed partial shading cases for 6×6 SPV TCT array configurations

## 4. Modeling and Simulation of Re-arrangement of Solar PV Modules Based TCT Configurations

### 4.1 Rearrangement of Modules in 6×6 TCT Solar PV Array

As shown in Figure 8, the photovoltaic modules are arranged in row and column wise for a 6×6 size conventional TCT array configuration. The number 11 indicates 1st row and 1st column, 12 indicates 1st row and 2nd column and similarly for 66 means 6th row and 6th column. In SP,TCT and optimal TCT type of configurations the modules doesn't change their positions in an SPV array, whereas in remaining rearranged based TCT array configurations the position of modules is rearranged based on the puzzle number pattern. In this rearrangement module-based configurations, the modules in every column or row are changed to other columns or rows in the entire 6×6 size array depending on the type of puzzle used. As shown in Figure 9, the rearrangement of modules is based on the puzzle number patterns, including Sudoku, Arrow Sudoku, Ken-

Ken type, skyscrapers type, Non-symmetric, CBM, Odd-Even, Futoshiki, Latin Square, Magic Square, Im based (current based arrangement) and Vm based (voltage based arrangement) method [15-16]. For the Im based method, let's consider a 6×6 TCT array with 36 modules which are rearranged by Im values of SPV module as shown in Figure 9. In the proposed rearrangement method, only modules are rearranged in different rows or columns without altering the electrical connections of SPV array configurations. So, the shade will be dispersed to a new row or column in the array. It improves the performance of photovoltaic array configurations, compared to other conventional configurations. In this rearrangement-based configuration, the performance will be improved but it requires more wires for repositioning of modules to a new row or column in an array. It leads to wiring losses and increases the installation cost of the solar plant. The rearrangement of modules based on Sudoku puzzle for TCT configuration is shown in Figure 8. In a similar way, remaining SPV TCT array configurations are rearranged based on puzzle patterns shown in Figure 9.

In the Series-Parallel configuration, series connection of modules (strings) are connected in parallel shown in Figure 4(c). The TCT array topology is formed from interconnecting the rows of the junction of SP scheme through ties. In the optimal TCT configuration type, ties are connected between modules, depending on the number of shaded modules and their locations in an array configuration. In Sudoku, Arrow Sudoku, Ken-Ken, Non-symmetric and Latin square type, modules in 1$^{st}$ column are unchanged, while the positions of 2$^{nd}$, 3$^{rd}$, 4$^{th}$, 5$^{th}$ and 6$^{th}$ column modules are changed and based on the puzzle pattern. In skyscraper, CBM, Odd-Even and Futoshiki type of TCT array configurations, all modules in each row and column are changed to the new optimal location in an array according to puzzle arrangement shown in Figure 9.

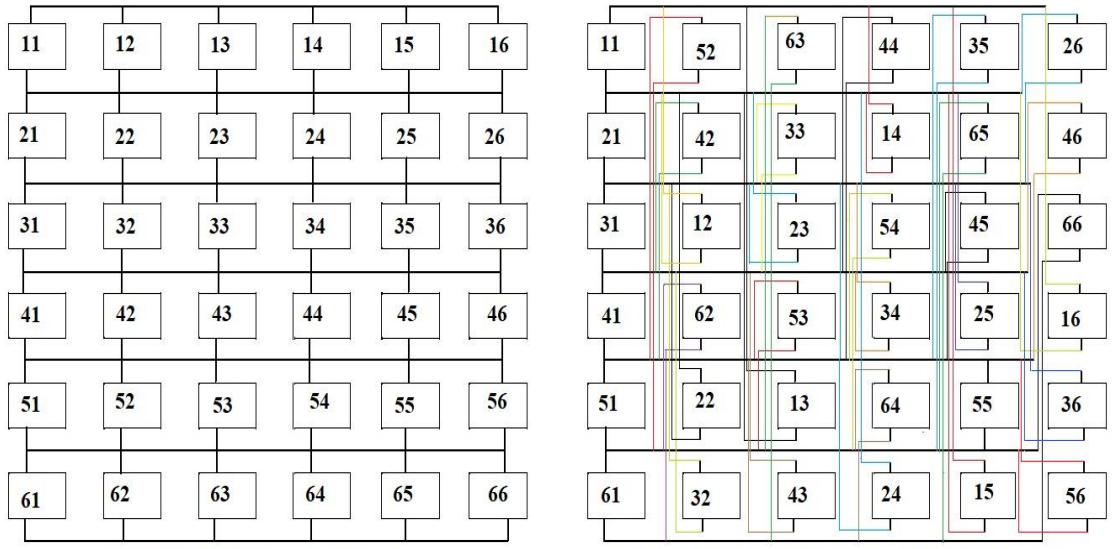


**Figure 8.** Proposed Su-Do-Ku puzzle based re-arranged TCT SPV array configuration

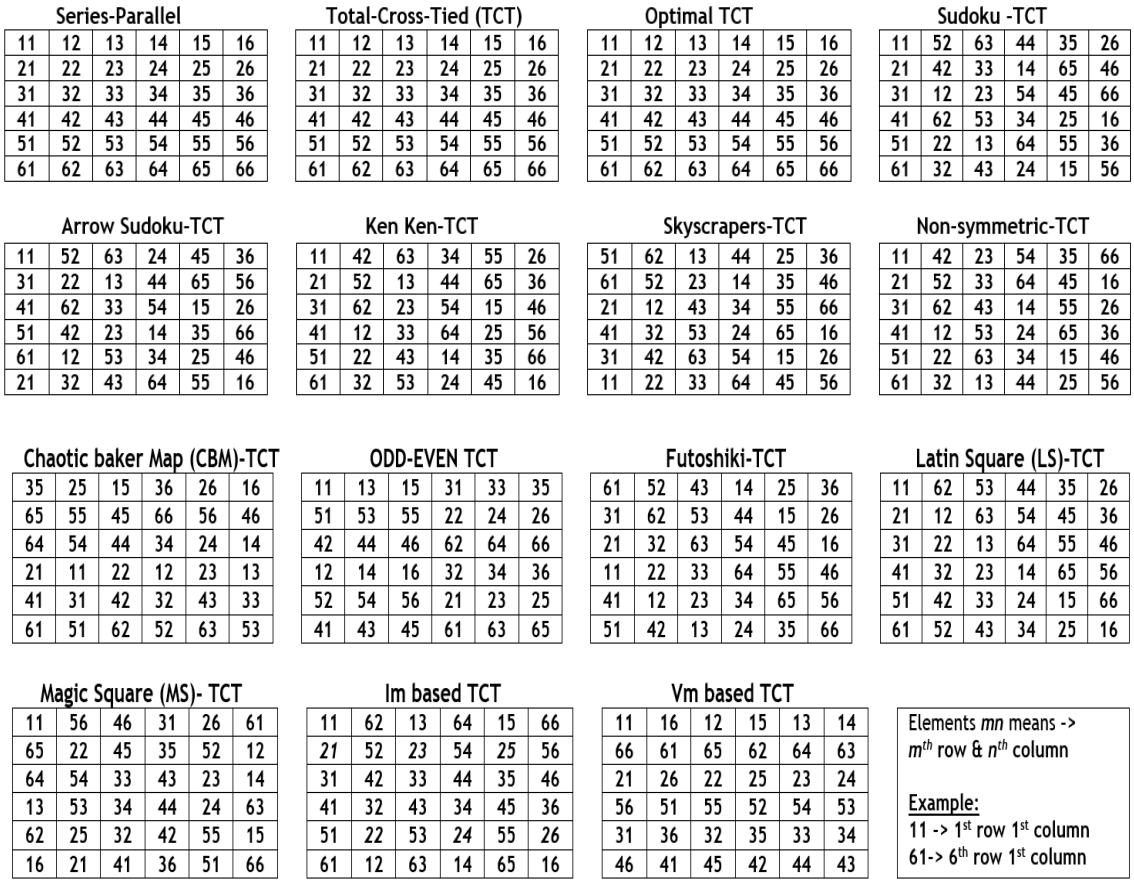


**Figure 9.** Rearrangement of modules in TCT SPV array Configurations based on puzzle patterns

## 4.2 Shade Dispersion Analysis of Su-Do-Ku Puzzle Based TCT SPV Array Configuration

Figure 10 shows the shade dispersion analysis for the Sudoku puzzle based TCT configuration. As shown in Figure 10(a), a 6×6 size TCT PV array consists of 6 rows and 6 columns of modules. In this method, the PV modules are repositioned in each row and column based on puzzle patterns without altering electrical connections. These electrical interconnections are the same as that of the TCT array topology. The module arrangement in Sudoku pattern is shown in Figure 10(b). The modules in the 1$^{st}$ column remain unchanged and modules in remaining five columns are changed their positions as shown in Figure 10(c). For the 5$^{th}$ row of the TCT array configuration that is completely shaded, the modules are repositioned to new optimal location in a same column by rearrangement of modules based on Sudoku puzzle. In the Sudoku arrangement, the modules are re-arranged to a new position, compare to previous positions as shown in Figure 10(a). In this arrangement, the position of the shaded modules is changed, and the shade will be dispersed to a new position, as shown in Figure 10(d) of shade dispersion with Sudoku-TCT configuration. By this shade dispersion technique, the shading on the TCT array configuration is dispersed without altering the electrical connections by simply repositioning of existing modules in an array, and it improves the output power of array as compared to the conventional TCT configuration.

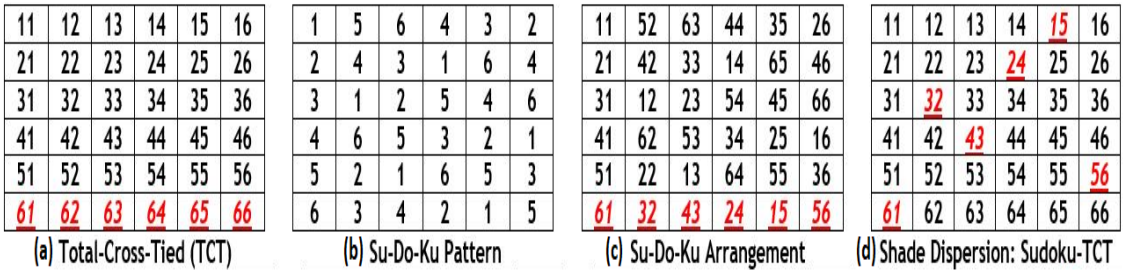


**Figure 10.** Su-Do-Ku based TCT configuration with shade dispersion technique

## 4.3. Performance of Rearrangement Modules Based TCT SPV Array Configuration

This section describes the comprehensive study on SP, TCT, optimal TCT and puzzle-based rearrangement of TCT array configurations [8-10] under one uniform case-U and 14 number of shading scenarios (Cases 1-14). The proposed optimal interconnection technique is applicable for PV systems of any size, improves the array power, and requires a minimum number of ties and low shading losses, compared to SP and TCT configurations. This optimal method doesn't require any switches or sensors, so it is simple to implement [9-13].

The interconnections or ties among modules are a, b, c, d, e, f, g, h, i, j, k, l, m, n, o, p, q, r, s, t, u, v, w, x and y, as shown in Figure 6. For SP configurations, no tie connections are required, and in puzzle based rearranged TCT configurations, a total 25 ties are required among modules. In the case of the proposed optimal configuration, only a smaller number of ties is required, which depends on the shading pattern. In this proposed optimal method, the mismatch losses given in Equation 8 are reduced compared to the series-parallel configuration, and the number of interconnections or ties are minimized compared to the TCT array configuration. It also reduces the installation time, cost, cable losses, and wiring required for installation of PV system.

$$\text{Mismatch power loss } \boldsymbol{P_{mmloss}}\,(\boldsymbol{W}) = \boldsymbol{P_{mu}} - \boldsymbol{P_{mpsc}} \quad \ldots\ldots\ldots\ldots (\mathbf{8})$$

$$\%\ \text{Power loss} = \frac{\boldsymbol{P_{mu}} - \boldsymbol{P_{mpsc}}}{\boldsymbol{P_{mu}}} \text{x}\ \mathbf{100} \quad \ldots\ldots\ldots\ldots (\mathbf{9})$$

$$\text{Fill-Factor (FF)} = \frac{\boldsymbol{V_{mpp}} * \boldsymbol{I_{mpp}}}{\boldsymbol{V_{oc}} * \boldsymbol{I_{sc}}} \quad \ldots\ldots\ldots\ldots (\mathbf{10})$$

$$\text{Efficiency, } \eta = \frac{\boldsymbol{V_{mp}} * \boldsymbol{I_{mp}}}{\boldsymbol{P_{in}}} \text{x}\mathbf{100} \quad \ldots\ldots\ldots\ldots (\mathbf{11})$$

Where $P_{in}$ = Number of SPV modules × Area of Module, and Area of module= 1952×982 mm (given in Table 1: specifications of solar ELDORA 270W PV module). $\boldsymbol{P_{mu}}$ is the global maximum power (GMPP) of the SPV array at uniform irradiation of 1000 W/m$^2$ and $\boldsymbol{P_{mpsc}}$ is the array power at different shading cases. $\boldsymbol{V_{mp}}$ is the maximum voltage and $\boldsymbol{I_{mp}}$ is the current at maximum power point. $\boldsymbol{V_{oc}}$ and $\boldsymbol{I_{sc}}$ are open circuit voltage and short circuit currents of the SPV module, respectively [11-15].

*Wiring Losses for Solar PV Array Configurations*

The repositioning of modules to the optimal location within an array increases the distance of wiring requirement for electrical connections of modules in each column in an array configuration. So, the wire resistance is increased, which causes a wiring loss and

increases the voltage drop. The additional length of wires required for each module depends on the physical location of the previous and next modules in the same column. Compared to the optimal interconnections of the TCT configuration under different partial shading conditions, it increases the wiring losses in a rearrangement based TCT array configuration. If the connections or ties among modules in an array are less, the wiring requirement for the PV system installation can be reduced. But in the TCT array configuration, the number of ties or interconnections among modules are more, so the wiring requirement is more. In the TCT type of configuration system, the cost of the installation increases and wiring losses are more due to the additional length of wires used for interconnection among modules in array configuration.

## 5. Results and Discussion

The output PV (Power-Voltage) characteristics of SP, proposed rearranged based TCT and proposed optimal topology under 14 different shading and one un-shaded are shown in Figures 11 to 25. The global maximum powers of the array of SP, rearranged based TCT and proposed optimal interconnection topology are shown in Figure 26. In the uniform irradiance case-U, the global maximum peak power of SP, rearranged TCT and proposed optimal configurations or topology are the same *i.e.*, 9620 W and the maximum power will be changed in different shading scenarios. The array global maximum power and mismatch or shading losses, fill-factor, efficiency of TCT array configurations under 14 different partial shading cases (Cases 1 to 14) are tabulated in Table 5.

**Table 5.** Array power, fill-Factor and efficiency of different configurations

| Configurations | Parameters | Cases | | | | | | | | | | | | | |
|---|---|---|---|---|---|---|---|---|---|---|---|---|---|---|---|
| | | 1 | 2 | 3 | 4 | 5 | 6 | 7 | 8 | 9 | 10 | 11 | 12 | 13 | 14 |
| Uniform | $P_{Gmpp}$ (W) | 9620 | 9620 | 9620 | 9620 | 9620 | 9620 | 9620 | 9620 | 9620 | 9620 | 9620 | 9620 | 9620 | 9620 |
| | $P_{mmloss}$ (W) | 0 | 0 | 0 | 0 | 0 | 0 | 0 | 0 | 0 | 0 | 0 | 0 | 0 | 0 |
| | %Power Loss | **0** | **0** | **0** | **0** | **0** | **0** | **0** | **0** | **0** | **0** | **0** | **0** | **0** | **0** |
| | Fill Factor | 0.743 | 0.743 | 0.743 | 0.743 | 0.743 | 0.743 | 0.743 | 0.743 | 0.743 | 0.743 | 0.743 | 0.743 | 0.743 | 0.743 |
| | η | 14.0 | 14.0 | 14.0 | 14.0 | 14.0 | 14.0 | 14.0 | 14.0 | 14.0 | 14.0 | 14.0 | 14.0 | 14.0 | 14.0 |
| 1. SP | $P_{Gmpp}$ (W) | 7974 | 8834 | 5550 | 7974 | 8123 | 7339 | 5441 | 5154 | 6617 | 5346 | 4113 | 6328 | 8869 | 5190 |
| | $P_{mmloss}$ (W) | 1646 | 786 | 4070 | 1646 | 1497 | 2281 | 4179 | 4466 | 3003 | 4274 | 5507 | 3292 | 751 | 4430 |
| | %Power Loss | ***17.11*** | ***8.17*** | ***42.3*** | ***17.11*** | ***15.56*** | ***23.71*** | ***43.44*** | ***46.42*** | ***31.21*** | ***44.42*** | ***57.24*** | ***34.22*** | ***7.80*** | ***46.05*** |
| | Fill Factor | 0.619 | 0.744 | 0.431 | 0.619 | 0.627 | 0.567 | 0.424 | 0.485 | 0.511 | 0.50 | 0.341 | 0.493 | 0.685 | 0.439 |
| | η | 12.57 | 13.94 | 10.14 | 12.57 | 12.61 | 12.7 | 9.76 | 11.17 | 12.29 | 10.69 | 9.77 | 10.97 | 13.0 | 10.59 |
| 2. TCT | $P_{Gmpp}$ (W) | 7974 | 8834 | 7082 | 8834 | 8558 | 7687 | 5725 | 5285 | 6778 | 5433 | 5704 | 8049 | 9352 | 5510 |
| | $P_{mmloss}$ (W) | 1646 | 786 | 2538 | 786 | 1062 | 1933 | 3895 | 4335 | 2842 | 4187 | 3916 | 1571 | 268 | 4110 |
| | %Power Loss | ***17.11*** | ***8.17*** | ***26.38*** | ***8.17*** | ***11.03*** | ***20.10*** | ***40.48*** | ***45.06*** | ***29.54*** | ***43.52*** | ***40.70*** | ***16.33*** | ***2.78*** | ***42.72*** |
| | Fill Factor | 0.619 | 0.747 | 0.602 | 0747 | 0.663 | 0.598 | 0.447 | 0.498 | 0.53 | 0.511 | 0.675 | 0.752 | 0.722 | 0.472 |
| | η | 12.58 | 13.94 | 12.94 | 13.94 | 13.30 | 13.34 | 10.28 | 11.47 | 12.60 | 10.88 | 13.56 | 13.97 | 13.72 | 11.25 |
| 3. Optimal-TCT | $P_{Gmpp}$ (W) | 7974 | 8834 | 7042 | 8834 | 8257 | 7493 | 5441 | 5213 | 6752 | 5410 | 4196 | 8049 | 8990 | 5294 |
| | $P_{mmloss}$ (W) | 1646 | 786 | 2578 | 786 | 1363 | 2127 | 4179 | 4407 | 2868 | 4210 | 5424 | 1571 | 630 | 4326 |
| | %Power Loss | ***17.11*** | ***8.17*** | ***26.79*** | ***8.17*** | ***14.16*** | ***22.11*** | ***43.44*** | ***45.81*** | ***29.81*** | ***43.76*** | ***56.38*** | ***16.33*** | ***6.54*** | ***44.96*** |
| | Fill Factor | 0.619 | 0.744 | 0.598 | 0.746 | 0.638 | 0.579 | 0.424 | 0.49 | 0.526 | 0.506 | 0.355 | 0.752 | 0.694 | 0.45 |
| | η | 12.58 | 13.94 | 12.87 | 13.94 | 12.83 | 13.0 | 9.77 | 11.31 | 12.56 | 10.83 | 9.98 | 13.97 | 13.19 | 10.81 |
| 4. Su Do Ku-TCT | $P_{Gmpp}$ (W) | 8834 | 8834 | 7082 | 8599 | 8881 | 8049 | 7618 | 6075 | 7422 | 6815 | 5704 | 7173 | 9352 | 6716 |
| | $P_{mmloss}$ (W) | 786 | 786 | 2538 | 1021 | 740 | 1571 | 2002 | 3545 | 2198 | 2805 | 3916 | 2447 | 268 | 2904 |
| | %Power Loss | **8.17** | **8.17** | **26.38** | **10.61** | **7.69** | **16.33** | **20.81** | **36.85** | **22.84** | **29.15** | **40.70** | **25.43** | **2.78** | **30.18** |
| | Fill Factor | 0.747 | 0.747 | 0.603 | 0.667 | 0.689 | 0.752 | 0.712 | 0.635 | 0.695 | 0.711 | 0.675 | 0.61 | 0.722 | 0.701 |
| | η | 13.94 | 13.94 | 12.94 | 13.57 | 13.80 | 13.97 | 13.68 | 14.06 | 13.80 | 13.65 | 13.56 | 13.52 | 13.72 | 13.71 |

| | | | | | | | | | | | | | | | | |
|---|---|---|---|---|---|---|---|---|---|---|---|---|---|---|---|---|
| **5. Arrow Su Do Ku-TCT** | $P_{Gmpp}$ (W) | 8834 | 8834 | 6394 | 8013 | 8916 | 7702 | 7618 | 6480 | 7057 | 6752 | 5704 | 7058 | 9352 | 6716 |
| | $P_{mmloss}$ (W) | 786 | 786 | 3226 | 1607 | 704 | 1918 | 2002 | 3140 | 2563 | 2868 | 3916 | 2562 | 268 | 2904 |
| | **%Power Loss** | **8.17** | **8.17** | **33.53** | **16.70** | **7.31** | **19.93** | **20.81** | **32.64** | **26.64** | **29.81** | **40.70** | **26.63** | **2.78** | **30.18** |
| | **Fill Factor** | 0.745 | 0.745 | 0.544 | 0.521 | 0.691 | 0.654 | 0.712 | 0.762 | 0.66 | 0.635 | 0.675 | 0.549 | 0.722 | 0.70 |
| | η | 13.94 | 13.94 | 11.68 | 12.64 | 13.86 | 13.37 | 13.68 | 14.06 | 13.12 | 13.52 | 13.56 | 12.25 | 13.72 | 13.71 |
| **6. Ken Ken-TCT** | $P_{Gmpp}$ (W) | 8704 | 8834 | 7082 | 8599 | 8916 | 7790 | 7617 | 6480 | 7057 | 6692 | 5704 | 7687 | 9352 | 6716 |
| | $P_{mmloss}$ (W) | 916 | 786 | 2538 | 1021 | 704 | 1830 | 2003 | 3140 | 2563 | 2928 | 3916 | 1933 | 268 | 2904 |
| | **%Power Loss** | **9.52** | **8.17** | **26.38** | **10.61** | **7.31** | **19.02** | **20.82** | **32.64** | **26.64** | **30.43** | **40.70** | **20.1** | **2.78** | **30.18** |
| | **Fill Factor** | 0.736 | 0.747 | 0.60 | 0.667 | 0.691 | 0.661 | 0.711 | 0.762 | 0.66 | 0.629 | 0.675 | 0.599 | 0.722 | 0.701 |
| | η | 13.73 | 13.94 | 12.94 | 13.57 | 13.86 | 13.52 | 13.68 | 14.06 | 13.12 | 13.40 | 13.56 | 13.34 | 13.72 | 13.71 |
| **7. Skyscrapers- TCT** | $P_{Gmpp}$ (W) | 8834 | 8834 | 7082 | 8030 | 8558 | 8049 | 7618 | 6075 | 7057 | 6752 | 5704 | 7167 | 9352 | 6262 |
| | $P_{mmloss}$ (W) | 786 | 786 | 2538 | 1590 | 1062 | 1571 | 2002 | 3545 | 2563 | 2868 | 3916 | 2453 | 268 | 3358 |
| | **%Power Loss** | **8.17** | **8.17** | **26.38** | **16.52** | **11.03** | **16.33** | **20.81** | **36.85** | **26.64** | **29.81** | **40.70** | **25.49** | **2.78** | **34.90** |
| | **Fill Factor** | 0.747 | 0.747 | 0.602 | 0.623 | 0.663 | 0.752 | 0.712 | 0.635 | 0.66 | 0.634 | 0.675 | 0.558 | 0.723 | 0.653 |
| | η | 13.94 | 13.94 | 12.94 | 12.67 | 13.30 | 13.97 | 13.68 | 13.18 | 13.12 | 13.52 | 13.56 | 12.44 | 13.72 | 12.79 |
| **8. Non Symmetric-TCT** | $P_{Gmpp}$ (W) | 8834 | 8834 | 7097 | 8511 | 8916 | 7790 | 7618 | 6480 | 7057 | 6752 | 5704 | 7687 | 9352 | 6716 |
| | $P_{mmloss}$ (W) | 786 | 786 | 2523 | 1109 | 704 | 1830 | 2002 | 3140 | 2563 | 2868 | 3916 | 1933 | 268 | 2904 |
| | **%Power Loss** | **8.17** | **8.17** | **26.22** | **11.52** | **7.3** | **19.02** | **20.81** | **32.64** | **26.64** | **29.81** | **40.70** | **20.1** | **2.78** | **30.18** |
| | **Fill Factor** | 0.747 | 0.747 | 0.664 | 0.659 | 0.691 | 0.662 | 0.711 | 0.762 | 0.66 | 0.634 | 0.675 | 0.598 | 0.723 | 0.70 |
| | η | 13.94 | 13.94 | 12.97 | 13.43 | 13.86 | 13.52 | 13.68 | 14.06 | 13.12 | 13.52 | 13.56 | 13.34 | 13.72 | 13.71 |
| **9. Chaotic baker map (CBM) - TCT** | $P_{Gmpp}$ (W) | 7899 | 8030 | 6442 | 8511 | 8650 | 8049 | 7499 | 6075 | 7041 | 6284 | 5704 | 7701 | 9352 | 6150 |
| | $P_{mmloss}$ (W) | 1721 | 1590 | 3178 | 1109 | 970 | 1571 | 2121 | 3545 | 2579 | 3336 | 3916 | 1919 | 268 | 3470 |
| | **%Power Loss** | **17.88** | **16.52** | **33.03** | **11.52** | **10.08** | **16.33** | **22.04** | **36.85** | **26.80** | **34.67** | **40.70** | **19.94** | **2.78** | **36.07** |
| | **Fill Factor** | 0.613 | 0.623 | 0.549 | 0.66 | 0.67 | 0.752 | 0.638 | 0.636 | 0.60 | 0.59 | 0.675 | 0.654 | 0.723 | 0.578 |
| | η | 12.46 | 12.67 | 11.77 | 13.43 | 13.44 | 13.97 | 13.46 | 13.18 | 13.09 | 12.58 | 13.56 | 13.37 | 13.72 | 12.56 |
| **10. ODD EVEN-TCT** | $P_{Gmpp}$ (W) | 7899 | 8442 | 7082 | 8834 | 8558 | 6310 | 7486 | 6011 | 6967 | 6698 | 5704 | 8049 | 9352 | 5510 |
| | $P_{mmloss}$ (W) | 1721 | 1178 | 2538 | 786 | 1062 | 3310 | 2134 | 3609 | 2653 | 2922 | 3916 | 1571 | 268 | 4110 |
| | **%Power Loss** | **17.88** | **12.24** | **26.38** | **8.17** | **11.03** | **34.40** | **22.18** | **37.51** | **27.57** | **30.37** | **40.70** | **16.33** | **2.78** | **42.27** |
| | **Fill Factor** | 0.613 | 0.654 | 0.60 | 0.747 | 0.663 | 0.49 | 0.584 | 0.628 | 0.653 | 0.629 | 0.675 | 0.752 | 0.722 | 0.471 |
| | η | 12.46 | 13.32 | 12.94 | 13.94 | 13.30 | 10.95 | 13.44 | 13.04 | 12.96 | 13.41 | 13.56 | 13.97 | 13.72 | 11.25 |
| **11. Futoshiki-TCT** | $P_{Gmpp}$ (W) | 8834 | 8834 | 6381 | 7974 | 8650 | 8049 | 7618 | 6075 | 7057 | 6752 | 5704 | 6925 | 9352 | 5510 |
| | $P_{mmloss}$ (W) | 786 | 786 | 3239 | 1646 | 970 | 1571 | 2002 | 3545 | 2563 | 2868 | 3916 | 2695 | 268 | 4110 |
| | **%Power Loss** | **8.17** | **8.17** | **33.66** | **17.11** | **10.08** | **16.33** | **20.81** | **36.85** | **26.64** | **19.81** | **40.70** | **28.01** | **2.78** | **42.27** |
| | **Fill Factor** | 0747 | 0.747 | 0.543 | 0.619 | 0.671 | 0.752 | 0.711 | 0.636 | 0.66 | 0.634 | 0.675 | 0.539 | 0723 | 0.471 |
| | η | 13.94 | 13.94 | 11.66 | 12.58 | 13.44 | 13.97 | 13.68 | 13.18 | 13.12 | 13.52 | 13.56 | 12.02 | 13.72 | 11.25 |
| **12. Latin Square-TCT** | $P_{Gmpp}$ (W) | 8834 | 8834 | 6381 | 7974 | 8649 | 8049 | 7618 | 6075 | 7057 | 6752 | 5704 | 6925 | 9352 | 5510 |
| | $P_{mmloss}$ (W) | 786 | 786 | 3239 | 1646 | 971 | 1571 | 2002 | 3545 | 2563 | 2868 | 3916 | 2695 | 268 | 4110 |
| | **%Power Loss** | **8.17** | **8.17** | **33.66** | **17.11** | **10.09** | **16.33** | **20.81** | **36.85** | **26.64** | **29.81** | **40.70** | **28.01** | **27.85** | **42.72** |
| | **Fill Factor** | 0.747 | 0.747 | 0.543 | 0.619 | 0.669 | 0.752 | 0.712 | 0.635 | 0.66 | 0.635 | 0.675 | 0.541 | 0.722 | 0.472 |
| | η | 13.94 | 13.94 | 11.66 | 12.58 | 13.44 | 13.97 | 13.68 | 13.18 | 13.12 | 13.52 | 13.56 | 12.02 | 13.72 | 11.25 |
| **13. Magic Square-TCT** | $P_{Gmpp}$ (W) | 8834 | 7899 | 7460 | 8834 | 8650 | 7687 | 7618 | 6075 | 6778 | 5433 | 5704 | 8049 | 9352 | 6716 |
| | $P_{mmloss}$ (W) | 786 | 1721 | 2160 | 786 | 970 | 1933 | 2002 | 3545 | 2842 | 3887 | 3916 | 1571 | 268 | 2904 |
| | **%Power Loss** | **8.17** | **17.88** | **22.45** | **8.17** | **10.08** | **20.09** | **20.81** | **36.85** | **29.54** | **40.40** | **40.70** | **16.33** | **2.78** | **30.18** |
| | **Fill Factor** | 0.747 | 0.612 | 0.635 | 0747 | 0.67 | 0.599 | 0.711 | 0.635 | 0.53 | 0.511 | 0.674 | 0.752 | 0.722 | 0.70 |
| | η | 13.94 | 12.46 | 13.63 | 13.94 | 13.44 | 13.34 | 13.68 | 13.18 | 12.60 | 10.88 | 13.56 | 13.97 | 13.72 | 13.71 |
| **14. Im based TCT** | $P_{Gmpp}$ (W) | 7899 | 8834 | 7097 | 8442 | 8916 | 7790 | 7499 | 6480 | 6778 | 5433 | 5704 | 8049 | 9352 | 6716 |
| | $P_{mmloss}$ (W) | 1721 | 786 | 2523 | 1178 | 704 | 1830 | 2121 | 3140 | 2842 | 4187 | 3916 | 1571 | 268 | 2904 |
| | **%Power Loss** | **17.88** | **8.17** | **26.22** | **12.24** | **7.31** | **19.02** | **22.04** | **32.64** | **29.54** | **43.52** | **40.70** | **16.33** | **2.78** | **30.18** |
| | **Fill Factor** | 0.612 | 0.747 | 0.55 | 0.654 | 0.691 | 0.662 | 0.638 | 0.762 | 0.53 | 0.511 | 0.675 | 0.752 | 0.722 | 0.70 |
| | η | 12.46 | 13.94 | 12.97 | 13.32 | 13.86 | 13.52 | 13.46 | 14.06 | 12.60 | 10.88 | 13.56 | 13.97 | 13.72 | 13.71 |
| **15. Vm based TCT** | $P_{Gmpp}$ (W) | 7974 | 8834 | 7082 | 8834 | 8558 | 7687 | 5725 | 5285 | 6778 | 5433 | 5704 | 8049 | 9352 | 5510 |
| | $P_{mmloss}$ (W) | 1646 | 786 | 2538 | 786 | 1062 | 1933 | 3895 | 4335 | 2842 | 4187 | 3916 | 1571 | 268 | 4110 |
| | **%Power Loss** | **17.11** | **8.17** | **26.38** | **8.17** | **11.03** | **20.1** | **40.48** | **45.06** | **29.54** | **43.52** | **40.70** | **16.33** | **2.78** | **42.72** |
| | **Fill Factor** | 0.619 | 0.747 | 0.60 | 0.747 | 0.663 | 0.598 | 0.447 | 0.498 | 0.53 | 0.511 | 0.675 | 0.752 | 0.722 | 0.472 |
| | η | 12.58 | 13.94 | 12.94 | 13.94 | 13.30 | 13.34 | 10.28 | 11.47 | 12.60 | 10.88 | 13.56 | 13.97 | 13.72 | 11.25 |

From the simulation results, it can be concluded that,

- In partial shading case-1: Sudoku, Arrow Sudoku, skyscrapers, non-symmetrical, Futoshiki, LS and MS type of TCT array configurations have the maximum global peak power of 8834 W.
- In partial shading case-2: SP, TCT, proposed optimal TCT, Sudoku, Arrow Sudoku, Ken-Ken, skyscrapers, Non-symmetrical, futoshiki, LS, Im based and Vm based TCT configurations have the maximum power of 8834 W.

- In partial shading case-3: Magic Square (MS) TCT array configuration has the maximum power of 7460 W.
- In partial shading case-4: TCT, proposed optimal TCT, Odd-Even, MS, Vm based TCT configurations have the maximum power of 8834 W.
- In partial shading case-5: Arrow Sudoku, Ken-Ken, Non-symmetric, Im based TCT configurations have the maximum power of 8916 W.
- In partial shading case-6: Sudoku, skyscraper, CBM, Futoshiki, LS type configurations have the maximum power of 8049 W.
- In partial shading case-7: Sudoku, Arrow Sudoku, skyscraper, Non-symmetric, Futoshiki, LS and MS type of SPV array configurations have the maximum power of 7618 W.
- In shading case-8: Arrow Sudoku, Ken-Ken, Non-symmetric, Im based TCT configurations have the maximum power of 6480 W.
- In partial shading case-9: Sudoku type TCT SPV array configuration has the maximum power of 7422 W.
- In partial shading case-10: Sudoku type TCT has the maximum power of 6815 W.
- In partial shading case-11: all rearrangement-based puzzle TCT configurations have the maximum global power of 5704 W.
- In partial shading case-12: TCT, optimal TCT, Odd-Even, MS, Im based and Vm based TCT configurations have the maximum power of 8049 W.
- In partial shading case-13: all rearrangement-based puzzle TCT configurations have the maximum global power of 9352 W.
- In partial shading case-14: Sudoku, Arrow Sudoku, Ken-Ken, Non-symmetric, MS, Im based TCT configurations have the maximum global power of 6716 W.
- Under partial shading conditions, rearrangement-based Total- Cross-Tied (TCT) array configurations show improved results compared to the conventional array topologies.
- In the proposed method of optimal configuration, the requirement of ties or interconnections for electrical connections of modules in an array configuration are changed based on the shading pattern in the array.
- Considering wiring losses in TCT and rearranged based TCT array topologies, the proposed optimal TCT array configuration has the better results compared to other rearranged based TCT array topologies. From the simulation results tabulated in Table 5, it can be concluded that the proposed optimal TCT array configuration, Sudoku, Arrow Sudoku, MS type of puzzle based TCT configurations have the highest global maximum peak power.

## 5.1 Simulation Results:

*Power-Voltage Characteristics of SPV TCT Array Configurations*

The performance characteristics (Power-Voltage) for different 6x6 size TCT SPV array configurations or topologies are shown in Figures 11 to 25. The global maximum peak powers of PV configurations under various shading cases are represented in Figure 26. The global maximum peak powers (GMPP) of each topology are tabulated in Table 5.

a. Series(S)-Parallel (P) Configuration:

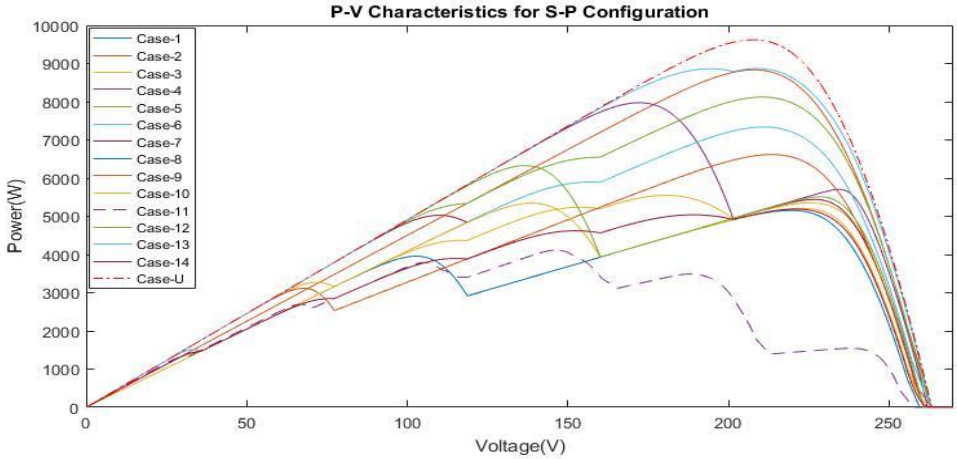


**Figure 11.** Output characteristics of 6 x 6 array S-P configuration

b. Total (T)-Cross(C)-Tied (T) configuration:

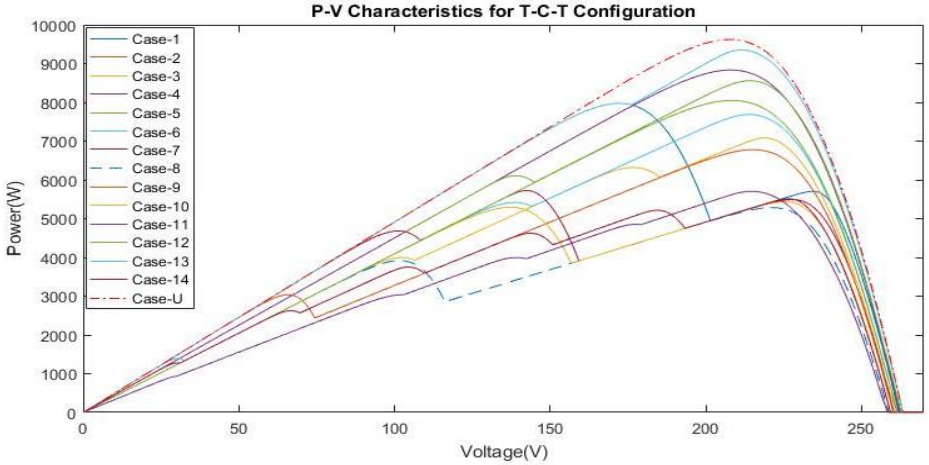


**Figure 12.** Output characteristics of 6 x 6 size TCT SPV array configuration

c. Proposed optimal array configuration:

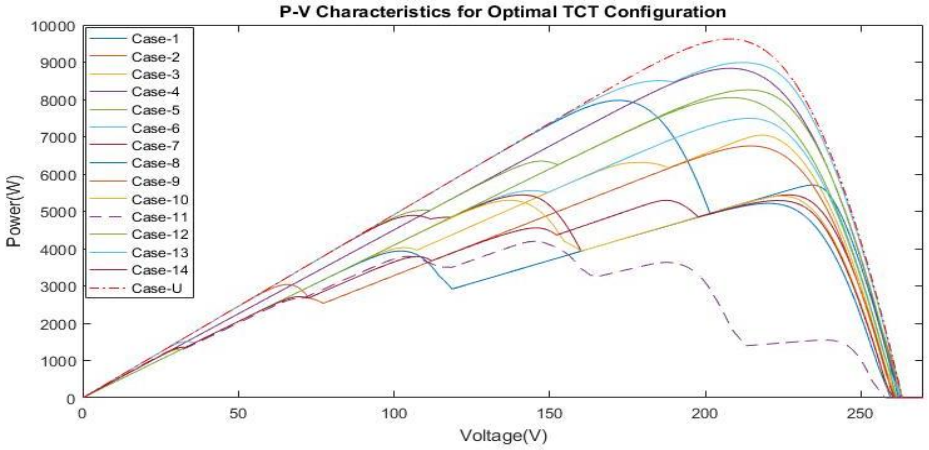


**Figure 13.** Output characteristics for proposed optimal configuration

d. Su-Do-Ku based T-C-T configuration:

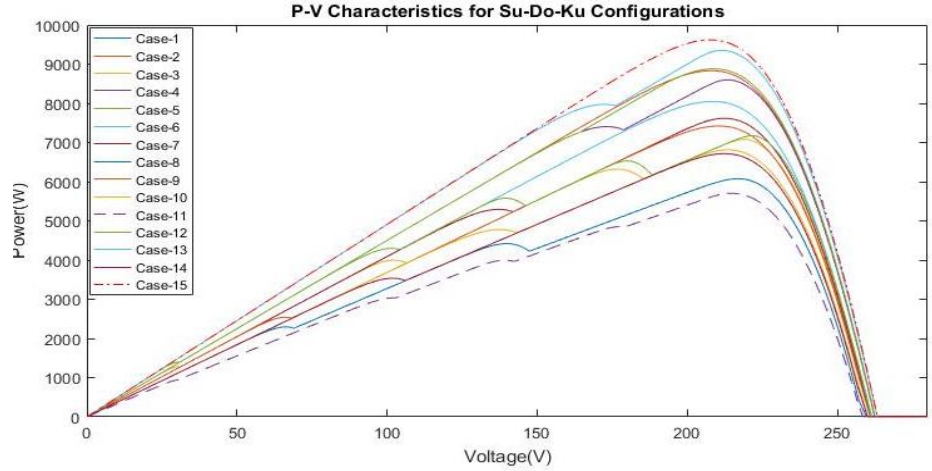


**Figure 14.** 6 x 6 array Sudoku-TCT configuration characteristics

e. Arrow Su-Do-Ku based TCT configuration:

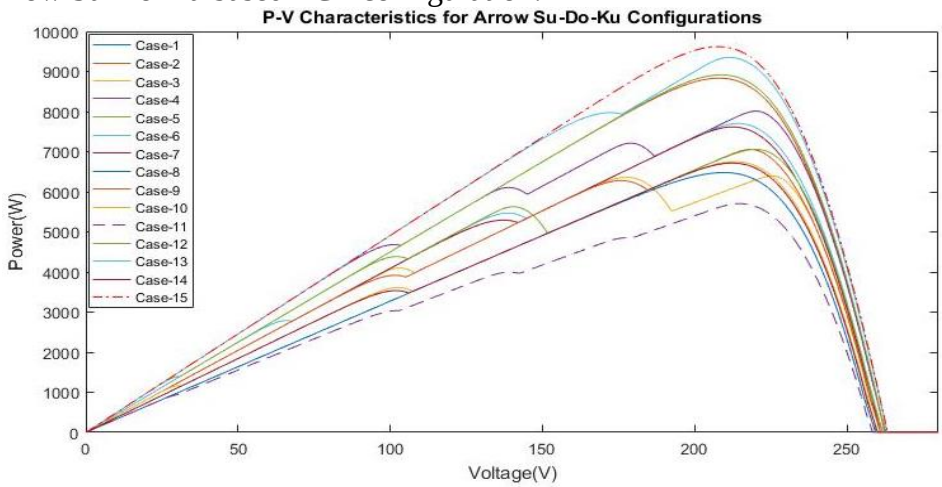


**Figure 15.** 6×6 array Arrow Sudoku TCT configuration characteristics

f. Ken-Ken based TCT configuration:

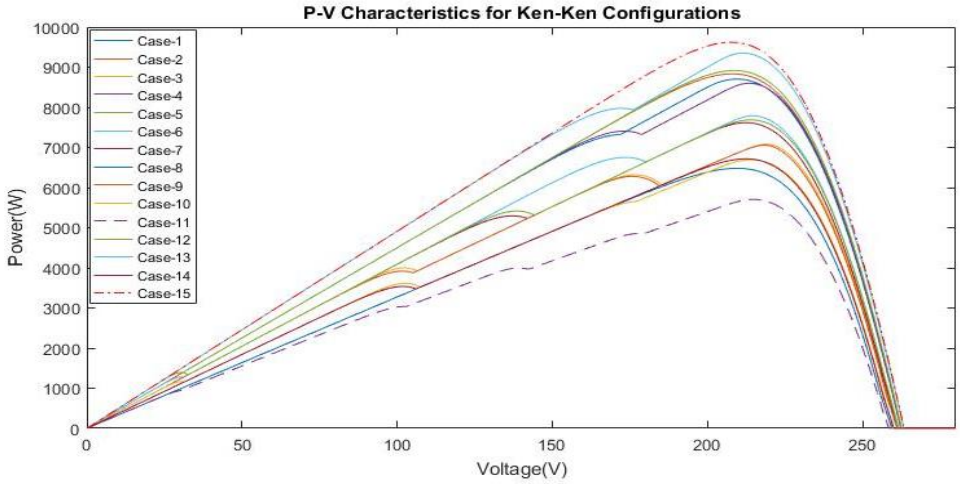


**Figure 16.** P-V characteristics for Modified Ken Ken-TCT configuration

g. Skyscrapers-TCT configuration:

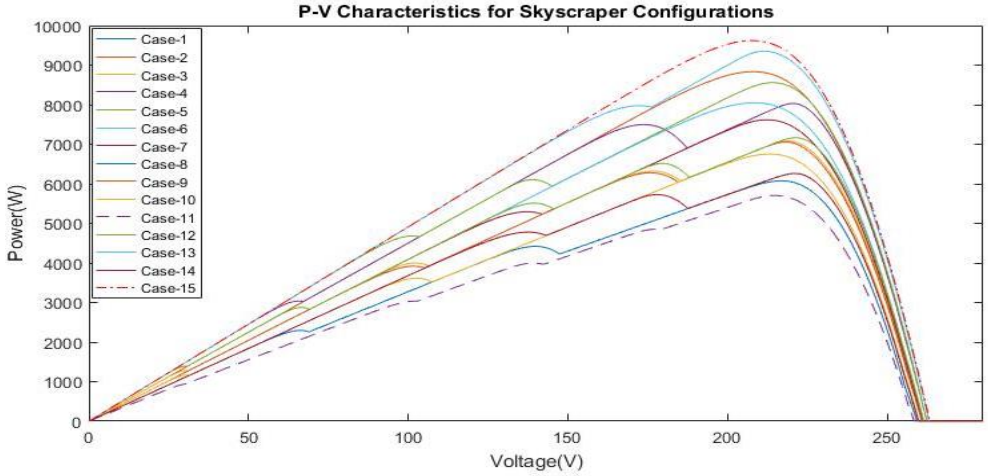


**Figure 17.** P-V characteristics for Skyscrapers TCT configuration

h. Non-Symmetric TCT configuration:

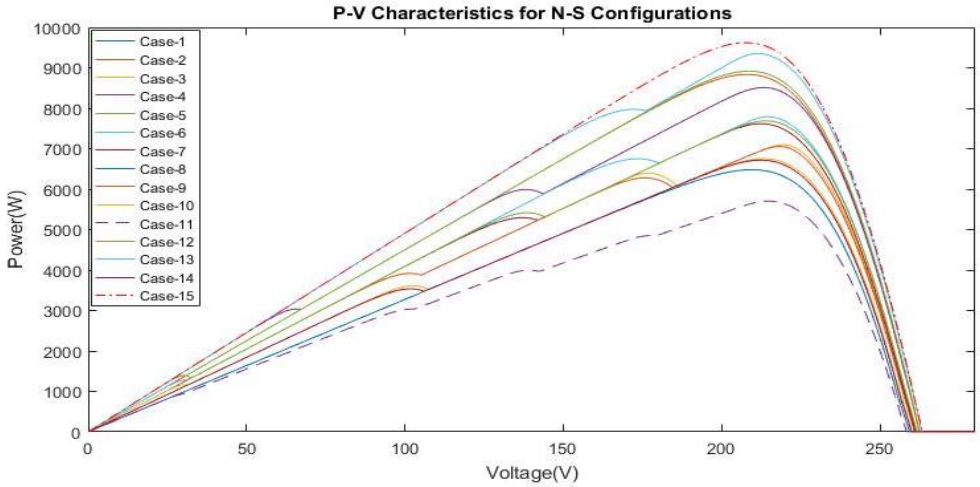


**Figure 18.** P-V characteristics for Non- Symmetric TCT Re-configuration

i. Chaotic Baker Map (CBM) TCT configuration:

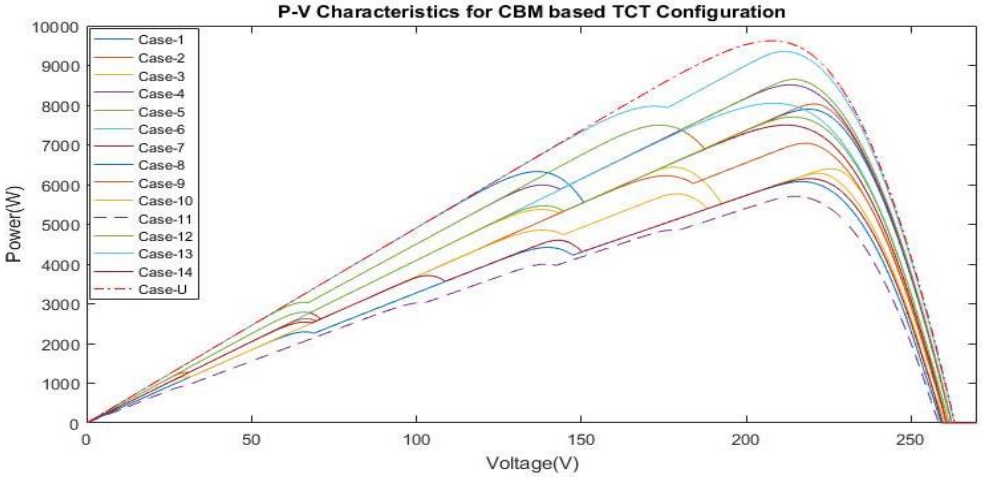


**Figure 19.** P-V characteristics for CBM TCT Re-configuration

j. ODD-EVEN based TCT configuration:

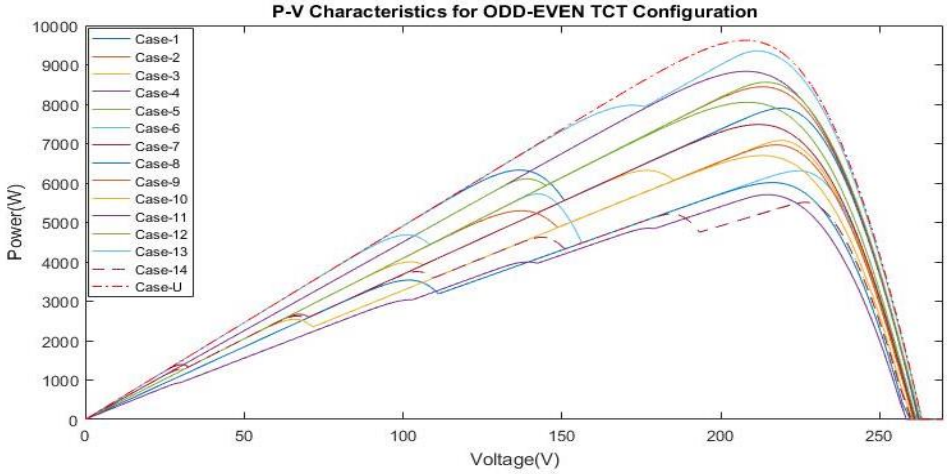


**Figure 20.** P-V characteristics for Odd Even TCT configuration

k. Futoshiki-TCT configuration:

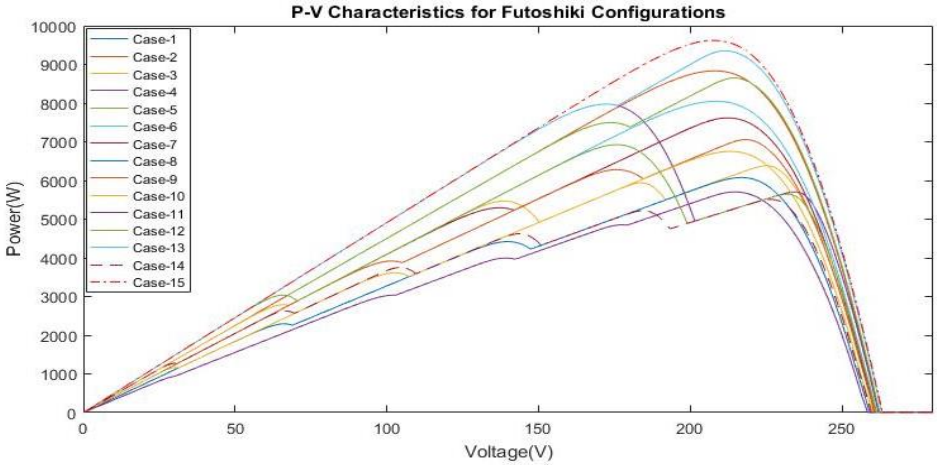


**Figure 21.** P-V characteristics for Futoshiki TCT configuration

l. Latin Square (LS) based TCT configuration:

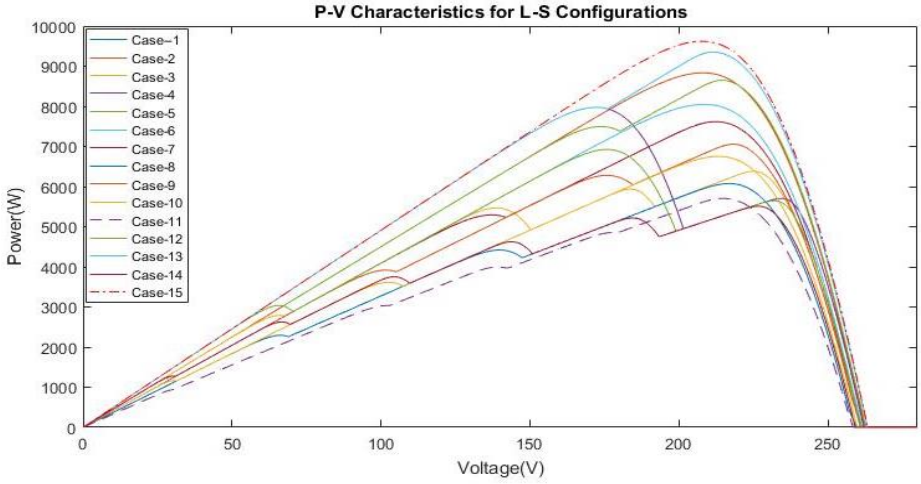


**Figure 22.** P-V characteristics for LS based TCT configuration

m. Magic Square (MS) TCT topology:

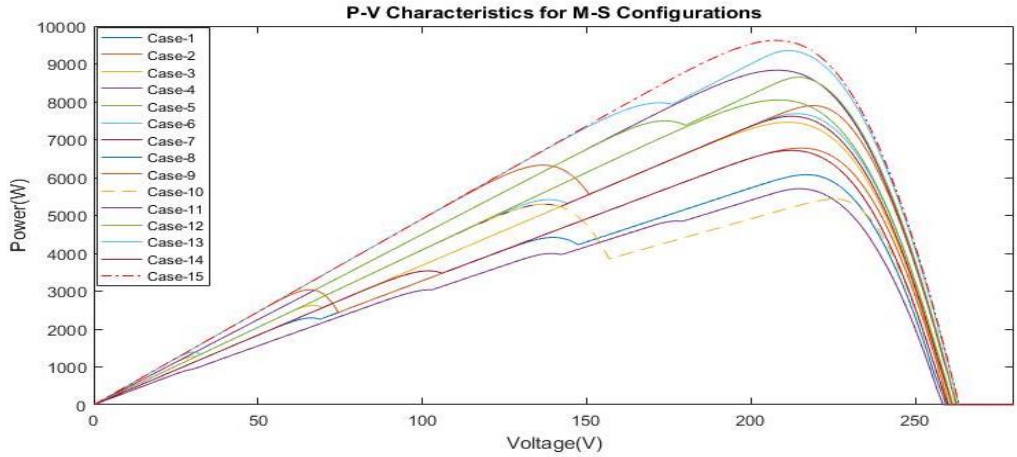


**Figure 23.** P-V characteristics for MS TCT configuration

n. Im based TCT configuration:

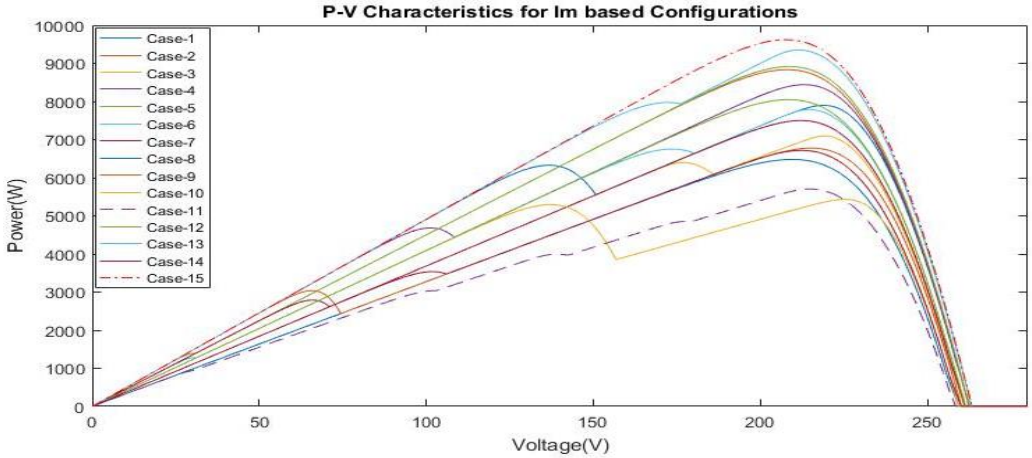


**Figure 24.** P-V characteristics for Im based TCT configuration

o. Vm based TCT configuration:

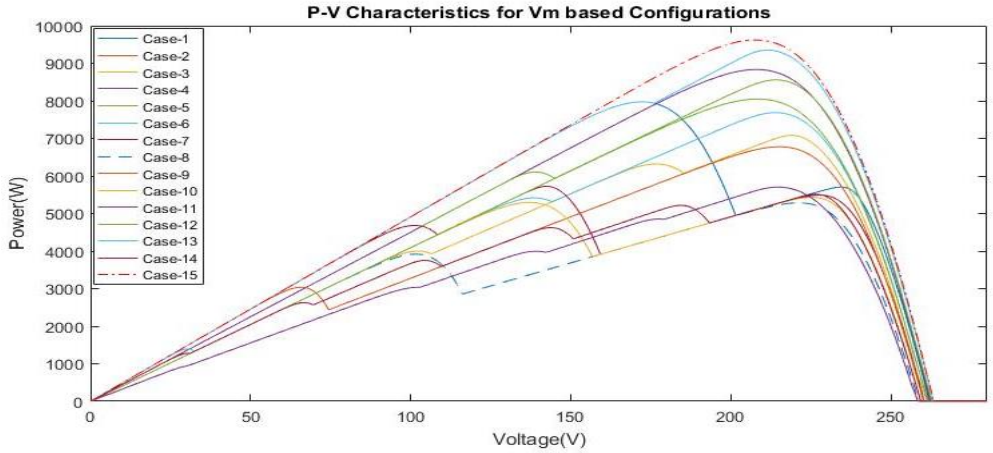


**Figure 25.** P-V characteristics for Vm based TCT configuration

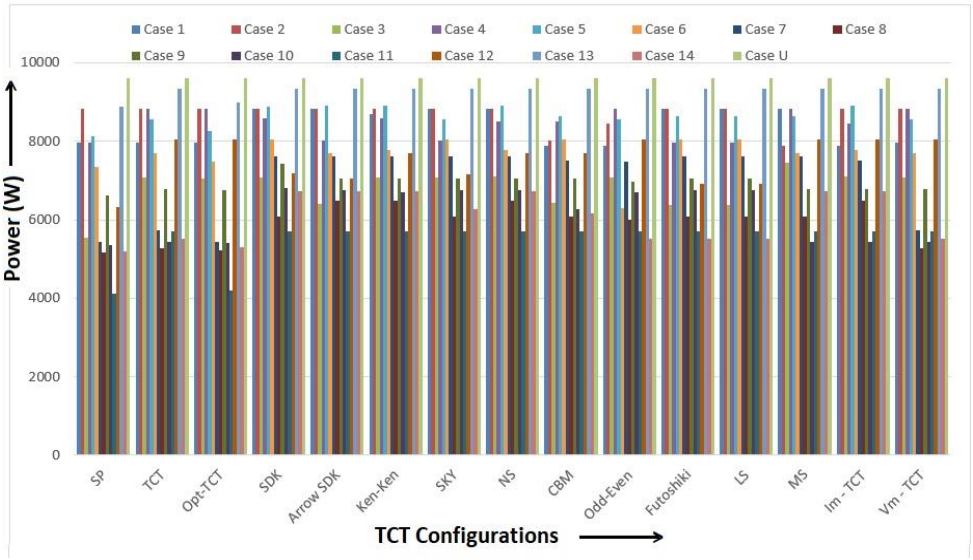


**Figure 26.** Global maximum powers of different TCT SPV array configurations

## CONCLUSIONS

The proposed optimal array configuration method can be applied to an array of any size by simply dividing the PV system into a number of 2×2 sub arrays. The performance of rearranged array TCT configurations based on puzzle patterns including Sudoku, Arrow Sudoku, Ken-Ken, CBM, Odd-Even, Futoshiki, LS, MS, Im based and Vm based array TCT configurations are compared with the proposed optimal TCT configuration under fourteen different partial shading cases and one uniform un-shaded case-U. In the rearrangement method, the positioning of modules is changed, but electrical connections are unchanged. The wiring losses and requirement of wires for the rearrangement of modules are more due to repositioning of photovoltaic modules without altering electrical connections. Compared to rearranged based TCT array configurations, the proposed optimal method slightly reduces the mismatch losses, improves the array global maximum power and the fill factor, and minimizes the number of interconnections among modules, time required for wiring at the time of installation of PV system, installation cost of photovoltaic system and complexity of modules interconnection in an array. The rearranged based configurations have greater array power in all proposed partial shading conditions, but due to the extra wire length required for module interconnections in the array configuration, there is more wiring loss.

## CONFLICTS OF INTEREST

The authors declare that there is no conflict of interests regarding the publication of this paper.

## REFERENCES

[1] J. Chattopadhyay, R. Singh, and O. Prakash, "Renewable Energy and its Innovative Technologies", *Proceedings of ICEMIT 2017*, Volume 1, Springer Singapore, 2019. DOI: 10.1007/978-981-13-2116-0
[2] M.I. Ahmad, M. Ismail, and S. Riffat, "Renewable Energy and Sustainable Technologies for Building and Environmental Applications: Options for a Greener Future", Springer International Publishing, 2016. DOI: 10.1007/978-3-319-31840-0
[3] J. Hossain and A. Mahmud, "Large Scale Renewable Power Generation: Advances in Technologies for Generation, Transmission and Storage", Springer Singapore, 2014. DOI: 10.1007/978-981-4585-30-9
[4] D. Nguyen and B. Lehman, "Modeling and Simulation of Solar PV Arrays under Changing Illumination Conditions", in 2006 IEEE Workshops on Computers in Power Electronics, 2006, pp. 295-299. DOI: 10.1109/COMPEL.2006.305629
[5] H. Braun, S.T. Buddha, V. Krishnan, A. M. Banavar, and D. Srinivasan, "Topology reconfiguration for optimization of photovoltaic array output", S*ustainable Energy, Grids and Networks*, vol. 6, pp. 58-69, 2016. DOI: 10.1016/j.segan.2016.01.003
[6] G. Sai Krishna and T. Moger, "Reconfiguration strategies for reducing partial shading effects in photovoltaic arrays: State of the art", *Solar Energy*, vol. 182, pp. 429-452, 2019. DOI: 10.1016/j.solener.2019.02.057
[7] D. Nguyen and B. Lehman, "A reconfigurable solar photovoltaic array under shadow conditions", in *2008 Twenty-Third Annual IEEE Applied Power Electronics Conference and Exposition*, 2008, pp. 980-986. DOI: 10.1109/APEC.2008.4522840
[8] G. S. Krishna and T. Moger, "Comparative Study on Solar Photovoltaic Array Configurations Under Irregular Irradiance Conditions", in *2018 8th IEEE India International Conference on Power Electronics (IICPE)*, 2018, pp. 1-6. DOI: 10.1109/IICPE.2018.8709512
[9] O. Bingöl and B. Özkaya, "Analysis and comparison of different PV array configurations under partial shading conditions", *Solar Energy*, vol. 160, pp. 336-343, 2018. DOI: 10.1016/j.solener.2017.12.004
[10] S. Pareek, N. Chaturvedi, and R. Dahiya, "Optimal interconnections to address partial shading losses in solar photovoltaic arrays", *Solar Energy*, vol. 155, pp. 537-551, 2017. DOI: 10.1016/j.solener.2017.06.060
[11] V.Bala Raju and Ch. Chengaiah, "Performance Analysis of Conventional, Hybrid and Optimal PV Array Configurations of Partially Shaded Modules", *International Journal of Engineering and Advanced Technology (IJEAT)*, vol. 9, pp. 3061-3073, 2019. DOI: 10.35940/ijeat.A1661.109119
[12] Marcelo Gradella Villalva, Jonas Rafael Gazoli, and Ernesto Ruppert Filho, "Comprehensive approach to modeling and simulation of photovoltaic arrays", IEEE Transactions On Power Electronics, VOL. 24, NO. 5, May 2009, 1198–1208. DOI: 10.1109/TPEL.2009.2013862
[13] S. Pareek and R. Dahiya, "Power optimization of TCT configured PS-PV fields by forecasting the connection of modules", in *2015 Annual IEEE India Conference (INDICON)*, 2015, pp. 1-6. DOI: 10.1109/INDICON.2015.7443496
[14] H. S. Sahu and S. K. Nayak, "Power enhancement of partially shaded PV array by using a novel approach for shade dispersion", in *2014 IEEE Innovative Smart Grid Technologies - Asia (ISGT ASIA)*, 2014, pp. 498-503. DOI: 10.1109/ISGT-Asia.2014.6873842

[15] V.Bala Raju and Dr. Ch.Chengaiah "Modelling of solar PV array topologies under different partial shading conditions", in *2019 International Conference on Electrical, Communication, Electronics, Instrumentation and Computing (ECEIC)*, Kanchipuram · India, 2019.
[16] A. S. Yadav, R. K. Pachauri, Y. K. Chauhan, S. Choudhury, and R. Singh, "Performance enhancement of partially shaded PV array using novel shade dispersion effect on magic-square puzzle configuration", *Solar Energy*, vol. 144, pp. 780-797, 2017. DOI: 10.1016/j.solener.2017.01.011



Trends in Renewable Energy
OPEN ACCESS ISSN: 2376-2144
Peer-Reviewed Article futureenergysp.com/index.php/tre

# Statistical Channel Modeling of Overhead Low Voltage Broadband over Power Lines (OV LV BPL) Networks – Part 1: The Theory of Class Map Footprints of Real OV LV BPL Topologies, Branch Line Faults and Hook-Style Energy Thefts

Athanasios G. Lazaropoulos*

*School of Electrical and Computer Engineering / National Technical University of Athens / 9 Iroon Polytechniou Street / Zografou, GR 15780*

Received January 22, 2020; Accepted February 26, 2020; Published March 12, 2020

Due to the significant volatility of Broadband over Power Lines (BPL) networks regarding their circuital and topological characteristics, channel statistical modeling recently gains special attention from the BPL communications engineers. Among the recently presented channel attenuation statistical models, initial statistical hybrid model (iSHM) and modified statistical hybrid model (mSHM) have been theoretically defined and applied to overhead medium voltage (OV MV), underground medium voltage (UN MV) and overhead high voltage (OV HV) BPL networks so far. Apart from the iSHM and mSHM definition and application, the theory of the definition procedure of new virtual distribution and transmission BPL topologies, which describes the phases towards defining statistically equivalent BPL topologies and topology subclasses to the real indicative ones, has been demonstrated as well as the class maps, which are 2D capacity contour plots with respect to the channel attenuation statistical distributions (CASDs) parameters of iSHM and mSHM.

In this pair of papers, iSHM, mSHM, the definition procedure of new virtual BPL topologies and the class mapping are first applied to overhead low voltage (OV LV) BPL networks. Based on the class maps and the BPL topology database of Topology Identification Methodology (TIM), the required theory for illustrating the footprint of the real OV LV BPL topologies is first presented on class maps in this paper. On the basis of the class maps and the BPL topology database of Fault and Instability Identification Methodology (FIIM), the required theory for illustrating the footprint of the OV LV BPL topologies with branch line faults is first identified on class maps in this paper. On the basis of the class maps and the BPL topology database of hook style energy theft detection method (HS-DET method), the required theory for illustrating the footprint of the OV LV BPL topologies with a hook style energy theft is first demonstrated on class maps in this paper.

*Keywords: Smart Grid; Broadband over Power Lines (BPL) networks; Power Line Communications (PLC); Distribution and Transmission Power Grids; Capacity; Statistics; Modeling*

**Corresponding author:* AGLazaropoulos@gmail.com

Tr Ren Energy, 2020, Vol.6, No.1, 61-87. doi: 10.17737/tre.2020.6.1.00112

## Nomenclature

| | |
|---|---|
| AAAC | All Aluminum Alloy Conductor |
| AWGN | Additive White Gaussian Noise |
| BPL | Broadband over Power Lines |
| BPMN | Business Process Model and Notation |
| CASD | Channel Attenuation Statistical Distribution |
| CDF | cumulative density function |
| CS2 module | Coupling Scheme version 2 module |
| DHM | deterministic hybrid model |
| EMI | ElectroMagnetic Interference |
| FIIM | Fault and Instability Identification Methodology |
| FL noise model | Flat noise model |
| HS-DET method | hook style energy theft detection method |
| HV | High Voltage |
| ICT | Information and Communication Technology |
| IPSD limits | injected power spectral density limits |
| IP | Internet Protocol |
| iSHM | initial Statistical Hybrid Model |
| LOS | Line-of-Sight |
| LV | Low Voltage |
| L1PMA | L1 Piecewise Monotonic Approximation |
| MLE | Maximum Likelihood Estimator |
| mSHM | modified Statistical Hybrid Model |
| MTL | multiconductor transmission line |
| MtM | MultiWire-to-MultiWire |
| MV | Medium Voltage |
| OV | Overhead |
| PES | Percent Error Sum |
| PSD | Power spectral density |
| SG | Smart Grid |
| SHM | Statistical Hybrid Model |
| TIM | Topology Identification Methodology |
| TL | Transmission Line |
| TM2 method | Transmission Matrix version 2 method |
| UN | Underground |
| WtG | Wire-to-Ground |
| WtW | Wire-to-Wire |

## 1. Introduction

During the recent years, the traditional power grid, which represents an omnipresent widely branched hierarchical network structure and has been designed to facilitate the one-way power delivery from producers to consumers with relatively few one-way communications modalities is transformed into the smart grid, which is based on the traditional power grid infrastructure and may support two types of flows; say, a two-way power and a two-way information flow [1]-[3]. As the two-way information flow is concerned in this paper, the smart grid can be treated as an advanced IP-based communications network where a plethora of broadband applications can be supported that can facilitate either power utilities (*e.g.*, real-time monitor, meter and control of the power grid equipment and wired infrastructure) or customers (*e.g.*, real-time monitor and control of their power flows). To implement the two-way information flow across the smart grid, BPL technology attracts great attention from the stakeholders among the available communications technology proposals since it exploits the already installed wired power grid infrastructure [4]-[6]. However, transmission and distribution power grids have intentionally been designed to deliver power and for that reason power grids are a hostile medium for communications signals, such as BPL ones, through their infrastructure and equipment [7]-[11].

High and frequency-selective channel attenuation is considered as one of the critical inherent deficiencies of the BPL signal propagation and transmission across the power grid, thus requiring an accurate BPL channel model to be developed. So far, two main categories of BPL channel models are available: the deterministic and statistical BPL channel models. Here, it should be noted that statistical BPL channel models are based on the deterministic BPL channel models to a large degree. Hence, as the deterministic BPL channel attenuation modeling is first concerned, the relevant deterministic BPL channel models typically follow either a bottom-up approach or a top-down approach or hybrid approaches that synthesize the aforementioned bottom-up and top-down ones [7], [8], [12]-[23]. Among the available deterministic BPL channel models of the literature, DHM is selected for the analysis of this paper due to its exhaustive validation in various MTL configurations of transmission and distribution BPL networks [7], [8], [12], [24]-[30]. DHM consists of two interconnected modules, say: (i) the bottom-up approach module that is based on the formality of the MTL theory and its interaction with various similarity transformations; and (ii) the top-down approach module (TM2 method) that is based on the handling of the multidimensional transmission matrices of the cascaded BPL topologies of the examined BPL networks and topologies, the coupling scheme module, which determines the way that the BPL signal is injected/extracted onto/from power lines, and the capacity module that computes the highest information rate without errors that can be achieved in the examined BPL networks. Among the broadband performance metrics that are available as output from the DHM, channel attenuation and capacity are of interest during the application of the statistical BPL channel model of this pair of papers. Apart from the aforementioned deterministic framework, that is anyway required for the analysis of this pair of papers, the attention of BPL communications engineers and scientists regarding the BPL channel attenuation modeling has also been focused on statistical BPL channel models. So far, a great number of statistical BPL channel models, which are based on the results

of deterministic BPL channel models, has been proposed in a variety of BPL technology application fields [31]-[42]. SHM, which has been proposed in [35]-[37], is based on DHM and is hereafter applied. In fact, iSHM and mSHM, which are the two versions of the SHM, are both based on DHM while their simulation results may be considered as the statistically processed DHM numerical results through a set of appropriate CASDs; say, iSHM applies Gaussian, Lognormal, Wald, Weibull and Gumbel CASDs while mSHM applies Empirical CASD. By combining the channel attenuation results of DHM and CASDs through a six-phase flowchart procedure, iSHM and mSHM may give as output capacity ranges for given MTL configuration, IPSD limit, noise PSD level, coupling scheme and BPL topology subclass where a BPL topology subclass is uniquely characterized by its respective real indicative BPL topology and consists of statistically equivalent BPL topologies to the indicative one in terms of the MLE parameters of the applied CASDs (CASD MLEs). The capacity simulation results of iSHM and mSHM are based on real indicative BPL topologies whose topological results are well defined in terms of the topology length, the interconnections between branches / main lines, branch lengths, branch distances and branch terminations. Depending on the average value of their capacity range, BPL topology subclasses can be further classified into five BPL topology classes; say, LOS, rural, suburban, urban A and urban B BPL topology classes regardless of the type of power grid. In accordance with [36], [37], [45], it should be here noted that the capacity estimation success and the total simulation time of CASDs for given SHM version have been benchmarked for different transmission and distribution BPL networks revealing the strong dependence of the capacity estimation success on the applied CASD and SHM version. In fact, the definition procedure of virtual indicative BPL topologies, which has been analyzed in [43]-[45] and is hereafter simply denoted as definition procedure, enriches BPL topology classes with BPL topology subclasses whose respective virtual indicative BPL topologies are not defined in terms of the topology length, the interconnections between branches and main lines, branch lengths, branch distances and branch terminations but are only statistically defined in terms of the applied SHM version and its corresponding successful CASD MLEs. The definition procedure is a three-group eleven-step flowchart procedure that defines the MLE parameter ranges for given CASD and SHM version while its output is the class map, which is a 2D contour plot, that illustrates the borders between the BPL topology classes and corresponds each CASD MLE parameter pair to its BPL topology subclass average capacity for given power grid type, SHM version, CASD, coupling scheme, IPSD limits and noise levels. The simulation results of the definition procedure are presented for distribution and transmission BPL networks in [44] and [45], respectively, when the most successful CASDs for given SHM version are adopted.

In this set of papers, iSHM, mSHM, the definition procedure and the class maps are first applied to OV LV BPL networks. By exploiting the already acquired application experience of SHM to OV MV, UN MV and OV HV BPL networks [36], [37], [45], new results are provided for OV LV BPL topologies thus: (i) revealing the most successful CASD among the aforementioned ones for iSHM and mSHM; and (ii) benchmarking the performance of iSHM and mSHM.

But the main contribution of this set of papers is the proposal of the footprint areas on the class maps, hereafter simply denoted as footprints, that allows the impact investigation of critical events that may occur during the operation of OV LV power

grids. To determine a footprint in the class maps, the OV LV BPL topology databases of three smart grid broadband applications that are supported by the BPL technology (*e.g.*, TIM [46], FIIM [46] and HS-DET method [47]) are here retrieved and applied. First, since the class maps are 2D contour plots that are curved with respect to CASD MLEs for given CASD, the average capacity results of all the possible BPL topology subclasses are grouped among the five BPL topology classes and are demonstrated on class maps into five BPL topology class areas. By exploiting the BPL topology database of TIM that contains all the possible real OV LV BPL topologies, respective OV LV BPL subclasses are defined and their average capacities are computed with respect to the most successful CASDs of iSHM and mSHM. Then, the footprint of the real OV LV BPL topologies is going to be first illustrated on the class maps thus separating the real OV LV BPL topology footprint from the virtual one. Second, a critical issue concerning the supply security and the fine operation of the OV LV power grid is the immediate response and repair to faults that may occur across the OV LV power grid infrastructure. In this paper, by exploiting the BPL topology database of FIIM, the impact of a single branch line fault across an OV LV BPL topology is first assessed through the footprint of the OV LV BPL topologies with branch line faults on class maps for given indicative OV LV BPL topology. Third, energy theft defines a multi-billion problem for power utility companies either in traditional power systems or in the emerging smart grid. In this paper, by exploiting the BPL topology database of HS-DET method, the impact of the hook style energy theft across an OV LV BPL topology is first assessed through the footprint of the OV LV BPL topologies with a single hook for energy theft on class maps for given indicative OV LV BPL topology. In this paper, the theory that is required for the introduction of the footprint concept for real OV LV BPL topologies, OV LV BPL topologies with branch line faults and OV LV BPL topologies with hook-style energy thefts is detailed.

The rest of this paper is organized as follows: In Section II, the OV LV MTL configuration is presented as well as the real indicative OV LV BPL topologies of this pair of papers. Section III summarizes the basics of DHM, iSHM, mSHM, the definition procedure and the class maps as well as the required settings for their default operation during the study of OV LV BPL topologies. Section IV briefly presents TIM, FIIM and HS-DET method as well as the required settings for the update of the respective databases. Also, the theory concerning the iSHM and mSHM class maps footprints of real OV LV BPL topologies, of OV LV BPL topologies with branch line faults and of OV LV BPL topologies with hook-style energy thefts is carefully presented. Section V concludes this paper.

## 2. OV LV MTL Configuration and Indicative OV LV BPL Topologies

Due to the physical properties of OV LV TLs and the involved power grid equipment, the BPL signal propagation and transmission across the OV LV power grid considerably differs from the one of well-known communications media such as twisted-pair, coaxial or fiber-optic cables. This Section presents the applied OV LV MTL configuration and indicative OV LV BPL topologies that mainly affect the BPL signal propagation and transmission, respectively.

## 2.1 OV LV MTL Configuration

In Fig. 1(a), the typical OV LV MTL configuration that is examined in this paper is illustrated. The examined OV LV MTL configuration consists of four parallel non-insulated conductors (*i.e.*, $n^{\mathbf{OVLV}} = 4$), which are spaced each other by a vertical distance $\Delta_{\mathrm{OVLV}}$ in the range from 0.3m to 0.5m. The upper conductor of radius $r_{\mathrm{OVLV,n}}$ is the neutral one, while the lower three conductors of radius $r_{\mathrm{OVLV,p}}$ stand for the three phases.

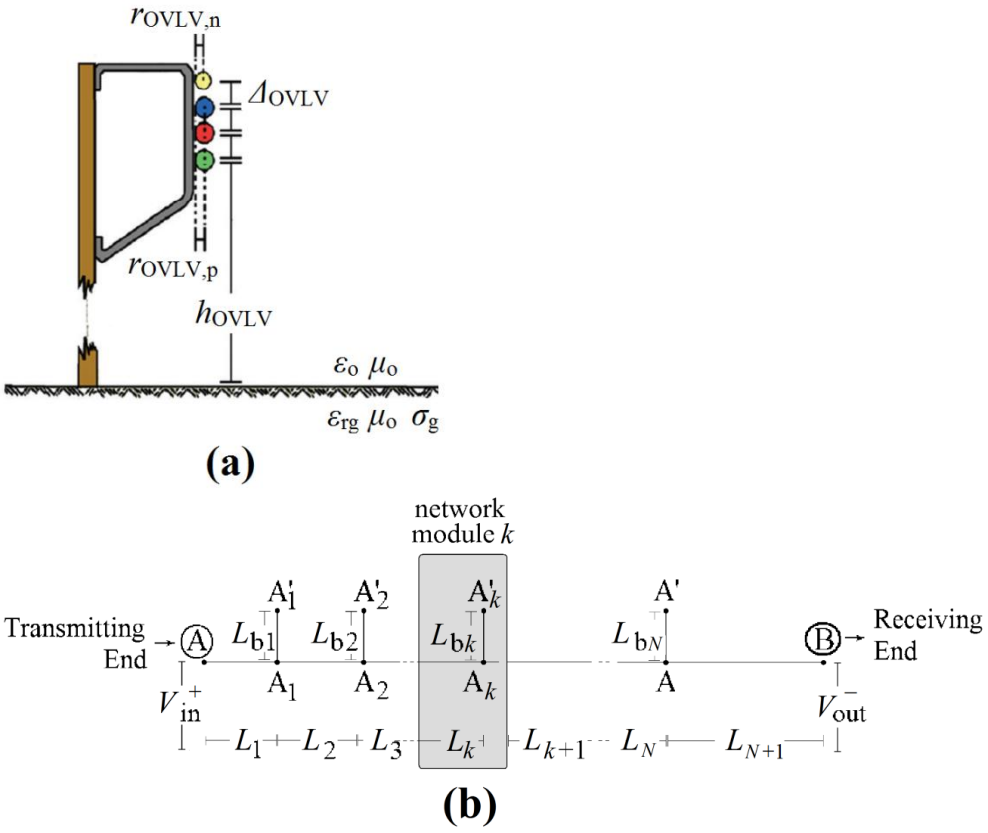


**Fig. 1**. (a) OV LV MTL configuration [12]. Typical OV LV BPL topology with *N* branches [35].

Note that the lowest phase conductor is hung at height $h_{\mathrm{OVLV}}$ in the range from 6 m to 10 m above the ground. As the dimension, the material and the structure of conductors are concerned, the three-phase four-conductor OV LV MTL configuration consists of 3×54.6 mm$^2$+1×34.4 mm$^2$ AAACs [12], [48]. The ground is considered as the reference conductor with conductivity $\sigma_{\mathrm{g}}$ and relative permittivity $\varepsilon_{\mathrm{rg}}$ that are equal to 5 mS/m and 13, respectively [7], [12], [15], [23], while the impact of imperfect lossy ground on BPL signal propagation over OV power lines has been analyzed in [49]-[51].

## 2.2 Real Indicative OV LV BPL Topologies

To study OV LV BPL networks, each network is assumed to be divided into cascaded OV LV BPL topologies. A typical OV LV BPL topology is illustrated in Fig. 1(b). Each OV LV BPL topology is bounded by the transmitting and receiving ends

where BPL devices, such as BPL signal injector, BPL signal extractor and BPL signal repeater, are installed depending on the relative location of the topology across the network. Across the BPL signal transmission path, $N$ branches with their respective terminations may be encountered. The arbitrary $k$ branch has length equal to $L_{bk}$, $k$=1,…,$N$ and is located at distance $\sum_{i=1}^{k} L_{bk}$ from the transmitting end. In accordance with TM2 method of DHM [12], [24], each OV LV BPL topology is treated as a concatenation of $N$+1 network modules; say, each of the first $N$ network modules comprises the $k$ branch and the TL of length $L_k$, which is the distance between the examined branch and its previous one, while the last network module only comprises the TL of length $L_{N+1}$, which is the distance between the last branch and the receiving end.

In accordance with [12], [47], [52]-[54], five OV LV BPL topology classes (*i.e.*, LOS, rural, suburban, urban A and urban B) with their respective representative BPL topologies can be defined so that a thorough study of all OV LV BPL topologies may be fulfilled during DHM application. In Table 1, the representative OV LV BPL topologies of the respective five OV LV BPL topology classes (real indicative OV LV BPL topologies) are reported in the case of DHM as well as their topological characteristics. Similarly, when SHM is applied the representative OV LV BPL topologies of Table 1 act as the representative ones for the respective main subclasses of the OV LV BPL topology classes. The selection of the main subclass for given OV LV BPL topology class remains critical during the preparation of class maps since its capacity influences the capacity boundaries among the topology classes.

## 3. The Basics of DHM, SHM, Definition Procedure and Class Maps

Class maps, which are the main graphical metric in order to access the case studies of this pair of papers, are the output of the definition procedures of iSHM and mSHM, which are anyway the two versions of SHM. Apart from the required statistical processing, SHM is based on DHM results that are the channel attenuation and the capacity. In this Section, a brief synopsis of DHM, SHM, definition procedure and class maps is provided as well as their interoperability.

### 3.1 DHM

In this paper, DHM can be treated as the module concatenation of the bottom-up, the top-down, the coupling scheme and the capacity computation modules.

On the basis of its first two interconnected modules, say, the bottom-up and the top-down approach module, several useful intermediate metrics, among them is the line channel transfer function matrix, may be calculated by DHM for given OV LV MTL configuration and OV LV BPL topology. Since $n^{\mathrm{OVLV}}$ phase conductors that are greater than 2 are encountered in OV LV MTL configurations, the standard TL analysis is extended by DHM to the MTL analysis. Extensively been analyzed in [7], [8], [12], [25], [26], [27], [52], [55]-[58], bottom-up module of DHM computes the $n^{\mathrm{OVLV}}$ modes that are supported and propagate across the OV LV MTL configurations in the frequency range of interest. By receiving the results of the bottom-up module and applying TM2 method of the top-down module, the $n^{\mathrm{OVLV}} \times n^{\mathrm{OVLV}}$ line channel transfer function matrix $\mathbf{H}\{\cdot\}$ that relates line quantities with modal ones is given by

$$\mathbf{H}^{\mathrm{OVLV}}\{\cdot\} = \mathbf{T}_V^{\mathrm{OVLV}} \cdot \mathbf{H}^{\mathrm{OVLV,m}}\{\cdot\} \cdot \left(\mathbf{T}_V^{\mathrm{OVLV}}\right)^{-1} \quad (1)$$

where $\mathbf{H}^{\mathrm{OVLV,m}}\{\cdot\}$ is the $n^{\mathrm{OVLV}} \times n^{\mathrm{OVLV}}$ modal channel transfer function matrix that mainly depends on the examined OV LV MTL configuration and OV LV BPL topology and $\mathbf{T}_V^{\mathrm{OVLV}}$ is a $n^{\mathrm{OVLV}} \times n^{\mathrm{OVLV}}$ matrix that depends on the frequency, the physical properties of the TLs and the geometry of the OV LV MTL configuration.

As the line channel transfer function matrix is computed by the top-down module of DHM, the coupling scheme module can implement different coupling schemes that define the practical way that the signals are injected into and extracted from the TLs of the OV LV BPL networks. With reference to [29], [59], CS2 module, which is the most

**Table 1**
Representative OV LV BPL Topologies (Real indicative OV LV BPL Topologies) for DHM and SHM

| OV LV BPL Topology Class | OV LV BPL Topology Name (and OV LV BPL Topology Subclass Name) | Number of Branches (*N*) | Length of Main Lines | Length of Branches |
|---|---|---|---|---|
| Typical urban topology class | Urban case A (main subclass) | 3 | $L_1$=500m, $L_2$=200m, $L_3$=100m, $L_4$=200m | $L_{b1}$=8m, $L_{b2}$=13m, $L_{b3}$=10m |
| Aggravated urban topology class | Urban case B (main subclass) | 5 | $L_1$=200m, $L_2$=50m, $L_3$=100m, $L_4$=200m, $L_5$=300m, $L_6$=150m | $L_{b1}$=12m, $L_{b2}$=5m, $L_{b3}$=28m, $L_{b4}$=41m, $L_{b5}$=17m |
| Suburban topology class | Suburban case (main subclass) | 2 | $L_1$=500m, $L_2$=400m, $L_3$=100m | $L_{b1}$=50m, $L_{b2}$=10m |
| Rural topology class | Rural case (main subclass) | 1 | $L_1$=600m, $L_2$=400m | $L_{b1}$=300m |
| LOS topology class | LOS case (main subclass) | 0 | $L_1$=1000m | - |

recently upgraded coupling scheme module for BPL networks, is adopted in this paper. CS2 module can describe the BPL signal coupling procedure using two interfaces, namely: (i) BPL signal injection; and (ii) BPL signal extraction interface while it can support three types of coupling schemes for the OV LV BPL networks, namely: (1) *Coupling Scheme Type 1: WtG* coupling scheme; (2) *Coupling Scheme Type 2: WtW* coupling scheme; and (3) *Coupling Scheme Type 3: MtM* coupling scheme. With reference to eq. (1), CS2 module computes the coupling scheme channel transfer function that relates output and input BPL signal through

$$H^{\mathrm{OVLV},c}\{\cdot\} = [\mathbf{C}^{\mathrm{out}}]^{\mathrm{OVLV},c} \cdot \mathbf{H}^{\mathrm{OVLV}}\{\cdot\} \cdot [\mathbf{C}^{\mathrm{in}}]^{\mathrm{OVLV},c} \quad (2)$$

for given coupling scheme where $[\cdot]^c$ denotes the applied coupling scheme, $\mathbf{C}^{\mathrm{in}}$ is the input coupling $n^{\mathrm{OVLV}} \times 1$ column vector that deals with the BPL signal injection interface and $\mathbf{C}^{\mathrm{out}}$ is the ouput coupling $1 \times n^{\mathrm{OVLV}}$ line vector that deals with the BPL signal extraction interface. Different coupling schemes involve different conductors of the examined OV LV MTL configuration and entail corresponding power restrictions and thus corresponding $\mathbf{C}^{\mathrm{in}}$ and $\mathbf{C}^{\mathrm{out}}$ as explained in [59], [29].

As the coupling scheme channel transfer function is well defined by eq.(2) for given coupling scheme, the last module of DHM is the capacity one that computes the maximum achievable transmission rate that can be reliably transmitted for given OV LV BPL topology and remains the crucial measure for the class maps. Apart from the

coupling scheme channel transfer function of eq. (2), two other critical parameters (*i.e.*, IPSD limits and noise PSD levels) should be defined so that the capacity of a given OV LV BPL topology can be determined, namely:

- *IPSD limits*: Since BPL systems operate in a common frequency range with other already licensed communications services, by adopting suitable IPSD limits the unintentional EMI to the other already licensed communications services (*e.g.*, aeronautical radionavigation, radio astronomy, mobile satellite and maritime mobile) can be significantly mitigated. Among the most noted proposals that define suitable EMI policies and thus respective IPSD limits are FCC Part 15, German Reg TP NB30 and the BBC / NATO Proposal. More analytically, the electric field strength limits proposed by the aforementioned proposals are presented in [10], [60], [61] while the respective IPSD limits are determined in [61] for OV BPL networks.
- *Noise PSD levels*: OV BPL networks suffer from colored background and impulsive noise [7], [12], [25], [27], [52], [53], [55], [56]. However, FL noise model of [62] suggests that the assumption of AWGN PSD levels can remain a simple but accurate noise approximation during the capacity computations of OV LV BPL networks in the 3-30MHz frequency that is anyway the frequency range of interest of this paper. Hence, the AWGN PSD level of OV LV BPL networks that is adopted in this paper is assumed to be equal to –60 dBm/Hz.

Since the coupling scheme channel transfer function, IPSD limits and noise PSD levels are well defined for given MTL configuration, OV LV BPL topology, applied coupling scheme, EMI policy and the noise environment, the capacity $C$ is given by [52], [55], [56]

$$C = f_s \sum_{q=1}^{Q} \log_2 \left\{ 1 + \left[ \frac{\langle p(f_q) \rangle_L}{\langle N(f_q) \rangle_L} \cdot \left| H^{\mathrm{OVLV,C}}(f_q) \right|^2 \right] \right\} \quad (3)$$

$$f_q = 3\mathrm{MHz} + (q-1) \cdot f_s,\ q = 1, \ldots, Q \quad (4)$$

$$\mathbf{f} = [f_1 \quad \cdots \quad f_q \quad \cdots \quad f_Q],\ q = 1, \ldots, Q \quad (5)$$

where $f_q$ is the flat-fading subchannel start frequency, $f_s$ is the flat-fading subchannel frequency spacing, $Q$ is the number of subchannels in the examined 3-30 MHz frequency range, $\mathbf{f}$ is the $1 \times Q$ line vector that consists of the flat-fading subchannel start frequencies $f_q$, $p(\cdot)$ is the applied IPSD limits in dBm/Hz, $N(\cdot)$ is the applied AWGN PSD levels in dBm/Hz and $\langle \cdot \rangle_{\mathbf{L}}$ is an operator that converts dBm/Hz into a linear power ratio (W/Hz).

## 3.2 SHM

SHM, which consists of iSHM and mSHM that are its two versions, has been proposed in [35]-[37]. SHM exploits the deterministic results of DHM while SHM can be considered as a statistical BPL channel model with its recent application to various transmission and distribution BPL networks of interest [35]-[37]. The BPMN diagrams of iSHM and mSHM that describe their operation and the transformation of the DHM deterministic results to the SHM simulation results of this paper are demonstrated in Figs. 2(a) and 2(b), respectively. Either iSHM or mSHM consists of six Phases (Phase A-F) while each Phase is graphically constrained by a grey container and is characterized by its corresponding procedure and produced files shown in light blue color. The red elements of the BPMN diagrams are analyzed in Sec.3.3 since these are modifications required by the definition procedure. Significant similarities and

differences between iSHM and mSHM occur and they are analytically highlighted in this subsection.

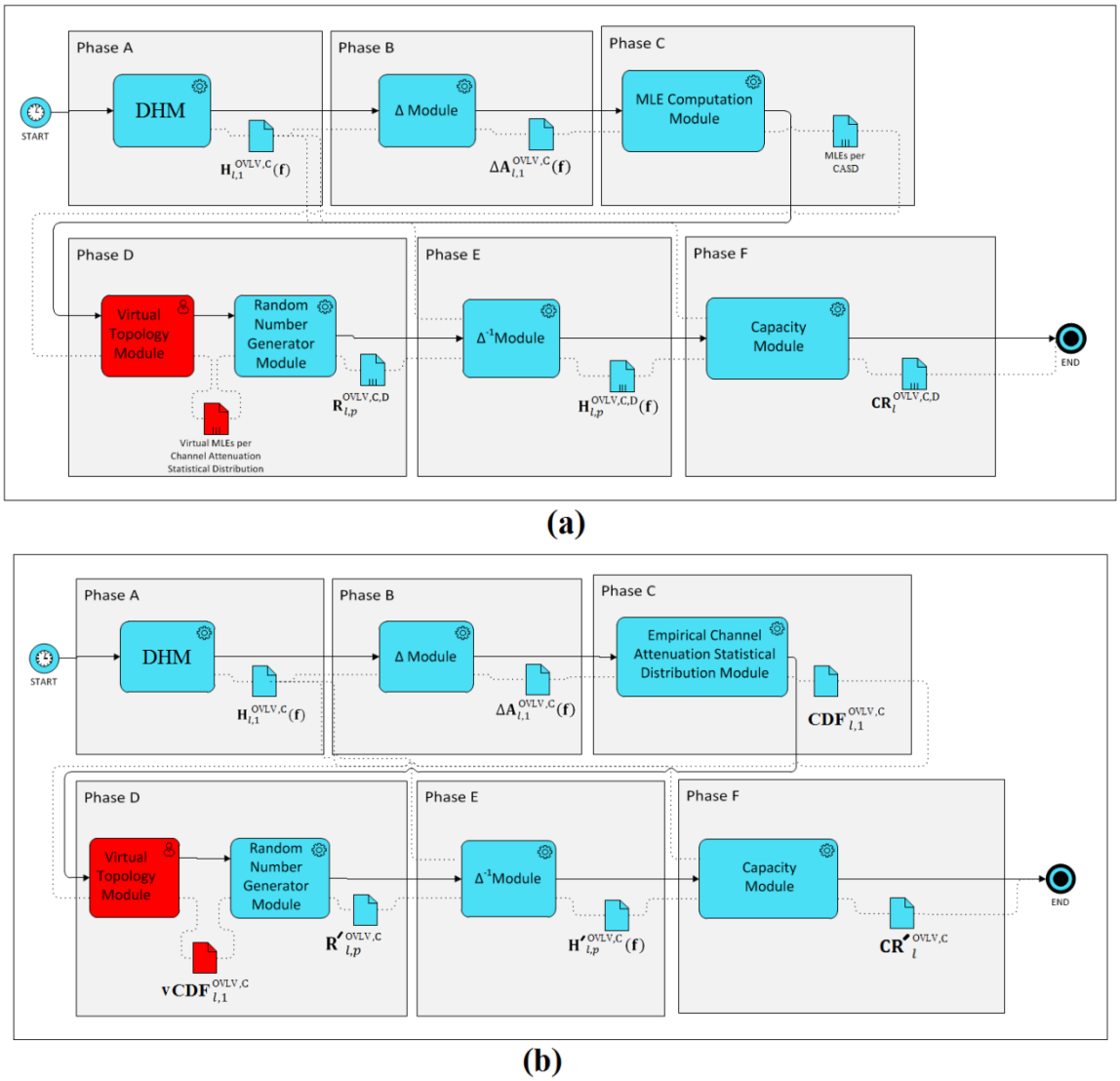


**Fig. 2**. BPMN diagrams of SHM. (a) iSHM [35]. (b) mSHM [37].

In accordance with [35] and with reference to Fig. 2(a), the operation of iSHM can be described through the concatenation of the Phases A-F. More specifically, Phase A of iSHM deals with the bottom-up, the top-down and the coupling scheme modules of DHM by taking as input the $l$ real indicative OV LV BPL topology of Table 1, its corresponding OV LV MTL configuration and the applied coupling scheme while it gives as output the $1\times Q$ coupling scheme channel transfer function line vector $\mathbf{H}_{l,1}^{\mathrm{OVLV,C}}(\mathbf{f})$. As the coupling scheme channel transfer function line vector is well delivered, Phase B of iSHM computes the $1\times Q$ channel attenuation difference line vector $\Delta\mathbf{A}_{l,1}^{\mathrm{OVLV,C}}(\mathbf{f})$ of the $l$ real indicative OV LV BPL topology with respect to the LOS case for given

coupling scheme through its Δ module. Then, Phase C of iSHM computes the MLEs of the supported iSHM CASDs (*i.e.*, Gaussian, Lognormal, Wald, Weibull and Gumbel CASDs) by applying MLE computation module for given channel attenuation difference line vector. Note that the MLE estimation method of the five supported iSHM CASDs is presented in Appendix A of [35] as well as the respective CDFs. By deploying the random number generator module, Phase D of iSHM gives as output the 1×*Q* random number line vector $\mathbf{R}_{l,p}^{\mathrm{OVLV,C,D}}$ for given indicative OV LV BPL topology and coupling scheme where $[\cdot]^{\mathrm{D}}$ denotes the applied CASD and *p*, *p*=1,…,*P*+1 is the member number in the OV LV BPL topology main subclass. Thus, each OV LV BPL main subclass finally comprises its real indicative OV LV BPL topology (*p*=1), which is one of the first four OV LV BPL topologies of Table 1, and *P* statistically equivalent virtual OV LV BPL topologies in terms of the CASD MLEs of the real indicative OV LV BPL topology. Phase E of iSHM performs the inverse procedure of Phase B through its $\Delta^{-1}$ module by computing 1×*Q* coupling scheme channel transfer function line vector $\mathbf{H}_{l,p}^{\mathrm{OVLV,C,D}}(\mathbf{f})$ of each of the *P* members of each BPL topology main subclass for the examined coupling scheme and CASD. Finally, Phase F of iSHM computes the capacity range $\mathbf{CR}_{l}^{\mathrm{OVLV,C,D}} = [min\{\mathbf{C}_{l}^{\mathrm{OVLV,C,D}}\} \;\; average\{\mathbf{C}_{l}^{\mathrm{OVLV,C,D}}\} \;\; max\{\mathbf{C}_{l}^{\mathrm{OVLV,C,D}}\}]$ of each OV LV BPL topology main subclass for given coupling scheme and CASD by applying capacity module of DHM where

$$\mathbf{C}_{l}^{\mathrm{OVLV,C,D}} = [C_{l,1}^{\mathrm{OVLV,C,D}} \;\; \cdots \;\; C_{l,p}^{\mathrm{OVLV,C,D}} \;\; \cdots \;\; C_{l,P+1}^{\mathrm{OVLV,C,D}}],\ p=1,\ldots,P+1 \tag{6}$$

is the capacity line vector of the examined OV LV BPL topology main subclass, $C_{l,p}^{\mathrm{OVLV,C,D}}$ is the capacity of the *p* member of the examined OV LV BPL topology main subclass, $min\{\cdot\}$, $average\{\cdot\}$ and $max\{\cdot\}$ computes the minimum, the average and the maximum value of an array, respectively. More details concerning the operation of iSHM are given in [35].

In accordance with [37] and with reference to Fig. 2(b), the operation of mSHM can be described by revealing the similarities and the differences between mSHM Phases and the respective ones of iSHM. Phases A and B of mSHM remain the same with the respective Phases of iSHM. The main differences between mSHM and iSHM are concentrated in Phases C and D; since mSHM adopts the Empirical CASD instead of the five CASDs of iSHM, the Empirical channel attenuation statistical distribution module is deployed in Phase C for mSHM that receives as input the coupling scheme channel attenuation difference and it gives as output the Empirical CDF of the coupling scheme channel attenuation difference $\mathbf{CDF}_{l,1}^{\mathrm{OVLV,C}}$ for given OV LV BPL topology and coupling scheme. Then, the random number generator of mSHM Phase D gives as output the random number 1×*Q* line vector $\mathbf{R}'^{\mathrm{OVLV,C}}_{l,p}$ for given coupling scheme and indicative distribution BPL topology after the inverse interpolation to achieve the Empirical CDF projection of the random values taken by Phase C. Similarly to iSHM, mSHM Phase E computes the 1×*Q* coupling scheme channel transfer function line vector $\mathbf{H}'^{\mathrm{OVLV,C}}_{l,p}(\mathbf{f})$ of each of the *P* members of each BPL topology main subclass for the examined coupling scheme while mSHM Phase F computes the capacity range $\mathbf{CR}'^{\mathrm{OVLV,C}}_{l}$ of each OV LV BPL topology main subclass for given coupling scheme in accordance with the iSHM capacity range $\mathbf{CR}_{l}^{\mathrm{OVLV,C,D}}$ and eq. (6) when Empirical CASD is applied.

### 3.3 The Definition Procedure and Class Maps

In accordance with Sec. 3.2., when the topological and circuital characteristics of real OV LV BPL topologies are available, iSHM and mSHM may define the respective BPL topology subclasses and compute the corresponding capacity ranges. As already been identified in [43]-[45], the underrepresentation of the BPL topology classes during the BPL statistical channel modelling can be mitigated through the insertion of virtual indicative BPL topologies and their respective subclasses through the adoption of the definition procedure. In [43], the theoretical framework of the definition procedure has been detailed while in Figs. 3(a) and 3(b) the flowcharts of the definition procedure of iSHM and mSHM are demonstrated, respectively. Note that the definition procedure imposes the operation of virtual topology module with its corresponding file output (*i.e.*, red elements of BPMN diagrams) in Figs. 2(a) and 2(b) for iSHM and mSHM, respectively.

In accordance with [43] and with reference to Fig. 3(a), iSHM definition procedure flowchart consists of eleven steps; nine of them (*i.e.*, FL1.02-FL1.10) are categorized into three groups (*i.e.*, Group 1.A-1.C) while the first and eleventh steps (*i.e.*, FL1.01 and FL1.11) deal with the definition of main subclasses and the graphical preparation of class maps, respectively. Since the real indicative OV LV BPL topologies of main subclasses of Table 1 have already been delivered by the step FL1.01, Group 1.A computes the capacities of these topologies $C_l^{\mathrm{OVLV,C}}, l = 1,2,3,4,5$ and the capacity borders between the adjacent OV LV BPL topology classes $CBo_l^{\mathrm{OVLV,C}}, l = 1,2,3,4$ in accordance with eq.(1) of [43]. At the same time, Group 1.B, which consists of five steps (*i.e.*, FL1.04-FL1.08), first computes each MLE pair ($MLE\_1_l^{\mathrm{OVLV,C,D}}$ and $MLE\_2_l^{\mathrm{OVLV,C,D}}, l = 1,2,3,4,5$) of the real indicative OV LV BPL topologies of the main subclasses per CASD at step FL1.04. Second, the step FL1.05 of Group 1.B defines the presentation resolution of the upcoming class maps by computing the length of horizontal spacings $\Delta MLE\_1_l^{\mathrm{OVLV,C,D}}$, $l = 1,2,3,4,5$ and of vertical spacings $\Delta MLE\_2_l^{\mathrm{OVLV,C,D}}, l = 1,2,3,4,5$ by taking into account the number of spacings for the horizontal axis $no\_1$ and vertical axis $no\_2$, respectively. Third, step FL1.06 computes all $(no\_1 + 1) \times (no\_2 + 1)$ MLE pair combinations of the virtual indicative OV LV BPL topologies of virtual subclasses per CASD $\left[vMLE\_1_{l,k\ no\ 1}^{\mathrm{OVLV,C,D}} \quad vMLE\_2_{l,k\ no\ 1}^{\mathrm{OVLV,C,D}}\right], k\_no\_1 = 0,1,\cdots,no\_1, k\_no\_2 = 0,1,\cdots,no\_2$ by taking into consideration the horizontal spacings $\Delta MLE\_1_l^{\mathrm{OVLV,C,D}}$ and vertical ones $\Delta MLE\_2_l^{\mathrm{OVLV,C,D}}$ –see eqs. (4) and (5) of [43]. Fourth, step FL1.07 activates the random number generator of Phase D of Fig.2(a) that exploits the MLE pair combinations of the virtual indicative OV LV BPL topologies of virtual subclasses per CASD while *P* members for each virtual OV LV BPL topology subclass are generated and added. Fifth, by activating the operation of Phases E and F of iSHM of Fig. 2(a), FL1.08 computes the average capacity value $\mathrm{average}\{\ C_{l,k\ no\ 1,k\ no\ 2}^{\mathrm{OVLV,C,D}}\ \}$, $k\_no\_1 = 0,1,\cdots,no\_1$, $k\_no\_2 = 0,1,\cdots,no\_2$ of each virtual OV LV BPL topology subclass. By deploying Group 1.C, step FL1.09 receives as input all the $(no\_1 + 1) \times (no\_2 + 1)$ MLE pair combinations of the virtual indicative OV LV BPL topologies of virtual subclasses per CASD

$\left[vMLE\_1_{l,k\ no\ 1}^{\mathrm{OVLV,C,D}} \quad vMLE\_2_{l,k\ no\ 1}^{\mathrm{OVLV,C,D}}\right], k\_no\_1 = 0,1,\cdots,no\_1, k\_no\_2 = 0,1,\cdots,no\_2$

from the step FL1.06 of Group 1.B and provides the minimum and maximum values of horizontal and vertical axes of the 2D contour plot of the class map per CASD (*i.e.*, CASD parameter mapping) while the step FL1.10 receives as input the CASD parameters from step FL1.09 and the average capacity values average{ $C_{l,k\ no\ 1,k\ no\ 2}^{\mathbf{OVLV,C,D}}$ }, $k\_no\_1 = 0,1,\cdots,no\_1$, $k\_no\_2 = 0,1,\cdots,no\_2$ of all possible virtual OV LV BPL topology subclasses from step FL1.08 of Group 1.B and provides the existing CASD parameter map enriched with the average capacities of all possible virtual OV LV BPL topology subclasses. Finally, by synthesizing its inputs into a 2D contour plot, step FL1.11 receives the CASD parameter map from Group1.C and the capacities of

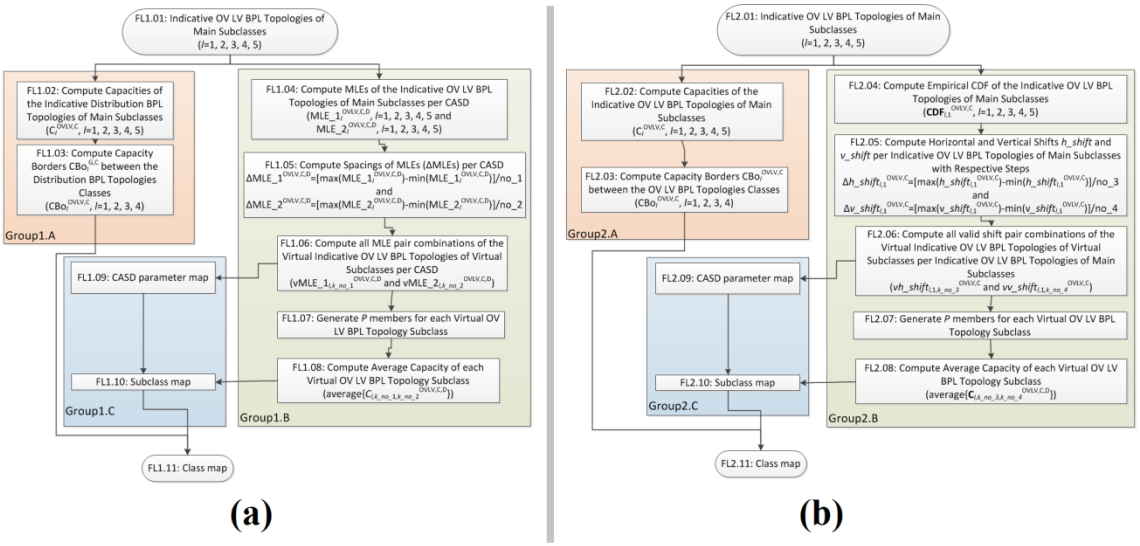


**Fig. 3**. Definition procedure flowcharts [43]. (a) iSHM. (b) mSHM.

the real indicative OV LV BPL topologies of main subclasses accompanied with the capacity borders between the adjacent OV LV BPL topology classes from Group1.A while step FL1.11 gives as output the class map that is the result of the definition procedure of iSHM.

Similarly to Sec.3.2, in accordance with [43] and with reference to Fig. 3(b), the operation of mSHM definition procedure can be described by simply highlighting the similarities and the differences between mSHM steps and groups and the respective ones of iSHM. Since the initialization of the definition procedure deals with the insertion of the real indicative OV LV BPL topologies of main subclasses of Table 1, step FL2.01 of mSHM and step FL1.01 remain the same. Also, Group 2.B of mSHM that consists of steps FL2.02 and FL2.03 deals with the capacities of the real indicative OV LV BPL topologies and the capacity borders between the adjacent OV LV BPL topology classes without any differences from the operation of Group 1.A of iSHM. The main differences between mSHM and iSHM definition procedures are concentrated in Group 2.B of mSHM and Group 1.B of iSHM; since mSHM adopts the Empirical CASD instead of the five CASDs of iSHM, step FL2.04 first computes the Empirical CDFs $\mathbf{CDF}_{l,1}^{\mathbf{OVLV,C}}, l = 1,2,3,4,5$ of the real indicative OV LV BPL topologies of main

subclasses. Then, step FL2.05 computes the repetition horizontal step $\Delta h\_shift_{l,1}^{\mathrm{OVLV,C}}, l = 1,2,3,4,5$ and vertical step $\Delta v\_shift_{l,1}^{\mathrm{OVLV,C}}, l = 1,2,3,4,5$ with respect to eqs. (6) and (7) of [43] by taking into account the spacing of the horizontal shift $h\_shift_{l,1}^{\mathrm{OVLV,C}}$ and vertical shift $v\_shift_{l,1}^{\mathrm{OVLV,C}}$ of the Empirical CDFs of the real indicative OV LV BPL topologies of main subclasses where $no\_3$ and $no\_4$ are the number of spacings for the horizontal and vertical axis, respectively. Afterwards, step FL2.06 computes all $(no\_3+1)\times(no\_4+1)$ shift pair combinations of the virtual indicative OV LV BPL topologies of virtual subclasses $\left[vh\_shift_{l,1,k\ no\ 3}^{\mathrm{G,C}} \quad vv\_shift_{l,1,k\ no\ 4}^{\mathrm{G,C}}\right], k\_no\_3 = 0,1,\cdots,no\_3, k\_no\_4 = 0,1,\cdots,no\_4$ by taking into consideration the repetition horizontal step $\Delta h\_shift_{l,1}^{\mathrm{OVLV,C}}$ and vertical one $\Delta v\_shift_{l,1}^{\mathrm{OVLV,C}}$ –see eqs. (8) and (9) of [43]–. In fact, the aforementioned repetition steps and shifts are used so that the Empirical CDF of the virtual OV LV BPL topologies of subclasses can be computed with respect to the Empirical CDFs of the real indicative OV LV BPL topologies of main subclasses. Similarly to the steps of Group 1.B of iSHM definition procedure, step FL2.07 exploits the random number generator of Phase D of Fig. 2(b), step FL2.08 enriches each virtual OV LV BPL topology subclass with *P* members and step FL2.09 computes the average capacity values $\mathrm{average}\{C_{l,k\ no\ 3,k\ no\ 4}^{\mathrm{OVLV,C,D}}\}$, $k\_no\_3 = 0,1,\cdots,no\_3$, $k\_no\_4 = 0,1,\cdots,no\_4$ of all possible virtual OV LV BPL topology subclasses of step FL2.08. As the Group 2.C and the step FL2.11 of mSHM definition procedure are concerned, these remain the same with the respective Group 1.C and step FL1.11 of iSHM definition procedure with the only difference that the axes of mSHM class maps that anyway the primary result of the described procedure comprise horizontal and vertical shifts while in the case of iSHM, the axes of iSHM class maps comprise CASD MLEs.

## 3.4 Default Operation Settings for DHM, iSHM, mSHM, Definition Procedures and Class Maps

Since DHM, iSHM, mSHM, definition procedures and class maps support an interconnected system, a set of default operation settings, which have already been reported in [35]-[37], are simply reported in this paper.

As the default operation settings for DHM are assumed, these are further divided into two categories; say, the topological and circuital operation setting categories. In the case of the default topological operation setting category, the real indicative OV LV BPL topologies that concern average long end-to-end connections of 1000m have already been presented in Table 1. In the case of the default circuital operation settings, these have explicitly been detailed in [7], [8], [12], [15]-[17], [23], [25]-[27], [48], [52], [53], [55], [56], [63]-[72]. The default circuital operation settings comprise four assumptions regarding the interpretation of the indicative OV LV BPL topologies from DHM, namely: (i) the branching and distribution cables are assumed identical; (ii) the interconnections between the distribution and branch conductors are fully activated; (iii) the transmitting and the receiving ends are assumed to be matched to the characteristic impedance of the supported modal channels; and (iv) the branch terminations are treated as open circuit terminations.

As the default operation settings for iSHM are assumed, these operation settings can be further divided into seven categories as already been outlined in [36], [44], namely: (i) *BPL operation frequency range*: The BPL operation frequency range that is considered in this paper is equal to 3-30 MHz while 270 subchannels of 0.1MHz frequency spacing (i.e, $f_s$ =0.1 MHz) are considered so that the assumption of the flat-fading subchannels, which is a typical scenario during the capacity computations in BPL channels, is valid [25]-[27], [30], [52], [56]; (ii) *Default coupling scheme system*: Already been mentioned in Sec.3.1, CS2 module, which has been detailed in [29], [59], can be considered as the default DHM coupling scheme module. Among the available coupling schemes that are supported by CS2 module, only WtG[1] coupling scheme is assumed to be the default one so that a direct comparison between the results of this paper and those of [36] and [37], can be performed; (iii) *Computation of the coupling scheme channel attenuation differences*: To prevent the appearance of infinite terms during the application of Lognormal, Wald and Weibull CASDs in iSHM, the coupling scheme channel attenuation differences are assumed to be equal to an arbitrarily low value, say $1\times10^{-11}$, when zero or negative coupling scheme channel attenuation differences rarely occur; (iv) *Members of each BPL topology subclass*: 100 member OV LV BPL topologies (*i.e.*, *P*=100) are going to be added in each BPL topology subclass per CASD in iSHM Phase D of Fig. 2(a); (v) *IPSD limits*: In accordance with Sec.3.1, FCC Part 15 is assumed to be the default EMI policy in this paper. In the frequency range 3-30MHz of interest, -60 dBm/Hz are the FCC Part 15 IPSD limits $p(\cdot)$ suitable for the operation of OV LV BPL networks [25], [26], [73]; (vi) *Noise PSD levels*: Already been mentioned in Sec.3.1, FL noise model of [62], [74] is adopted for the capacity computations in the 3-30MHz frequency range [25], [26], [30], [52], [75]; say -105 dBm/Hz is assumed to be the default AWGN PSD limit level $N(\cdot)$ for OV LV BPL networks; and (vii) *Best CASD with respect to its capacity estimation*: This is one of the main objective of the companion paper of [76] to be determined for the OV LV BPL networks. Anyway, in accordance with [36], [37], it has been demonstrated for the iSHM that Weibull and Wald CASDs perform the best capacity estimations in OV MV and UN MV power grid types, respectively, regardless of the examined BPL topology subclass when the respective default operation settings concerning IPSD limits, noise PSD levels and applied coupling scheme are assumed. Seventh, in accordance with [36], [37], the performance of iSHM and the accuracy of its capacity results significantly depend on the selection of the CASD. Based on the findings of [36] and [45], it has been demonstrated for the iSHM that Weibull and Gaussian CASDs perform the best capacity estimations in OV MV and OV HV BPL networks, respectively, regardless of the examined BPL topology subclass when the aforementioned default operation settings are adopted. Anyway, one of the main interest of the companion paper of [76] is the identification of the best CASD for the OV LV BPL networks with respect to the best capacity estimations when the default operation settings are applied.

As the default operation settings for mSHM are assumed, these operation settings remain the same with the iSHM ones when the only difference lies in the seventh category (*i.e.*, best CASD with respect to its capacity estimation). In contrast with iSHM, only one CASD, say, the Empirical CASD, is adopted by mSHM by default.

Finally, as the default operation settings of the definition procedures are concerned, these are further divided into two groups: (i) *iSHM definition procedure*

*default operation settings*: With respect to FL1.05 of Fig. 3(a), the number of spacings for the horizontal and vertical axis (*i.e.*, $no\_1$ and $no\_2$, respectively) is assumed to be equal to 10 in both cases. Note that the most suitable CASD with respect to its capacity estimation is going to be determined in [76] where the spacings for the horizontal and vertical axis are there applied; and (ii) *mSHM definition procedure default operation settings*: Since Empirical CASD is the only examined CASD, CDFs are of interest and not MLEs. With respect to FL2.05 of Fig. 3(b), the number of spacings for the horizontal and vertical axis (*i.e.*, $no\_3$ and $no\_4$, respectively) is assumed to be equal to 10 in both cases. Since CDF shifts are applied during the mSHM definition procedure, the maximum and minimum horizontal shift is assumed to be equal to 30 dB and -30 dB, respectively, while the maximum and minimum vertical shift is assumed to be equal to 1 and 0, respectively. Since the last step of both definition procedures (*i.e.*, FL1.11 or FL2.11) deals with the class mapping, the aforementioned iSHM and mSHM definition procedure default operation settings have significant impact on the appearance of the class maps.

## 4. TIM, FIIM and HS-DET method – The Basics and their Class Maps Footprints

Class maps define the graphical basis where the footprints of the three smart grid broadband applications of interest (*i.e.*, TIM, FIIM and HS-DET method) are going to be projected. In this Section, the three smart grid broadband applications are briefly outlined as well as the default operation settings that are required to be adopted. Note that numerical details concerning the default operation settings are also given in [76].

### 4.1 TIM

In accordance with [46], a BPL topology can be accurately identified with respect to its topological characteristics (*i.e.*, number of branches, length of branches, length of main distribution lines and branch terminations) when TIM is applied. In fact, TIM can recognize the BPL topology even if significant measurement differences may occur by appropriately approximating the measured coupling scheme channel transfer function data of the BPL topology, which are contaminated by measurement differences. To approximate measured coupling scheme channel transfer function data, TIM exploits the application of L1PMA, which is a piecewise monotonic data approximation [77], [78], to its TIM BPL topology database where real BPL topologies with their respective theoretical and measured coupling scheme channel transfer functions stand. Depending on the required examined scenario, corresponding TIM BPL topology database specifications are concerned for the database preparation; say, the maximum number of branches $N$, the length spacing $L_s$ for both branch distance and branch length and the maximum branch length $L_b$ for the OV LV BPL topologies.

In the companion paper, to illustrate the TIM footprint on the class maps of all possible real OV LV BPL topologies, the OV LV BPL topology database can be appropriately adjusted when the measurement differences are assumed to be equal to zero. For each real OV LV BPL topology of the TIM BPL topology database and with reference to its coupling scheme channel transfer function data, the following

corresponding records are inserted: (i) the MLEs of the supported CASDs as described in iSHM; (ii) the Empirical CDF as described in mSHM; and (iii) the capacity; when the default operation settings of Sec.3.4 are assumed.

With reference to Sec.3.3, each OV LV BPL topology of the TIM BPL topology database can be represented on the iSHM class map for given CASD by appropriately exploiting its respective CASD MLEs. Therefore, the TIM footprint on the iSHM class map consists of all TIM database OV LV BPL topology points, which are expected to create a subarea on the entire class map since class maps consist of all possible OV LV BPL topologies (*i.e.*, virtual OV LV BPL topologies) in terms of the corresponding CASD MLEs. As the capacity of each OV LV BPL topology of the TIM BPL topology database is concerned, its capacity remains very close to the average capacity of the OV LV BPL topology subclass whose virtual indicative OV LV BPL topology is characterized by the same CASD MLEs with the ones of real OV LV BPL topology of the TIM database when the examined CASD performs successful capacity estimation in terms of the percentage change metric [36], [37].

With reference to Sec.3.3, each OV LV BPL topology of the TIM BPL topology database cannot be directly represented on the mSHM class map for given real indicative OV LV BPL topology of the main subclasses but a capacity correlation should be first computed so that the best fit between the examined OV LV BPL topology of the TIM BPL topology database and one horizontally and vertically shifted version of the real indicative OV LV BPL topology (*i.e.*, virtual indicative OV LV BPL topologies) may occur. Strictly theoretically, with reference to eq. (3), the aforementioned best fit is achieved through the minimization of the following Frobenius distance with regards to the subchannel capacities, namely:

$$F = f_s \sqrt{\sum_{q=1}^{Q} \left( \log_2 \frac{\left\{1+\left[\frac{(P(f_q))_L}{(N(f_q))_L}\left|H_{\mathrm{TIM}}^{\mathrm{OVLV,C}}(f_q)\right|^2\right]\right\}}{\left\{1+\left[\frac{(P(f_q))_L}{(N(f_q))_L}\left|H'^{\,\mathrm{OVLV,C}}_{l(k\_no\_3,k\_no\_4),1}(f_q)\right|^2\right]\right\}} \right)^2} \cong f_s \sqrt{\sum_{q=1}^{Q} \left( \log_2 \frac{\left[\left|H_{\mathrm{TIM}}^{\mathrm{OVLV,C}}(f_q)\right|^2\right]}{\left[\left|H'^{\,\mathrm{OVLV,C}}_{l(k\_no\_3,k\_no\_4),1}(f_q)\right|^2\right]} \right)^2} \quad (7)$$

where $H_{\mathrm{TIM}}^{\mathrm{OVLV,C}}(f_q)$ is the $q$-th element of the $1\times Q$ coupling scheme channel transfer function line vector $\mathbf{H}_{\mathrm{TIM}}^{\mathrm{OVLV,C}}(\mathbf{f})$ of the examined OV LV BPL topology of the TIM BPL topology database and $H'^{\,\mathrm{OVLV,C}}_{l(k\ no\ 3,k\ no\ 4),1}(f_q)$ is the $q$-th element of the $1\times Q$ coupling scheme channel transfer function line vector $\mathbf{H}'^{\mathrm{OVLV,C}}_{l(k\_no\_3,k\_no\_4),1}(\mathbf{f})$ of the first virtual OV LV BPL topology of mSHM that corresponds to the $[k\_no\_3 \quad k\_no\_4]$ shift pair combination. The minimization of the Frobenius distance of eq.(7) implies that the capacity of the examined OV LV BPL topology of the TIM BPL topology database remains almost equal to the capacity of the shifted version of the real indicative OV LV BPL topology with $[k\_no\_3 \quad k\_no\_4]$ shift pair combination (say, best shifted version of the real indicative OV LV BPL topology). Practically, the best shifted version of the real indicative OV LV BPL topology can approximately be computed by comparing the capacity of the examined OV LV BPL topology of the TIM BPL topology database with all the capacities of the virtual OV LV BPL topologies and finding the corresponding $[k\_no\_3 \quad k\_no\_4]$ shift pair combination (*i.e.*, practical approximation of Frobenius distance). Thus, the examined OV LV BPL topology of the TIM BPL topology database can be indirectly characterized by the $[k\_no\_3 \quad k\_no\_4]$ shift pair combination of the best shifted version of the real indicative OV LV BPL topology and, hence, can be represented on the mSHM class map at the respective coordinates of the horizontal and vertical shifts. Similarly to the TIM footprint on the iSHM class map, the TIM footprint

on the mSHM class map consists of all TIM database OV LV BPL topology points, creating a subarea on the entire class map. Similarly to iSHM class maps, the capacity of the OV LV BPL topologies of the TIM BPL topology database remain very close to the average capacity of the OV LV BPL topology subclass whose virtual indicative OV LV BPL topology is characterized by an Empirical CDF that almost coincide with the one of real OV LV BPL topology of the TIM database when the Empirical CASD performs successful capacity estimation in terms of the percentage change metric [36], [37].

## 4.2 FIIM

In accordance with [46], FIIM achieves to identify any faults and instabilities that may occur in BPL topologies. FIIM repertory of faults and instabilities can be divided into two categories with two subcategories each, namely [79]: (i) *Faults*: This category describes all the interruptions that may occur across the lines of the power grid and can be further divided into two subcategories of line interruptions, say Fault in transmission line and Fault in branch line; and (ii) *Instabilities*: This category describes all the failures that can occur in the equipment across the power grid and can be further divided into two subcategories, say Instability in branch interconnections and Instability in branch terminations. Similarly to TIM, FIIM applies L1PMA to the measured coupling scheme transfer function data while FIIM supports its own FIIM BPL topology database where real BPL topologies that suffer from all the aforementioned faults and instabilities with their respective theoretical and measured coupling scheme channel transfer functions stand. In this paper, only the subcategory of one sole fault in one branch line is going to be examined. For given indicative OV LV BPL topology of Table 1, as the FIIM OV LV BPL topology database specifications are concerned for the database preparation, these remain the same with the TIM OV LV BPL topology database as described in Sec.4.1 while the fault location at the existing branch of the indicative OV LV BPL topology ranges from 0.1m to the end of the corresponding branch with a step of 0.1m. Note that the faulty branch termination is assumed to be open-circuit.

Similarly to the examined TIM iSHM and mSHM footprints of Sec.4.1, OV LV BPL topologies of the FIIM BPL topology database with one sole fault in one branch line can be represented on the iSHM class map for given CASD and indicative OV LV BPL topology of Table 1 by appropriately exploiting their respective CASD MLEs (FIIM iSHM footprint). As the FIIM mSHM footprint is concerned, by applying the practical approximation of Frobenius distance, virtual OV LV BPL topologies, which are characterized by respective $[k\_no\_3 \quad k\_no\_4]$ shift pair combinations, that approximate the behavior of the corresponding examined OV LV BPL topologies of the FIIM BPL topology database with one sole fault in one branch line can be identified (corresponding best fits). Hence, OV LV BPL topologies of the FIIM BPL topology database with one sole fault in one branch line can be represented on the mSHM class map at the coordinates of the horizontal and vertical shifts of their corresponding best fits (FIIM mSHM footprint).

## 4.3 HS-DET Method

In accordance with [47], HS-DET method achieves to identify any hook style energy theft in OV LV BPL networks either in theoretical or in real operation conditions; say with or without measurement differences, respectively. In [80], [81], the detection efficiency of HS-DET method has been exhaustively verified even in special operation cases of OV LV

BPL networks (*e.g.*, high measurement differences, very long hooks, "smart" hooks, feint "smart" hooks and hook interconnection issues). In contrast with TIM and FIIM, HS-DET method does not apply piecewise monotonic data approximations but adopts the metric of PES between the results collected by in-situ measurements and the theoretical results derived from DHM that occur during the normal operation of channel attenuation determination –see eqs.(3)-(8) of [47]–. Since the measurement differences are neglected during the determination of the coupling scheme channel transfer functions in this paper, PES is computed between the theoretical coupling scheme transfer functions of the real OV LV BPL topology of the TIM BPL topology database and the corresponding OV LV BPL topology that suffers from the hook style energy theft. Note that one sole hook is assumed during the energy theft from the real OV LV BPL topology but a plethora of different variations of the real OV LV BPL topology can be examined in terms of the hook distance from the transmitting end and the hook length. Hence, for given real OV LV BPL topology of the TIM BPL topology database, HS-DET method BPL topology database consists of all the possible corresponding real OV LV BPL topology with hook that can be assumed when the length spacing for both hook distance and hook length is assumed as well as the maximum hook length $L_b$. In accordance with [47], except for the aforementioned assumptions concerning the HS-DET method BPL topology database specifications, the hook termination is assumed to be open circuit while the hook interconnection with the distribution lines is assumed to be complete (*i.e.*, hook derivation points at the same distance from the transmitting end on all the three phases) and horizontal. Therefore, the hook can be treated by DHM as a branch. As already been verified in [80], [81], the previous assumptions are made in order to simplify the following analysis without losing its generality.

Similarly to the examined FIIM iSHM and mSHM footprints of Sec.4.2, OV LV BPL topologies of the HS-DET method BPL topology database with one sole hook can be represented on the iSHM class map for given CASD and real indicative OV LV BPL topology of Table 1, by appropriately exploiting their respective CASD MLEs (HS-DET method iSHM footprint). As the HS-DET method mSHM footprint is concerned, by applying the practical approximation of Frobenius distance, virtual OV LV BPL topologies, which are characterized by respective $[k\_no\_3 \quad k\_no\_4]$ shift pair combinations, that approximate the behavior of the corresponding examined OV LV BPL topologies of the HS-DET method BPL topology database with one sole hook can be identified (corresponding best fits). Hence, OV LV BPL topologies of the HS-DET method BPL topology database with one sole hook can be represented on the mSHM class map at the coordinates of the horizontal and vertical shifts of their corresponding best fits (HS-DET method mSHM footprint).

## 5. Conclusions

In this paper, a review concerning the interoperability of DHM, iSHM, mSHM, the definition procedure and the class maps has been first presented for OV LV BPL networks as well as the required default settings for their fine combined operation. However, the main interest of this paper has focused on the theory presentation of the OV LV BPL topology footprints of TIM, FIIM and HS-DET method on the class maps rather than on the numerical evaluation that is demonstrated in [76]. With respect to specific settings concerning the applied OV LV BPL topology databases of TIM, FIIM and HS-

DET method, the following footprint cases have been theoretically defined, namely: (i) iSHM and mSHM footprints of the real OV LV BPL topologies as described in TIM database; (ii) iSHM and mSHM footprints of OV LV BPL topologies of the FIIM BPL topology database with one sole fault in one branch line for given real indicative OV LV BPL topology; and (iii) iSHM and mSHM footprints of OV LV BPL topologies of the HS-DET method BPL topology database with one sole hook for given real indicative OV LV BPL topology. In [76], the numerical results concerning the first application of the combined operation of iSHM, mSHM, the definition procedure and the class maps on OV LV BPL topologies are demonstrated as well as the proposal of the aforementioned footprint cases.

## CONFLICTS OF INTEREST

The author declares that there is no conflict of interests regarding the publication of this paper.

## References

[1] M. H. Rehmani, M. Reisslein, A. Rachedi, M. Erol-Kantarci, and M. Radenkovic, "Integrating renewable energy resources into the smart grid: recent developments in information and communication technologies," *IEEE Transactions on Industrial Informatics*, vol. 14, no. 7, pp. 2814-2825, 2018.

[2] F. R. Yu, P. Zhang, W. Xiao, and P. Choudhury, "Communication systems for grid integration of renewable energy resources," *IEEE Network*, vol. 25, no. 5, pp. 22–29, Sep. 2011.

[3] B. Heile, "Smart grids for green communications [industry perspectives]," *IEEE Wireless Commun.*, vol. 17, no. 3, pp. 4–6, Jun. 2010.

[4] G. Artale, A. Cataliotti, V. Cosentino, D. Di Cara, R. Fiorelli, S. Guaiana, and G. Tinè, "A New Low Cost Coupling System for Power Line Communication on Medium Voltage Smart Grids," *IEEE Trans. on Smart Grid*, vol. 9, no. 4, pp. 3321-3329, 2018.

[5] L. González-Sotres, C. Mateo, P. Frías, C. Rodríguez-Morcillo, and J. Matanza, "Replicability Analysis of PLC PRIME Networks for Smart Metering Applications," *IEEE Trans. on Smart Grid*, vol. 9, no. 2, pp. 827-835, Mar. 2018.

[6] A. ElSamadouny, A. El Shafie, M. Abdallah, and N. Al-Dhahir, "Secure Sum-Rate-Optimal MIMO Multicasting Over Medium-Voltage NB-PLC Networks," *IEEE Trans. on Smart Grid*, vol. 9, no. 4, pp. 2954-2963, Jul. 2018.

[7] A. G. Lazaropoulos and P. G. Cottis, "Transmission characteristics of overhead medium voltage power line communication channels," *IEEE Trans. Power Del.*, vol. 24, no. 3, pp. 1164-1173, Jul. 2009.

[8] A. G. Lazaropoulos and P. G. Cottis, "Broadband transmission via underground medium-voltage power lines-Part I: transmission characteristics," *IEEE Trans. Power Del.*, vol. 25, no. 4, pp. 2414-2424, Oct. 2010.

[9] E. Biglieri, "Coding and modulation for a horrible channel," *IEEE Commun. Mag.*, vol. 41, no. 5, pp. 92–98, May 2003.
[10] M. Gebhardt, F. Weinmann, and K. Dostert, "Physical and regulatory constraints for communication over the power supply grid," *IEEE Commun. Mag.*, vol. 41, no. 5, pp. 84-90, May 2003.
[11] M. Götz, M. Rapp, and K. Dostert, "Power line channel characteristics and their effect on communication system design," *IEEE Commun. Mag.*, vol. 42, no. 4, pp. 78-86, Apr. 2004.
[12] A. G. Lazaropoulos, "Towards Modal Integration of Overhead and Underground Low-Voltage and Medium-Voltage Power Line Communication Channels in the Smart Grid Landscape: Model Expansion, Broadband Signal Transmission Characteristics, and Statistical Performance Metrics (Invited Paper)," *ISRN Signal Processing*, vol. 2012, Article ID 121628, pp. 1-17, 2012. [Online]. Available: http://www.hindawi.com/isrn/sp/2012/121628/
[13] K. Dostert, *Powerline Communications*. Upper Saddle River, NJ: Prentice-Hall, 2001.
[14] F. Versolatto and A. M. Tonello, "An MTL theory approach for the simulation of MIMO power-line communication channels," *IEEE Trans. Power Del.*, vol. 26, no. 3, pp. 1710-1717, Jul. 2011.
[15] P. Amirshahi and M. Kavehrad, "High-frequency characteristics of overhead multiconductor power lines for broadband communications," *IEEE J. Sel. Areas Commun.*, vol. 24, no. 7, pp. 1292-1303, Jul. 2006.
[16] T. Sartenaer, "Multiuser communications over frequency selective wired channels and applications to the powerline access network" *Ph.D. dissertation*, Univ. Catholique Louvain, Louvain-la-Neuve, Belgium, Sep. 2004.
[17] T. Sartenaer and P. Delogne, "Deterministic modelling of the (Shielded) outdoor powerline channel based on the multiconductor transmission line equations," *IEEE J. Sel. Areas Commun.*, vol. 24, no. 7, pp. 1277-1291, Jul. 2006.
[18] T. Calliacoudas and F. Issa, ""Multiconductor transmission lines and cables solver," An efficient simulation tool for plc channel networks development," presented at the *IEEE Int. Conf. Power Line Communications and Its Applications*, Athens, Greece, Mar. 2002.
[19] S. Galli and T. Banwell, "A deterministic frequency-domain model for the indoor power line transfer function," *IEEE J. Sel. Areas Commun.*, vol. 24, no. 7, pp. 1304-1316, Jul. 2006.
[20] S. Galli and T. Banwell, "A novel approach to accurate modeling of the indoor power line channel-Part II: Transfer function and channel properties," *IEEE Trans. Power Del.*, vol. 20, no. 3, pp. 1869-1878, Jul. 2005.
[21] A. Pérez, A. M. Sánchez, J. R. Regué, M. Ribó, R. Aquilué, P. Rodréguez-Cepeda, and F. J. Pajares, "Circuital and modal characterization of the power-line network in the PLC band," *IEEE Trans. Power Del.*, vol. 24, no. 3, pp. 1182-1189, Jul. 2009.
[22] H. Meng, S. Chen, Y. L. Guan, C. L. Law, P. L. So, E. Gunawan, and T. T. Lie, "Modeling of transfer characteristics for the broadband power line communication channel," *IEEE Trans. Power Del.*, vol. 19, no. 3, pp. 1057-1064, Jul. 2004.

[23] P. Amirshahi, "Broadband access and home networking through powerline networks" Ph.D. dissertation, Pennsylvania State Univ., University Park, PA, May 2006.

[24] A. G. Lazaropoulos, "Towards Broadband over Power Lines Systems Integration: Transmission Characteristics of Underground Low-Voltage Distribution Power Lines," *Progress in Electromagnetics Research B*, vol. 39, pp. 89-114, 2012. [Online]. Available: http://www.jpier.org/PIERB/pierb39/05.12012409.pdf

[25] A. G. Lazaropoulos and P. G. Cottis, "Capacity of overhead medium voltage power line communication channels," *IEEE Trans. Power Del.*, vol. 25, no. 2, pp. 723-733, Apr. 2010.

[26] A. G. Lazaropoulos and P. G. Cottis, "Broadband transmission via underground medium-voltage power lines-Part II: capacity," *IEEE Trans. Power Del.*, vol. 25, no. 4, pp. 2425-2434, Oct. 2010.

[27] A. G. Lazaropoulos, "Broadband transmission and statistical performance properties of overhead high-voltage transmission networks," *Hindawi Journal of Computer Networks and Commun.*, 2012, article ID 875632, 2012. [Online]. Available: http://www.hindawi.com/journals/jcnc/aip/875632/

[28] A. G. Lazaropoulos, "Wireless Sensor Network Design for Transmission Line Monitoring, Metering and Controlling Introducing Broadband over PowerLines-enhanced Network Model (BPLeNM)," *ISRN Power Engineering*, vol. 2014, Article ID 894628, 22 pages, 2014. doi:10.1155/2014/894628. [Online]. Available: http://www.hindawi.com/journals/isrn.power.engineering/2014/894628/

[29] A. G. Lazaropoulos, "Broadband Performance Metrics and Regression Approximations of the New Coupling Schemes for Distribution Broadband over Power Lines (BPL) Networks," *Trends in Renewable Energy*, vol. 4, no. 1, pp. 43-73, Jan. 2018. [Online]. Available: http://futureenergysp.com/index.php/tre/article/view/59/pdf

[30] A. G. Lazaropoulos, "Smart Energy and Spectral Efficiency (SE) of Distribution Broadband over Power Lines (BPL) Networks – Part 1: The Impact of Measurement Differences on SE Metrics," *Trends in Renewable Energy*, vol. 4, no. 2, pp. 125-184, Aug. 2018. [Online]. Available: http://futureenergysp.com/index.php/tre/article/view/76/pdf

[31] A. M. Tonello and T. Zheng, "Bottom-up transfer function generator for broadband PLC statistical channel modeling," In *Proc. IEEE International Symposium on Power Line Communications and Its Applications 2009, ISPLC 2009*, pp. 7-12, Mar. 2009.

[32] A. M. Tonello and F. Versolatto, "Bottom-up statistical PLC channel modeling—Part I: Random topology model and efficient transfer function computation," *IEEE Transactions on Power Delivery*, vol. 26, no. 2, pp. 891-898, 2011.

[33] A. Pittolo and A. M. Tonello, "A synthetic statistical mimo plc channel model applied to an in-home scenario," *IEEE Transactions on Communications*, vol. 65, no. 6, pp. 2543-2553, 2017.

[34] A. M. Tonello and F. Versolatto, "Bottom-up statistical PLC channel modeling—Part II: Inferring the statistics," *IEEE transactions on Power Delivery*, vol. 25, no. 4, pp. 2356-2363, 2010.

[35] A. G. Lazaropoulos, "Statistical Broadband over Power Lines Channel Modeling – Part 1: The Theory of the Statistical Hybrid Model," *Progress in Electromagnetics Research C*, vol. 92, pp. 1-16, 2019. [Online]. Available: http://www.jpier.org/PIERC/pierc92/01.19012902.pdf

[36] A. G. Lazaropoulos, "Statistical Broadband over Power Lines (BPL) Channel Modeling – Part 2: The Numerical Results of the Statistical Hybrid Model," *Progress in Electromagnetics Research C*, vol. 92, pp. 17-30, 2019. [Online]. Available: http://www.jpier.org/PIERC/pierc92/02.19012903.pdf

[37] A. G. Lazaropoulos, "Enhancing the Statistical Hybrid Model Performance in Overhead and Underground Medium Voltage Broadband over Power Lines Channels by Adopting Empirical Channel Attenuation Statistical Distribution," *Trends in Renewable Energy*, vol. 5, no. 2, pp. 181-217, 2019. [Online]. Available: http://futureenergysp.com/index.php/tre/article/view/96/pdf

[38] T. Oliveira, A. Picorone, C. Zeller, S. Netto, and M. Ribeiro, "Statistical Modeling of Brazilian In-Home PLC Channel Features," *Journal of Communication and Information Systems*, vol. 34, no. 1, pp. 154-168, 2019.

[39] T. R. Oliveira, C. B. Zeller, S. L. Netto, and M. V. Ribeiro, "Statistical modeling of the average channel gain and delay spread in in-home PLC channels," in *Proc. in IEEE International Symposium on Power Line Communications and Its Applications*, pp. 184-188, Mar. 2015.

[40] J. A. Cortes, F. J. Canete, L. Dıez, and J. L. G. Moreno, "On the statistical properties of indoor power line channels: Measurements and models," in *Proc. IEEE International Symposium on Power Line Communications and Its Applications*, pp. 271-276, Apr. 2011.

[41] A. M. Tonello, F. Versolatto, and A. Pittolo, "In-home power line communication channel: Statistical characterization," *IEEE Trans. on Commun.*, vol. 62, no. 6, pp. 2096–2106, Jun. 2014.

[42] S. Galli, "A novel approach to the statistical modeling of wireline channels," *IEEE Transactions on Commun.*, vol. 59, no. 5, pp. 1332–1345, May 2011.

[43] A. G. Lazaropoulos, "Virtual Indicative Broadband over Power Lines Topologies for Respective Subclasses by Adjusting Channel Attenuation Statistical Distribution Parameters of Statistical Hybrid Models – Part 1: Theory," *Trends in Renewable Energy*, vol. 5, no. 3, pp. 237-257, Aug. 2019. [Online]. Available: http://futureenergysp.com/index.php/tre/article/view/99/pdf

[44] A. G. Lazaropoulos, "Virtual Indicative Broadband over Power Lines Topologies for Respective Subclasses by Adjusting Channel Attenuation Statistical Distribution Parameters of Statistical Hybrid Models – Part 2: Numerical Results for the Overhead and Underground Medium-Voltage Power Grids," *Trends in Renewable Energy*, vol. 5, no. 3, pp. 258-281, Aug. 2019. [Online]. Available: http://futureenergysp.com/index.php/tre/article/view/100/pdf

[45] A. G. Lazaropoulos, "Virtual Indicative Broadband over Power Lines Topologies for Respective Subclasses by Adjusting Channel Attenuation Statistical Distribution Parameters of Statistical Hybrid Models – Part 3: The Case of Overhead Transmission Power Grids," *Trends in Renewable Energy*, vol. 5, no. 3, pp. 282-306, Aug. 2019. [Online]. Available: http://futureenergysp.com/index.php/tre/article/view/101/pdf

[46] A. G. Lazaropoulos, "Improvement of Power Systems Stability by Applying Topology Identification Methodology (TIM) and Fault and Instability Identification Methodology (FIIM)–Study of the Overhead Medium-Voltage Broadband over Power Lines (OV MV BPL) Networks Case," *Trends in Renewable Energy*, vol. 3, no. 2, pp. 102-128, Apr. 2017. [Online]. Available: http://futureenergysp.com/index.php/tre/article/view/34

[47] A. G. Lazaropoulos, "Detection of Energy Theft in Overhead Low-Voltage Power Grids – The Hook Style Energy Theft in the Smart Grid Era," *Trends in Renewable Energy*, vol. 5, no. 1, pp. 12-46, Oct. 2018. [Online]. Available: http://futureenergysp.com/index.php/tre/article/view/81/pdf

[48] OPERA1, D44: Report presenting the architecture of plc system, the electricity network topologies, the operating modes and the equipment over which PLC access system will be installed, IST Integr. Project No 507667, Dec. 2005.

[49] M. D'Amore and M. S. Sarto, "A new formulation of lossy ground return parameters for transient analysis of multiconductor dissipative lines," *IEEE Trans. Power Del.*, vol. 12, no. 1, pp. 303-314, Jan. 1997.

[50] M. D'Amore and M. S. Sarto, "Simulation models of a dissipative transmission line above a lossy ground for a wide-frequency range-Part I: Single conductor configuration," *IEEE Trans. Electromagn. Compat.*, vol. 38, no. 2, pp. 127-138, May 1996.

[51] M. D'Amore and M. S. Sarto, "Simulation models of a dissipative transmission line above a lossy ground for a wide-frequency range-Part II: Multi-conductor configuration," *IEEE Trans. Electromagn. Compat.*, vol. 38, no. 2, pp. 139-149, May 1996.

[52] A. G. Lazaropoulos, "Review and Progress towards the Capacity Boost of Overhead and Underground Medium-Voltage and Low-Voltage Broadband over Power Lines Networks: Cooperative Communications through Two- and Three-Hop Repeater Systems," *ISRN Electronics*, vol. 2013, Article ID 472190, pp. 1-19, 2013. [Online]. Available: http://www.hindawi.com/isrn/electronics/aip/472190/

[53] A. G. Lazaropoulos, "Broadband over Power Lines (BPL) Systems Convergence: Multiple-Input Multiple-Output (MIMO) Communications Analysis of Overhead and Underground Low-Voltage and Medium-Voltage BPL Networks (Invited Paper)," *ISRN Power Engineering*, vol. 2013, Article ID 517940, pp. 1-30, 2013. [Online]. Available: http://www.hindawi.com/isrn/power.engineering/2013/517940/

[54] A. G. Lazaropoulos, "Main Line Fault Localization Methodology (MLFLM) in Smart Grid–The Underground Medium- and Low-Voltage Broadband over Power Lines Networks Case," *Trends in Renewable Energy*, vol. 4, no. 1, pp. 15-42, Dec. 2017. [Online]. Available: http://futureenergysp.com/index.php/tre/article/view/45

[55] A. G. Lazaropoulos, "Underground Distribution BPL Connections with (N + 1)-hop Repeater Systems: A Novel Capacity Mitigation Technique," *Elsevier Computers and Electrical Engineering*, vol. 40, pp. 1813-1826, 2014.

[56] A. G. Lazaropoulos, "Deployment Concepts for Overhead High Voltage Broadband over Power Lines Connections with Two-Hop Repeater System:

Capacity Countermeasures against Aggravated Topologies and High Noise Environments," *Progress in Electromagnetics Research B*, vol. 44, pp. 283-307, 2012. [Online]. Available: http://www.jpier.org/PIERB/pierb44/13.12081104.pdf

[57] C. R. Paul, *Analysis of Multiconductor Transmission Lines*. New York: Wiley, 1994.

[58] J. A. B. Faria, *Multiconductor Transmission-Line Structures: Modal Analysis Techniques*. New York: Wiley, 1994.

[59] A. G. Lazaropoulos, "New Coupling Schemes for Distribution Broadband over Power Lines (BPL) Networks," *Progress in Electromagnetics Research B*, vol. 71, pp. 39-54, 2016. [Online]. Available: http://www.jpier.org/PIERB/pierb71/02.16081503.pdf

[60] NTIA, "Potential interference from broadband over power line (BPL) systems to federal government radio communications at 1.7-80 MHz Phase 1 Study Vol. 1," NTIA Rep. 04-413, Apr. 2004.

[61] NATO, "HF Interference, Procedures and Tools (Interférences HF, procédures et outils) Final Report of NATO RTO Information Systems Technology," RTO-TR-ISTR-050, Jun. 2007.

[62] A. G. Lazaropoulos, "The Impact of Noise Models on Capacity Performance of Distribution Broadband over Power Lines Networks," *Hindawi Computer Networks and Communications*, vol. 2016, Article ID 5680850, 14 pages, 2016. doi:10.1155/2016/5680850. [Online]. Available: http://www.hindawi.com/journals/jcnc/2016/5680850/

[63] N. Suljanović, A. Mujčić, M. Zajc, and J. F. Tasič, "Approximate computation of high-frequency characteristics for power line with horizontal disposition and middle-phase to ground coupling," *Elsevier Electr. Power Syst. Res.*, vol. 69, pp. 17-24, Jan. 2004.

[64] OPERA1, D5: Pathloss as a function of frequency, distance and network topology for various LV and MV European powerline networks. IST Integrated Project No 507667, Apr. 2005.

[65] N. Suljanović, A. Mujčić, M. Zajc, and J. F. Tasič, "High-frequency characteristics of high-voltage power line," in *Proc. IEEE Int. Conf. on Computer as a Tool*, Ljubljana, Slovenia, Sep. 2003, pp. 310-314.

[66] N. Suljanović, A. Mujčić, M. Zajc, and J. F. Tasič, "Power-line high-frequency characteristics: analytical formulation," in *Proc. Joint 1st Workshop on Mobile Future & Symposium on Trends in Communications*, Bratislava, Slovakia, Oct. 2003, pp. 106-109.

[67] W. Villiers, J. H. Cloete, and R. Herman, "The feasibility of ampacity control on HV transmission lines using the PLC system," in *Proc. IEEE Conf. Africon*, George, South Africa, Oct. 2002, vol. 2, pp. 865-870.

[68] J. Anatory, N. Theethayi, R. Thottappillil, M. M. Kissaka, and N. H. Mvungi, "The influence of load impedance, line length, and branches on underground cable Power-Line Communications (PLC) systems," *IEEE Trans. Power Del.*, vol. 23, no. 1, pp. 180-187, Jan. 2008.

[69] J. Anatory, N. Theethayi, and R. Thottappillil, "Power-line communication channel model for interconnected networks-Part II: Multiconductor system," *IEEE Trans. Power Del.*, vol. 24, no. 1, pp. 124-128, Jan. 2009.

[70] J. Anatory, N. Theethayi, R. Thottappillil, M. M. Kissaka, and N. H. Mvungi, "The effects of load impedance, line length, and branches in typical low-voltage channels of the BPLC systems of developing countries: transmission-line analyses," *IEEE Trans. Power Del.*, vol. 24, no. 2, pp. 621-629, Apr. 2009.

[71] T. Banwell and S. Galli, "A novel approach to accurate modeling of the indoor power line channel—Part I: Circuit analysis and companion model," *IEEE Trans. Power Del.*, vol. 20, no. 2, pp. 655-663, Apr. 2005.

[72] W. Villiers, J. H. Cloete, L. M. Wedepohl, and A. Burger, "Real-time sag monitoring system for high-voltage overhead transmission lines based on power-line carrier signal behavior," *IEEE Trans. Power Del.*, vol. 23, no. 1, pp. 389-395, Jan. 2008.

[73] A. G. Lazaropoulos, "A Panacea to Inherent BPL Technology Deficiencies by Deploying Broadband over Power Lines (BPL) Connections with Multi-Hop Repeater Systems," *Bentham Recent Advances in Electrical & Electronic Engineering*, vol. 10, no. 1, pp. 30-46, 2017

[74] A. G. Lazaropoulos, "Capacity Performance of Overhead Transmission Multiple-Input Multiple-Output Broadband over Power Lines Networks: The Insidious Effect of Noise and the Role of Noise Models (Invited Paper)," *Trends in Renewable Energy*, vol. 2, no. 2, pp. 61-82, Jun. 2016. [Online]. Available: http://futureenergysp.com/index.php/tre/article/view/23

[75] A. G. Lazaropoulos, "Smart Energy and Spectral Efficiency (SE) of Distribution Broadband over Power Lines (BPL) Networks – Part 2: L1PMA, L2WPMA and L2CXCV for SE against Measurement Differences in Overhead Medium-Voltage BPL Networks," *Trends in Renewable Energy*, vol. 4, no. 2, pp. 185-212, Aug. 2018. [Online]. Available: http://futureenergysp.com/index.php/tre/article/view/77/pdf

[76] A. G. Lazaropoulos, "Statistical Channel Modeling of Overhead Low Voltage Broadband over Power Lines (OV LV BPL) Networks – Part 2: The Numerical Results of Class Map Footprints of Real OV LV BPL Topologies, Branch Line Faults and Hook Style Energy Thefts," *Trends in Renewable Energy*, vol. 6, no. 1, pp. 88-109.

[77] I. C. Demetriou, "An application of best *L*1 piecewise monotonic data approximation to signal restoration," *IAENG International Journal of Applied Mathematics*, vol. 53, no. 4, pp. 226-232, 2013.

[78] I. C. Demetriou, "L1PMA: A Fortran 77 Package for Best L1 Piecewise Monotonic Data Smoothing," *Computer Physics Communications*, vol. 151, no. 1, pp. 315-338, 2003.

[79] A. G. Lazaropoulos, "Measurement Differences, Faults and Instabilities in Intelligent Energy Systems – Part 2: Fault and Instability Prediction in Overhead High-Voltage Broadband over Power Lines Networks by Applying Fault and Instability Identification Methodology (FIIM)," *Trends in Renewable Energy*, vol. 2, no. 3, pp. 113-142, Oct. 2016. [Online]. Available: http://futureenergysp.com/index.php/tre/article/view/27/33

[80] A. G. Lazaropoulos, "Special Cases during the Detection of the Hook Style Energy Theft in Overhead Low-Voltage Power Grids through HS-DET Method – Part 1: High Measurement Differences, Very Long Hook Technique and "Smart" Hooks,"

*Trends in Renewable Energy*, vol. 5, no. 1, pp. 60-89, Jan. 2019. [Online]. Available: http://futureenergysp.com/index.php/tre/article/view/82/pdf

[81] A. G. Lazaropoulos, "Special Cases during the Detection of the Hook Style Energy Theft in Overhead Low-Voltage Power Grids through HS-DET Method – Part 2: Different Measurement Differences, Feint "Smart" Hooks and Hook Interconnection Issues," *Trends in Renewable Energy*, vol. 5, no. 1, pp. 90-116, Jan. 2019. [Online]. Available: http://futureenergysp.com/index.php/tre/article/view/83/pdf



Trends in Renewable Energy
OPEN ACCESS ISSN: 2376-2144
Peer-Reviewed Article futureenergysp.com/index.php/tre

# Statistical Channel Modeling of Overhead Low Voltage Broadband over Power Lines (OV LV BPL) Networks – Part 2: The Numerical Results of Class Map Footprints of Real OV LV BPL Topologies, Branch Line Faults and Hook Style Energy Thefts

Athanasios G. Lazaropoulos*

*School of Electrical and Computer Engineering / National Technical University of Athens / 9 Iroon Polytechniou Street / Zografou, GR 15780*

Received January 22, 2020; Accepted February 26, 2020; Published March 12, 2020

In [1], the theoretical framework for the interoperability of DHM, iSHM, mSHM, the definition procedure and the class maps has been first presented for OV LV BPL networks. But the main interest of the first paper has focused on the theory of the OV LV BPL topology footprints of TIM, FIIM and HS-DET method on the class maps.
In this paper, the numerical results concerning the application of iSHM, mSHM, the definition procedure and the class maps to OV LV BPL networks are first shown. Then, given the iSHM and mSHM class maps, the footprints of TIM, FIIM and HS-DET method databases for the OV LV BPL topologies are highlighted. Finally, a technique for the detection of branch line faults and hook style energy thefts that is based on iSHM and mSHM footprints is proposed.

*Keywords: Smart Grid; Broadband over Power Lines (BPL) networks; Power Line Communications (PLC); Distribution and Transmission Power Grids; Capacity; Statistics; Modeling*

**Corresponding author:* AGLazaropoulos@gmail.com

Tr Ren Energy, 2020, Vol.6, No.1, 88-109. doi: 10.17737/tre.2020.6.1.00113

## Nomenclature

| | |
|---|---|
| AAAC | All Aluminum Alloy Conductor |
| AWGN | Additive White Gaussian Noise |
| BPL | Broadband over Power Lines |
| BPMN | Business Process Model and Notation |
| CASD | Channel Attenuation Statistical Distribution |
| CDF | cumulative density function |
| CS2 module | Coupling Scheme version 2 module |
| DHM | deterministic hybrid model |
| EMI | ElectroMagnetic Interference |
| FIIM | Fault and Instability Identification Methodology |
| FL noise model | Flat noise model |
| HS-DET method | hook style energy theft detection method |
| HV | High Voltage |
| ICT | Information and Communication Technology |
| IPSD limits | injected power spectral density limits |
| IP | Internet Protocol |
| iSHM | initial Statistical Hybrid Model |
| LOS | Line-of-Sight |
| LV | Low Voltage |
| L1PMA | L1 Piecewise Monotonic Approximation |
| MLE | Maximum Likelihood Estimator |
| mSHM | modified Statistical Hybrid Model |
| MTL | multiconductor transmission line |
| MtM | MultiWire-to-MultiWire |
| MV | Medium Voltage |
| OV | Overhead |
| PES | Percent Error Sum |
| PSD | Power spectral density |
| SG | Smart Grid |
| SHM | Statistical Hybrid Model |
| TIM | Topology Identification Methodology |
| TL | Transmission Line |
| TM2 method | Transmission Matrix version 2 method |
| UN | Underground |
| WtG | Wire-to-Ground |
| WtW | Wire-to-Wire |

## 1. Introduction

In SG applications, ICT is their key aspect while among the available ICT solutions, BPL technology presents some natural advantages that render the related BPL networks as the most suitable implementation for SG applications [2]. However, BPL networks operate across a hostile medium for communications since transmission and distribution power grid infrastructure and equipment have been designed to deliver power rather than information [1], [3]-[7].

The interaction results of the deterministic framework, which is represented by the DHM [3], [4], [8]-[13], and the recently proposed statistical framework, which is characterized by the SHM operation [14]-[19], for the OV LV BPL networks are presented in this paper with respect to the class maps and the footprint area concept that have been first presented for OV LV BPL networks in [1]. In detail, the numerical results of the application of iSHM and mSHM are presented while the performance of different CASDs among the available ones of iSHM and mSHM is here assessed. Actually, the most successful CASD among the available ones of iSHM is going to be identified with respect to the metrics of percentage change and the average absolute percentage change as the most successful CASD of mSHM is the Empirical one. Then, the definition procedure is going to be applied in OV LV BPL networks enriching the corresponding topology classes with topology subclasses whose respective virtual indicative OV LV BPL topologies are statistically defined in terms of the applied SHM version and its corresponding successful CASD parameters (*i.e.*, MLEs and CDF for iSHM and mSHM CASDs, respectively). On the basis of the most successful CASDs of iSHM and mSHM, the definition procedure gives as output the class maps of OV LV BPL networks that illustrate the borders between the BPL topology classes and also corresponds each CASD parameter pair to its BPL topology subclass average capacity for given power grid type, SHM version, CASD, coupling scheme, IPSD limits and noise levels [1]. By taking into account OV LV BPL topologies, the numerical results concerning the footprints on the class maps, which have been theoretically defined in [1] and may allow the impact investigation of critical events of the operation of OV LV power grids, are here presented, namely: (i) The footprint of the real OV LV BPL topologies is going to first be illustrated on the class maps thus separating the real OV LV BPL topologies from the virtual ones of class maps by exploiting the TIM database [20]; (ii) for given real indicative OV LV BPL topology, the footprint of all the corresponding OV LV BPL topologies with a sole branch line fault is going to be shown on class maps by exploiting the FIIM database [20]; and (iii) for given real indicative OV LV BPL topology, the footprint of all the corresponding OV LV BPL topologies with a single hook for energy theft are going to be demonstrated on class maps by exploiting the HS-DET method [21]. On the basis of the impact investigation of the aforementioned three critical events, the study of iSHM and mSHM footprints can also act as a useful supplementary technique for identifying branch line faults and hook style energy thefts.

The rest of this paper is organized as follows: In Section II, the numerical results concerning the interoperability of DHM, iSHM, mSHM, the definition procedure and the class maps of OV LV BPL networks are demonstrated. The footprints of the aforementioned three critical events during the operation of the OV LV BPL networks are illustrated on the class maps. Apart from the presentation, interesting comparisons

with OV MV and OV HV BPL networks are provided while the proposed technique for identifying branch line faults and hook style energy thefts through iSHM and mSHM footprints is provided.

## 2. Numerical Results and Discussion

In this Section, numerical results concerning the statistical behavior of OV LV BPL networks are categorized into the following subsections, namely: (i) *iSHM*: CASD MLEs of iSHM are reported while the performance of iSHM CASDs is assessed in terms of the best percentage change and average percentage change results. The best CASD of iSHM is found with respect to the aforementioned two performance metrics; (ii) *mSHM*: The performance of Empirical CASD is assessed; (iii) *Definition procedure and class maps*: The definition procedures for the best CASD of iSHM and the Empirical CASD of mSHM are applied while the corresponding class maps are illustrated; and (iv) *Footprints*: the footprints of the three OV LV BPL topology databases (*i.e.*, TIM, FIIM and HS-DET method databases) are shown on the iSHM and mSHM class maps.

### 2.1 CASD MLEs of iSHM for the OV LV BPL Networks

In accordance with the iSHM definition [14], [15], the BPMN diagram of iSHM, which describes its operation, is given in Fig. 2(a) of [1]. As the CASD MLEs of iSHM are concerned, these are computed at the MLE computation module of Phase C of the iSHM BPMN diagram thus affecting all the remaining iSHM operation. As already been recognized in [15], [16], the efficiency of the CASDs is based on the respective CASD MLEs that further depend on the capacity estimation of the real indicative BPL topologies that is extended to the case of OV LV BPL networks of this paper.

As the default operation settings have been assumed in [1], MLEs of the Gaussian, Lognormal, Wald, Weibull and Gumbel CASDs of iSHM are reported in Table 1 for the real indicative OV LV BPL topologies of the main subclasses of Table 1 of [1]. Similarly to [15], [16], [18], [19], the graphical analysis concerning the capacity estimation performance of CASDs of iSHM can be securely neglected by simply applying capacity estimation performance metrics such as the percentage change and the average absolute percentage change instead. Indeed, the percentage change and the average absolute percentage change of each iSHM CASD are reported in Table 2 per each indicative OV LV BPL topology main subclass as well as the capacity of each real indicative OV LV BPL topology of main subclasses.

By comparing iSHM CASD MLEs of the real indicative OV LV BPL topologies, which are presented in Table 1, with the respective ones of the real indicative OV MV BPL topologies of Table 1 of [15] and the respective ones of the real indicative OV HV BPL topologies of Table 2 of [19], iSHM CASD MLEs of the real indicative OV LV BPL topologies present more similar behavior to the iSHM CASD MLEs of the real indicative OV MV BPL topologies rather than the ones of the OV HV BPL topologies. This is due to the fact that: (i) the OV LV MTL configuration can be considered as a vertical rearrangement of the OV MV MTL configuration; and (ii) the average transmission path of OV LV BPL topologies has been assumed to be the same to the one of OV MV BPL topologies as well as the topological characteristics. Taking into account

the findings of [15], same observations concerning the iSHM CASD MLEs of the indicative OV LV BPL topologies with the ones of OV MV BPL topologies can be expressed, namely: (a) $\hat{\mu}_{MLE}^{Gaussian}$, $\hat{\mu}_{MLE}^{Lognormal}$, $\hat{\mu}_{MLE}^{Wald}$, $\hat{a}_{MLE}^{Weibull}$, $\hat{a}_{MLE}^{Gumbel}$, $\hat{\sigma}_{MLE}^{Gaussian}$, $\hat{\lambda}_{MLE}^{Wald}$

**Table 1**
iSHM CASD MLEs of Real Indicative OV LV BPL Topologies of Table 1 of [1] for the Default Operation Settings

| Topology Name | BPL Topology Class Description | Gaussian MLEs | | Lognormal MLEs | | Wald MLEs | | Weibull MLEs | | Gumbel MLEs | |
|---|---|---|---|---|---|---|---|---|---|---|---|
| | | $\hat{\mu}_{MLE}^{Gaussian}$ | $\hat{\sigma}_{MLE}^{Gaussian}$ | $\hat{\mu}_{MLE}^{Lognormal}$ | $\hat{\sigma}_{MLE}^{Lognormal}$ | $\hat{\mu}_{MLE}^{Wald}$ | $\hat{\lambda}_{MLE}^{Wald}$ | $\hat{a}_{MLE}^{Weibull}$ | $\hat{\beta}_{MLE}^{Weibull}$ | $\hat{a}_{MLE}^{Gumbel}$ | $\hat{\epsilon}_{MLE}^{Gumbel}$ |
| Urban case A | Typical OV MV BPL urban topology class | 12.77 | 11.70 | 2.08 | 1.06 | 12.77 | 6.5 | 13.29 | 1.11 | 19.27 | 14.98 |
| Urban case B | Aggravated OV MV BPL urban topology class | 17.80 | 13.53 | 2.51 | 0.99 | 17.80 | 9.3 | 19.28 | 1.31 | 25.24 | 17.36 |
| Suburban case | OV MV BPL suburban topology class | 7.50 | 9.85 | 1.20 | 1.45 | 7.50 | 1.1 | 6.62 | 0.81 | 13.41 | 15.93 |
| Rural case | OV MV BPL rural topology class | 2.92 | 2.93 | 0.42 | 1.22<br>2.94 | 2.92 | 1.1<br>$9.03\times10^{-10}$ | 2.80 | 0.92 | 4.48 | 3.10 |
| "LOS" case | OV MV BPL "LOS" transmission class | $1\times10^{-11}$ | 0 | -25.33 | $4\times10^{-15}$ | $1\times10^{-11}$ | $2.62\times10^{3}$ | $1\times10^{-11}$ | $\infty$ | $1\times10^{-11}$ | 0 |

**Table 2**
Percentage Change between the Average Capacity of the OV LV BPL Topology Classes and the Capacity of the Indicative Topology of the Respective Classes for the Five Examined CASDs of iSHM when the Default Operation Settings are assumed
(grey background: best results, black background: unsuccessful capacity estimation)

| Indicative OV LV BPL Topology Name (OV LV Capacity in Mbps) | BPL Topology Class Description | Percentage Change (%) | | | | |
|---|---|---|---|---|---|---|
| | | iSHM | | | | |
| | | Gaussian | Lognormal | Wald | Weibull | Gumbel |
| Urban case A (275) | Typical BPL urban class | -3.43 | 0.86 | 4.12 | 0.008 | -6.29 |
| Urban case B (234) | Aggravated BPL urban | -3.88 | 1.72 | 9.90 | 0.068 | -5.58 |
| Suburban case (322) | BPL suburban class | -4.21 | -0.93 | 3.70 | -0.11 | -8.72 |
| Rural case (361) | BPL rural class | -0.63 | -0.54 | 0.02 | -0.01 | -1.17 |
| **Average Absolute Percentage Change (%)** | | **3.04** | **1.01** | **4.43** | **0.05** | **5.44** |

and $\hat{\epsilon}_{\mathbf{MLE}}^{\mathbf{Gumbel}}$ of OV LV BPL topologies increase as the multipath environment of the OV LV BPL topologies becomes more intense; and (b) $\hat{\sigma}_{\mathbf{MLE}}^{\mathbf{Lognormal}}$ and $\hat{\beta}_{\mathbf{MLE}}^{\mathbf{Weibull}}$ of OV LV BPL topologies receive very close values among them that anyway may act as an identity value of the power grid type (*i.e.*, in this case OV LV) rather than OV LV BPL topology identifier.

In accordance with [16], [15], [18], [19], it has been proven that the capacity performance success can be assessed by applying the metrics of capacity, capacity percentage change and average absolute capacity percentage change, as reported in Table 2. More specifically:

- iSHM CASD capacity estimation performance for OV LV BPL subclasses presents similarities with the one of OV MV BPL subclasses rather than the one of OV HV BPL subclasses. Since OV distribution BPL topologies are mainly characterized by the significant lower 1km long transmission paths in comparison with the 25km long transmission paths of OV HV BPL topologies, which implies a weaker "LOS" attenuation mechanism, and by the multipath aggravation due to the frequent and relatively short branches of distribution power grids, it is evident that a CASD separation may occur on the basis of the examined power grid level.
- Similarly to OV MV BPL topology subclasses, Weibull CASD succeeds in satisfying the 3% absolute threshold of percentage change and average absolute percentage change in all the OV LV BPL topology subclasses examined. Actually, Weibull CASD achieves the best percentage change and average absolute percentage change in all the cases examined (see grey background in the column of Weibull CASD in Table 2). Note that the only CASD that can produce successful capacity estimations but with significantly worse performance in comparison with the one of Weibull CASD, especially in the cases of urban environments, is Lognormal CASD. In contrast with the Gaussian CASD that operates as the best CASD in OV HV BPL networks, Gaussian, Wald and Gumbel cannot successfully operate in OV LV BPL topologies apart from the rural case that anyway resembles to the OV HV BPL signal transmission in terms of the scarce presence of branches. Here, it should be also reminded that the best fit for UN MV BPL networks is Wald CASD as outlined in [15].

In the rest of this paper, only Weibull CASD is going to be considered as the best fit CASD among the available ones of iSHM and to be applied during the following subsections of the definition procedure, class mapping and footprints.

## 2.2 CASD of mSHM for the OV LV BPL Networks

The BPMN diagram of mSHM is illustrated in Fig. 2(b) of [1]. In contrast with iSHM and its supported CASD MLEs, mSHM exploits the Empirical CASD through the Empirical CDF, which acts as the CASD parameter, of the coupling scheme channel attenuation difference for given OV LV BPL topology and coupling scheme. As already been recognized in [16], [18], [19], the efficiency of the mSHM CASD is based on the Empirical CDFs while it depends on the capacity estimation of the real indicative BPL topologies.

As the default operation settings have been assumed in [1] for the computation of the Empirical CDFs of mSHM and similarly to iSHM, the graphical analysis concerning

the capacity estimation performance of Empirical CASD of mSHM can be securely

**Table 3**
Percentage Change between the Average Capacity of the OV LV BPL Topology Class and the Capacity of the Indicative Topology of the Respective Class for the Empirical CASD of mSHM when the Default Operation Settings are assumed
(grey background: best results, black background: unsuccessful capacity estimation)

| **Indicative OV LV BPL Topology Name (OV LV Capacity in Mbps)** | **BPL Topology Class Description** | **Percentage Change (%)** |
|---|---|---|
| | | **mSHM** |
| | | **Empirical** |
| Urban case A (275) | Typical BPL urban class | 0.14 |
| Urban case B (234) | Aggravated BPL urban | 0.19 |
| Suburban case (322) | BPL suburban class | 0.09 |
| Rural case (361) | BPL rural class | 0.03 |
| **Average Absolute Percentage Change (%)** | | **0.11** |

neglected while the aforementioned capacity estimation performance metrics are applied instead. Indeed, the percentage change and the average absolute percentage change of mSHM Empirical CASD are reported in Table 3 per each indicative OV LV BPL topology main subclass as well as the capacity of each real indicative OV LV BPL topology of main subclasses, which anyway coincides with the respective one of Table 2.

By comparing the results of Table 3 and 2, it is evident that Empirical CASD of mSHM presents a capacity performance success for the main OV LV BPL subclasses (grey background of the last column of Table 3) that can be considered to be comparable with the one of Weibull CASD of iSHM, which anyway demonstrates the best fit results. In all the main OV LV BPL subclasses examined, Empirical CASD succeeds in satisfying the 3% absolute threshold of percentage change and average absolute percentage change. As been mentioned in Sec.2.1, this is an expected result since capacity estimation performance for OV LV BPL subclasses presents more similarities with the one of OV MV BPL subclasses rather than the one of OV HV BPL subclasses. Therefore, apart from the Weibull CASD of iSHM, the Empirical CASD of mSHM is also going to be applied during the following subsections of the definition procedure, class mapping and footprints.

## 2.3 iSHM and mSHM Class Mapping for OV LV BPL Classes for the Default Operation Settings

Already been presented in [1], iSHM and mSHM definition procedures for OV LV BPL topologies are here applied for the class mapping. From Sec.2.2, Weibull CASD of iSHM and Empirical CASD of mSHM are considered to execute the most successful

capacity estimations for OV LV BPL topologies and for that reason the corresponding class maps are illustrated in this paper.

As the iSHM class map scenario is concerned, there are 5 pairs of $\hat{a}_{\mathbf{MLE}}^{\mathbf{Weibull}}$ and $\hat{\beta}_{\mathbf{MLE}}^{\mathbf{Weibull}}$ that are the Weibull CASD MLEs, for the respective real indicative OV LV BPL topologies of the main subclasses of Table 1 of [1]. The iSHM class map of OV LV BPL topologies is plotted in Fig. 1 with respect to $\hat{a}_{\mathbf{MLE}}^{\mathbf{Weibull}}$ and $\hat{\beta}_{\mathbf{MLE}}^{\mathbf{Weibull}}$ for the default operation settings of [1] when the average capacity of each OV LV BPL topology subclass is considered. Note that as the spacings of the horizontal axis, the spacings of the vertical axis and the capacity borders between the adjacent distribution BPL topology classes are concerned, their computation is in accordance with [18], [19].

As the mSHM class map scenario is concerned, in accordance with [17]-[19], the examined real indicative OV LV BPL topologies of the main subclasses are examined separately during the preparation of mSHM class maps. Among the five real indicative OV LV BPL topologies of the main subclasses of Table 1 of [1], three of them are of interest in this paper and are going to be investigated through mSHM class maps; say, OV LV BPL urban case A, suburban case and rural case. With reference to [1], the mSHM class map of OV LV BPL topologies is plotted in Fig. 2(a) with respect to the indicative OV LV BPL urban case A, horizontal shift $h\_shift$ and vertical shift $v\_shift$ for the default operation settings when the average capacity of each OV LV BPL topology subclass is assumed. In the same 2D contour plot, the capacity borders between the adjacent distribution BPL topology classes and the capacity of the reference indicative OV LV BPL urban case A are also shown. In Figs. 2(b) and 2(c), same plots with Fig. 2(a) are shown but for the case of the OV LV BPL suburban case and of the OV LV BPL rural case, respectively.

By observing Fig. 1 and Figs. 2(a)-(c) and by comparing them with the respective ones of [18] and [19], it is evident that iSHM and mSHM class maps of OV LV BPL topologies present more similarities with the respective ones of OV MV BPL topologies rather than of UN MV BPL topologies and of OV HV BPL topologies. Apart from the approximate same capacity border values between the adjacent distribution BPL topology classes, the pattern of iSHM class maps present the same class area notches when the distribution BPL topologies are examined in contrast with the rectangular class areas of UN MV BPL topologies and OV HV BPL topologies. Also, as the mSHM class maps are regarded, the extent and the capacity border continuity of the "LOS" class area –*i.e.*, yellow class area in Figs. 2(a)-(c)– remain very similar between the OV MV BPL topologies and OV LV BPL ones.

Anyway, it should be noted that common issues among all the iSHM and mSHM class maps of transmission and distribution BPL topologies stand that are: (i) the clear distinction between the adjacent BPL topology classes regardless of the type of the examined class map; and (ii) the same general pattern of mSHM class maps where a large "LOS" class area exists at the left of the mSHM class map and two separate aggravated urban case class areas lie at the top and bottom right of the mSHM class map.

On the basis of Fig. 1 and Figs. 2(a)-(c), the footprints of the three OV LV BPL topology databases (*i.e.*, TIM, FIIM and HS-DET method databases), which are going to be studied in Secs. 2.4-2.6, respectively, are graphically superimposed on the aforementioned iSHM and mSHM class maps.

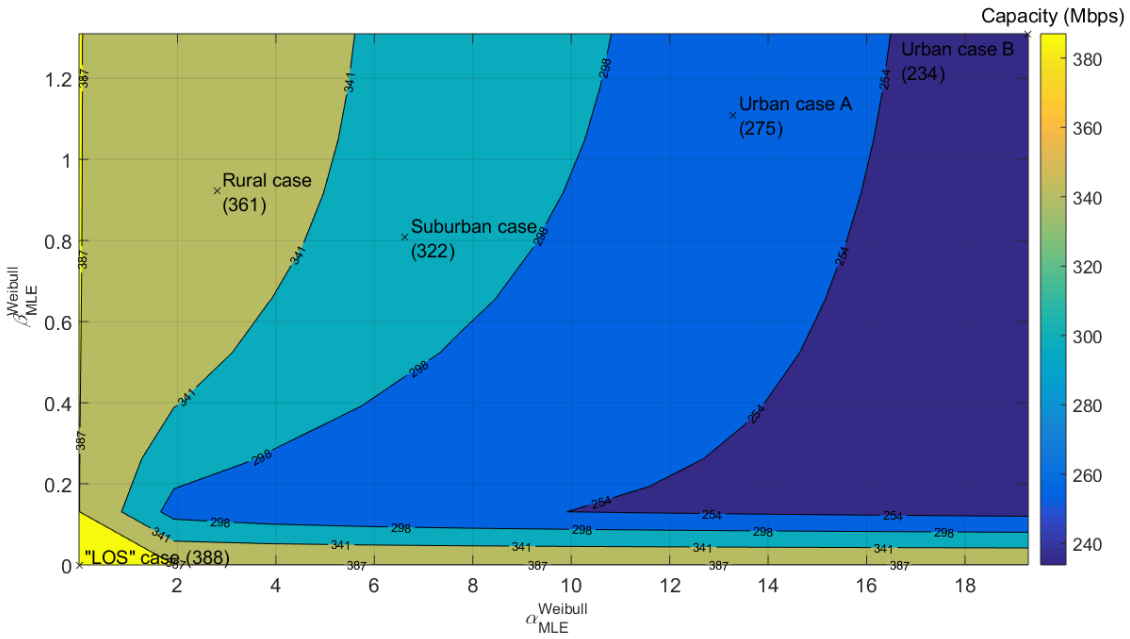


**Fig. 1**. iSHM class map for the average capacity of the OV LV BPL topologies in the 3-30MHz frequency band when WtG[1] coupling scheme is deployed and FCC Part 15 is applied.

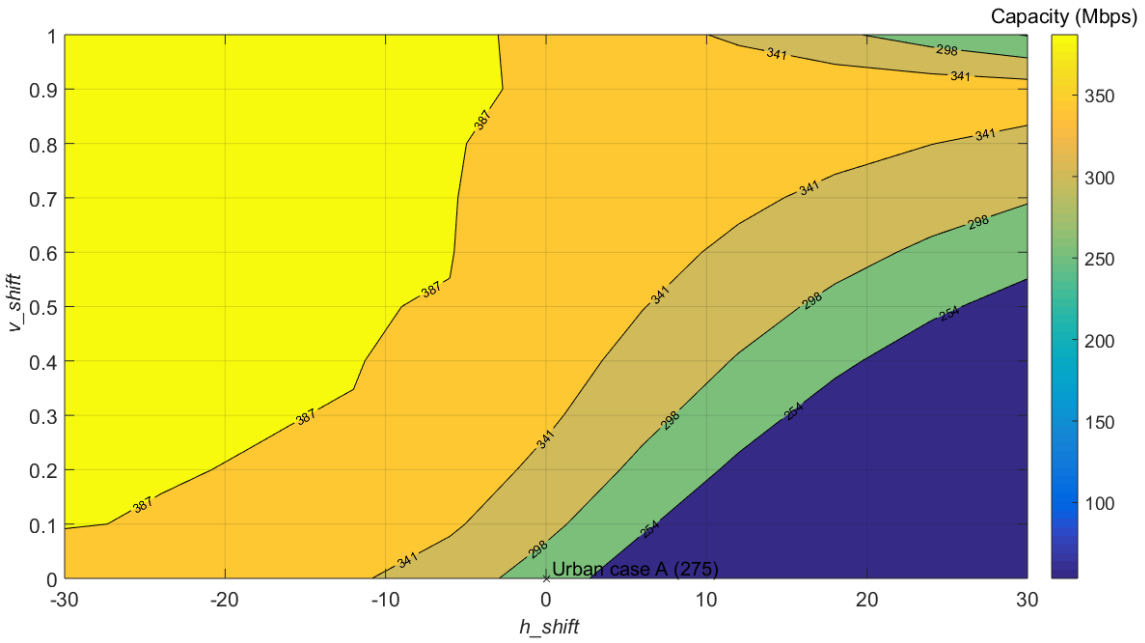
Capacity (Mbps)
v_shift
h_shift
Urban case A (275)
387
341
298
254

**(a)**

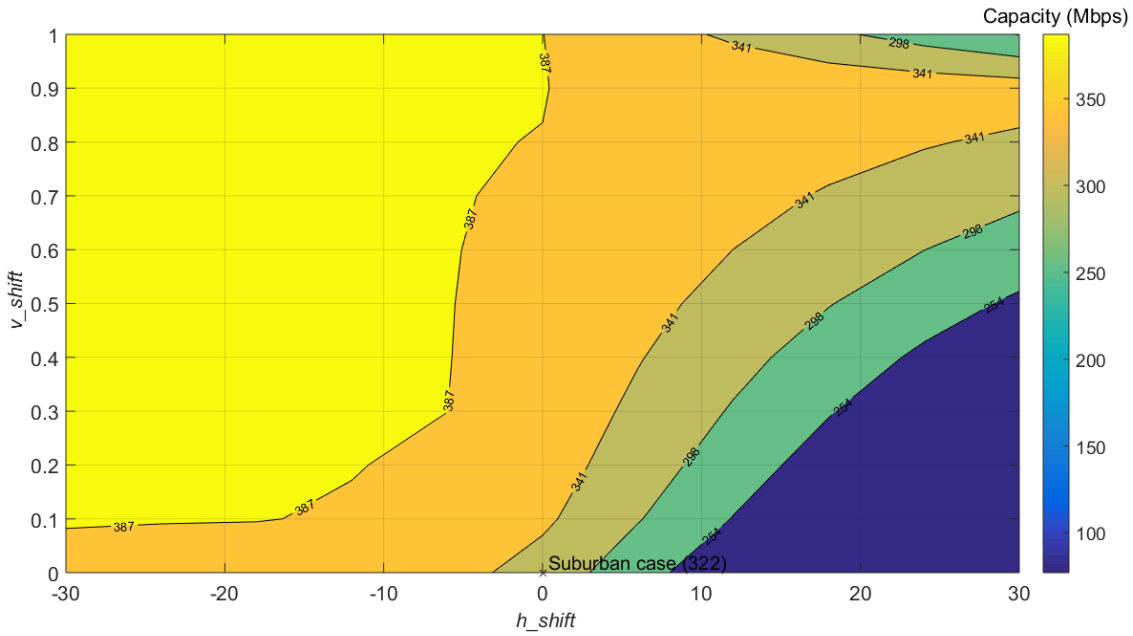
Capacity (Mbps)
v_shift
h_shift
Suburban case (322)
387
341
298
254

**(b)**

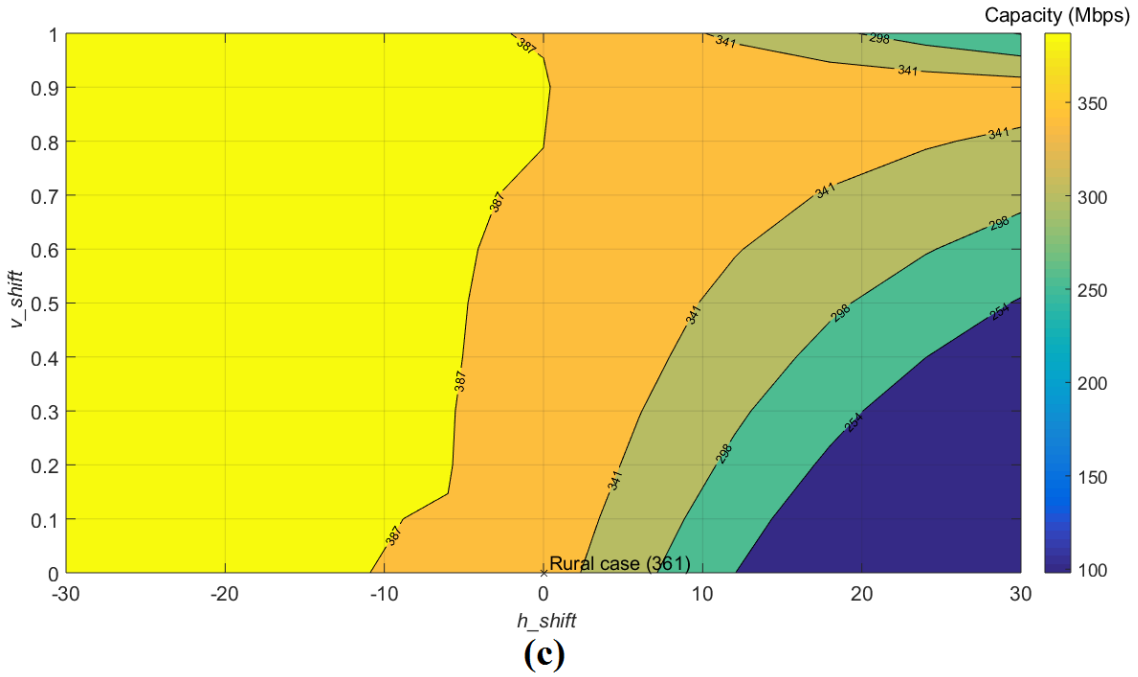


**Fig. 2**. mSHM class map for the average capacity of the OV LV BPL topologies in the 3-30MHz frequency band when WtG[1] coupling scheme is deployed and FCC Part 15 is applied for reference indicative OV HV BPL urban case A. (a) OV LV BPL urban case A. (b) OV LV BPL suburban case. (c) OV LV BPL rural case.

## 2.4 TIM Database Footprint on iSHM and mSHM Class Maps for the Default Operation Settings

In this Section, the footprint of the real OV LV BPL topologies is first illustrated on the iSHM and mSHM class maps of Sec.2.3 thus distinguishing the real OV LV BPL topologies from the virtual ones. With reference to the TIM database [20], real OV LV BPL topologies with their respective theoretical coupling scheme channel transfer functions can be retrieved. However, there is a trade-off during the preparation of the TIM database of interest between the detail degree of the assumed topological characteristics and the execution time of the theoretical coupling scheme channel transfer function and capacity computations through DHM. The TIM BPL topology database specifications that have been reported in [20] for the database preparation and affect the total execution time are the maximum number of branches $N$, the length spacing $L_s$ for both branch distance and branch length and the maximum branch length $L_b$ while typical lengths of 1000m are assumed for the real OV LV BPL topologies. To maintain realistic total execution times of the footprint representations, two different cases concerning the footprint of real OV LV BPL topologies are here examined; say, the footprints of real OV LV BPL topologies with one and two branches on iSHM and mSHM class maps. Note that the TIM BPL topology database specifications and total execution time that correspond to each scenario and class map type are also reported.

As the iSHM footprint of the real OV LV BPL topologies with one branch are concerned, the maximum number of branches $N$, the length spacing $L_s$ for both branch distance and branch length and the maximum branch length $L_b$ are assumed to be equal to

1 m, 10 m and 1000 m, respectively. With reference to the iSHM class map of Fig. 1, the iSHM footprint of the real OV LV BPL topologies with one branch is illustrated as superimposed white areas on class maps in Fig. 3(a). Similarly, the iSHM footprint of the real OV LV BPL topologies with two branches is illustrated in Fig. 3(b) when the maximum number of branches $N$, the length spacing $L_s$ for both branch distance and branch length and the maximum branch length $L_b$ are assumed to be equal to 2, 100m and 1000m, respectively.

As the mSHM footprint of the real OV LV BPL topologies with one branch are regarded, the TIM BPL topology database specifications are assumed to be the same with the ones of the iSHM footprint case. With reference to the mSHM class map of Fig. 2(c), the mSHM footprint of the real OV LV BPL topologies with one branch is illustrated as white areas in Fig. 4(a). Similarly, the mSHM footprint of the real OV LV BPL topologies with two branches is illustrated in Fig. 4(b) when the TIM BPL topology database specifications are assumed to be the same with the ones of the mSHM footprint case.

From Figs. 3(a), 3(b), 4(a) and 4(b), interesting observations concerning the iSHM and mSHM footprint planning of the real OV LV BPL topologies can be pointed out. More specifically:

- Since iSHM and mSHM class maps have already been prepared in Sec. 2.3, the total execution time considers the time that is required for the preparation of the TIM database given the TIM database specifications per each case as well as the required statistical and capacity processing. In terms of time, for the preparation of the footprints shown in Figs. 3(a), 3(b), 4(a) and 4(b), the total execution time is equal to 9674s, 7291s, 11646s, and 8567s, respectively. The different TIM database specifications regarding the two cases have been made so that the total execution time can remain relatively low without affecting the generality of the analysis. Anyway, different number of OV LV BPL topologies was expected for the two cases.
- With reference to Fig. 3(a), the iSHM footprint of OV LV BPL topologies with one branch is clearly confined in the rural case area. More specifically, as the length of the sole branch of the examined OV LV BPL topology decreases, this forces the presence of deep notches in the corresponding theoretical coupling scheme channel transfer function thus creating a richer multipath environment [12]. Conversely, the consideration of longer branches can impose more frequent but less deep notches in the corresponding theoretical coupling scheme channel transfer functions in comparison with the shorter branches. In accordance with [1], [180], OV LV BPL topologies of rare but less deep notches are characterized by increased values of $\hat{\alpha}_{\mathrm{MLE}}^{\mathrm{Weibull}}$ and $\hat{\beta}_{\mathrm{MLE}}^{\mathrm{Weibull}}$ and lower capacities. As the relative location of the OV LV BPL topologies with one short branch is concerned in the iSHM footprint, these topologies tend to be located at the lower left regions of the iSHM footprint while the OV LV BPL topologies with longer branches tend to be located at the opposite direction. Same observations can be expressed for the case of OV LV BPL topologies with two branches, where OV LV BPL topologies of two branches remain in the suburban case area with similar branch length behavior regarding the relative location in the class map suburban case area with the case of a single branch.

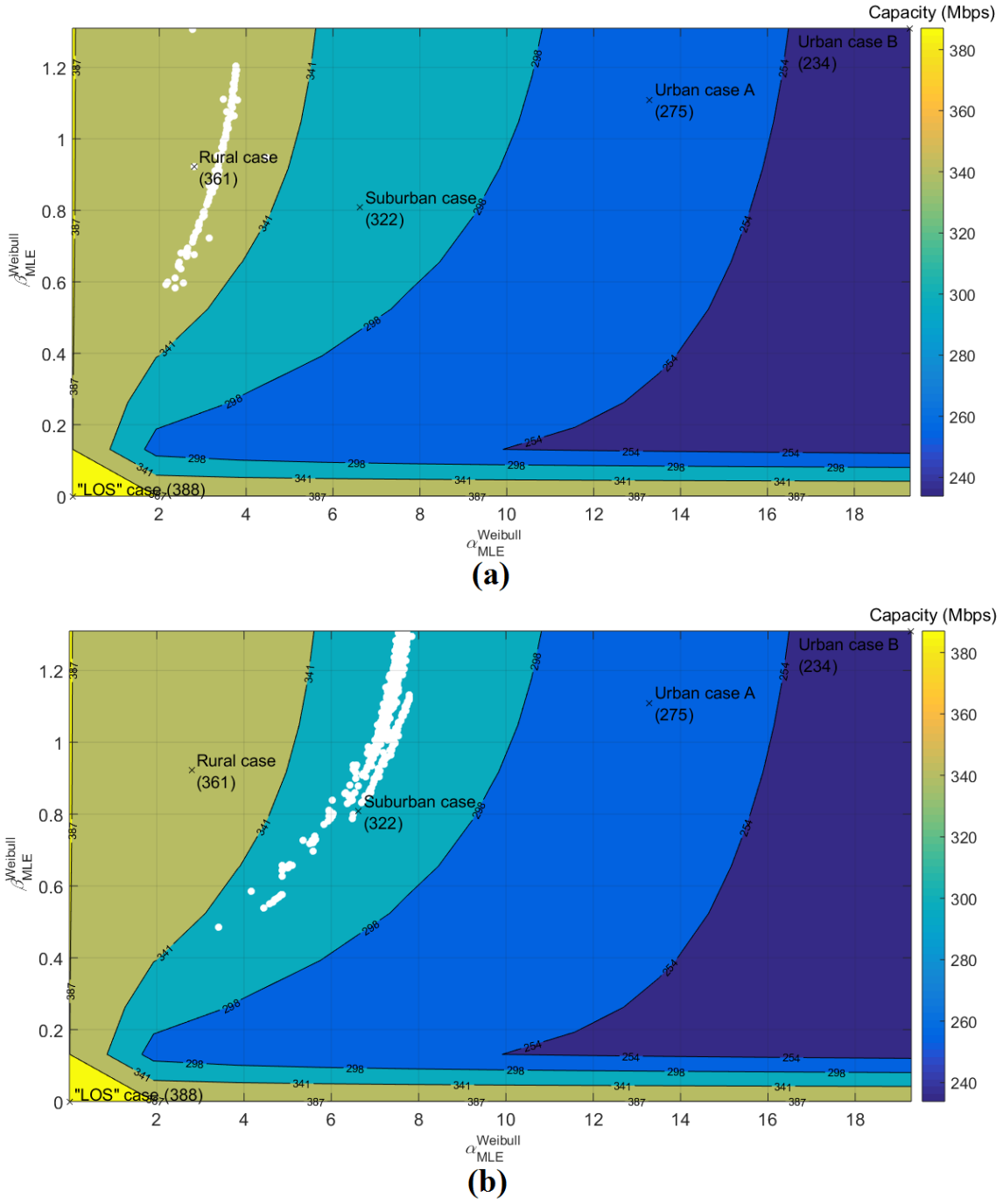


**Fig. 3**. Footprints of the real OV LV BPL topologies of the TIM database. (a) iSHM footprint of OV LV BPL topologies with one branch. (b) iSHM footprint of OV LV BPL topologies with two branches.

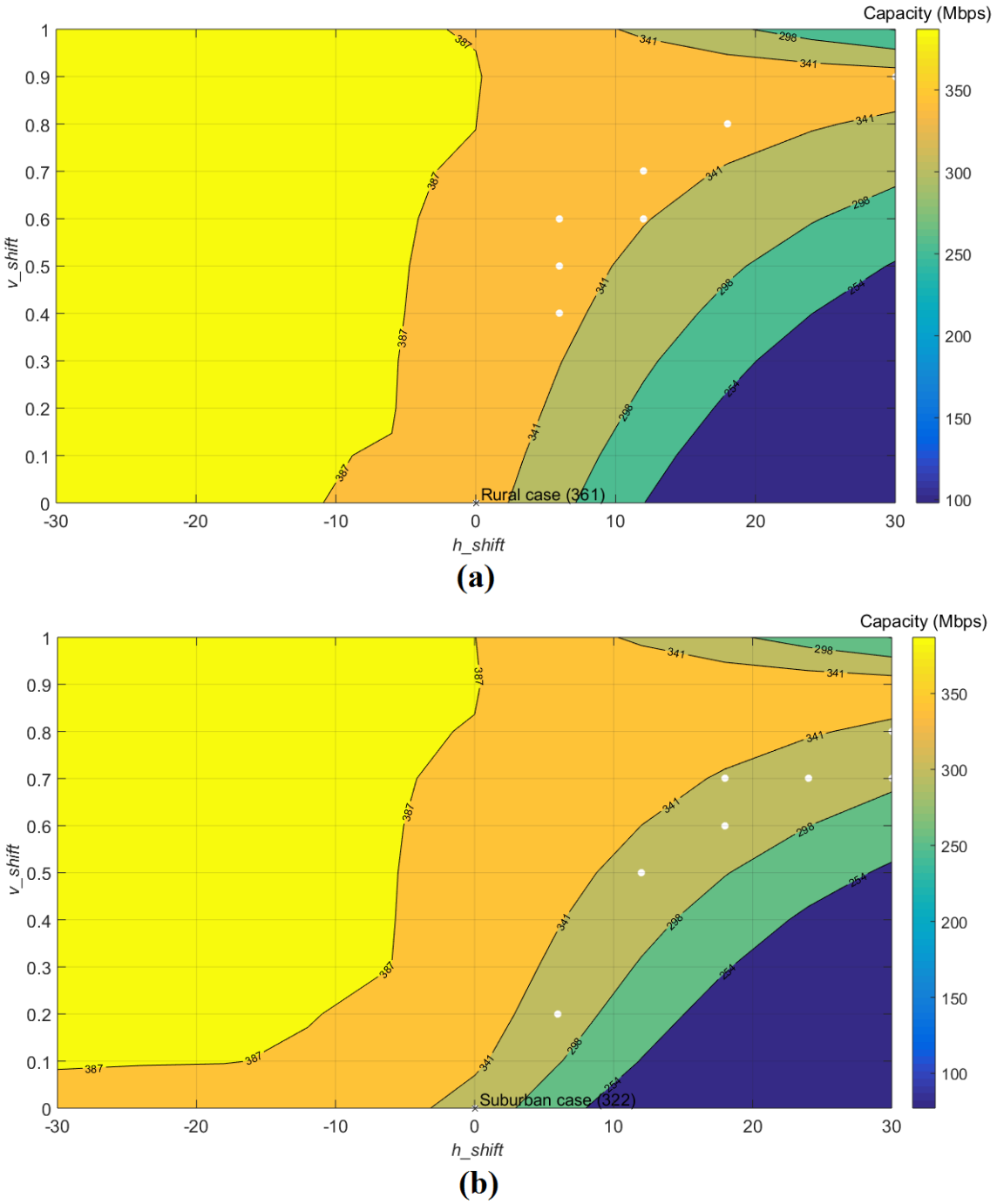


**Fig. 4**. Footprints of the real OV LV BPL topologies of the TIM database. (a) mSHM footprint of OV LV BPL topologies with one branch. (b) mSHM footprint of OV LV BPL topologies with two branches.

- With reference to Figs. 4(a) and 4(b), the mSHM footprints of OV LV BPL topologies with one and two branches are clearly confined in the rural and suburban case areas, respectively. Although the number of the examined OV LV BPL topologies remains the same given the number of branches, the main difference between iSHM and mSHM footprints is first their extent; this is due to

the fact that the examined real OV LV BPL topologies are characterized by their own CASD MLEs during the iSHM definition procedure and can be straightforward superimposed to iSHM class maps whereas the examined real OV LV BPL topologies are classified among the existing pairs $[h\_shift \quad v\_shift]$ of the mSHM class maps and demonstrated as white spots through the practical approximation of Frobenius distance analyzed in Sec.4.1 of [1]. As the number of spacings of the horizontal and vertical axes of the mSHM class maps of Figs. 2(a)-(c) is both equal to 10, all the white spots of Figs. 3(a) and 3(b) are classified into 8 white spots in Figs. 4(a) and 4(b), respectively. It is evident that as the number of spacings of the horizontal and vertical axes increases so does the number of white spots of the mSHM footprints of the real OV LV BPL topologies since a larger set of available pairs $[h\_shift \quad v\_shift]$ can be examined.

- The latter difference between the illustration of iSHM and mSHM footprints also explains the greater total execution times of mSHM footprints, which have been reported, in comparison with the ones of iSHM footprints for given number of branches of the real OV LV BPL topologies. As it is shown, the straightforward CASD MLE computation of iSHM definition procedure remains faster than the comparison among all the available virtual OV LV BPL topologies of each OV LV BPL topology subclass during the preparation of mSHM footprints.

## 2.5 FIIM Database Footprint on iSHM and mSHM Class Maps for the Default Operation Settings

In this Section, the iSHM and mSHM footprints of the real OV LV BPL topologies with a sole branch line fault are first illustrated. For given real OV LV BPL topology, say, OV LV BPL urban case A, one branch line fault is once applied to each of the three branches of the examined OV LV BPL urban case A. With reference to the FIIM database [20], real OV LV BPL topologies with one branch line fault that are based on the OV LV BPL urban case A with their respective theoretical coupling scheme channel transfer functions can be retrieved. Similarly to the TIM database specifications, appropriate FIIM BPL topology database specifications that have been reported in [1] for the database preparation are assumed, namely the fault location at each existing branch of the real indicative OV LV BPL urban case A ranges from 0.1 m to the end of the corresponding branch with a step of 0.1m. Note that the faulty branch termination is again assumed to be open-circuit.

As the iSHM footprint of the real OV LV BPL topologies with one branch line fault that are based on the real indicative OV LV BPL urban case A is concerned, the iSHM footprint of the real OV LV BPL topologies with one branch line fault is illustrated as superimposed white areas on class maps in Fig. 5 with reference to the iSHM class map of Fig. 1. Similarly to iSHM footprint of Fig. 5, the mSHM footprint of the real OV LV BPL topologies with one branch line fault that are based on the real indicative OV LV BPL urban case A is shown in Fig. 6.

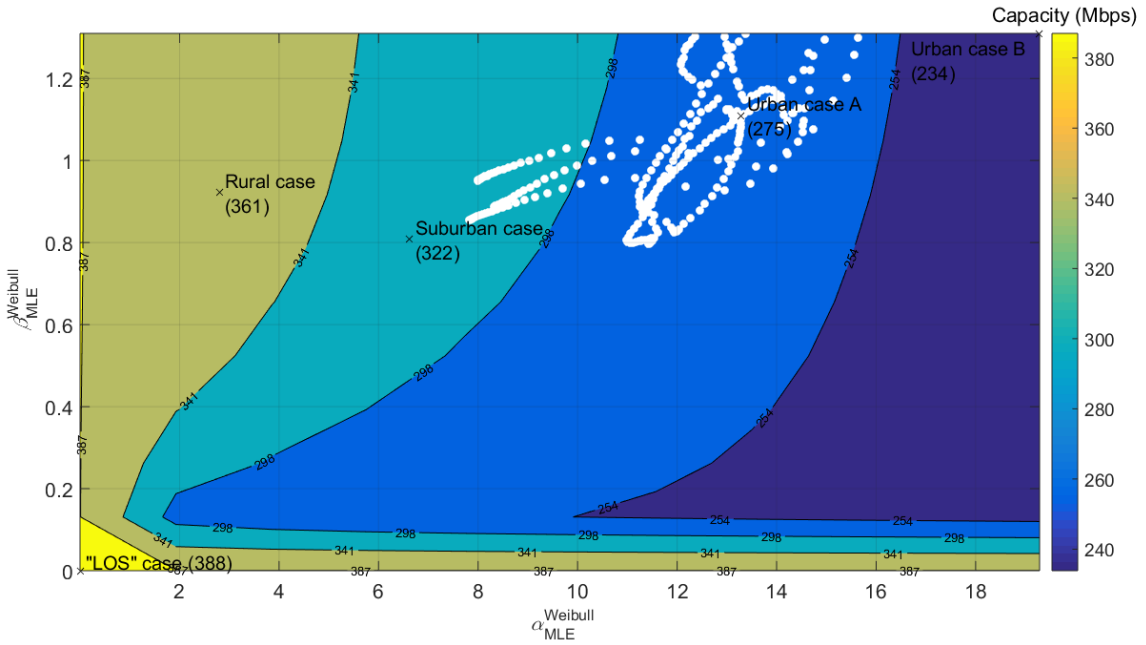


**Fig. 5**. iSHM footprint of the real OV LV BPL topologies of the FIIM database with one branch line fault with reference to the real indicative OV LV BPL urban case A.

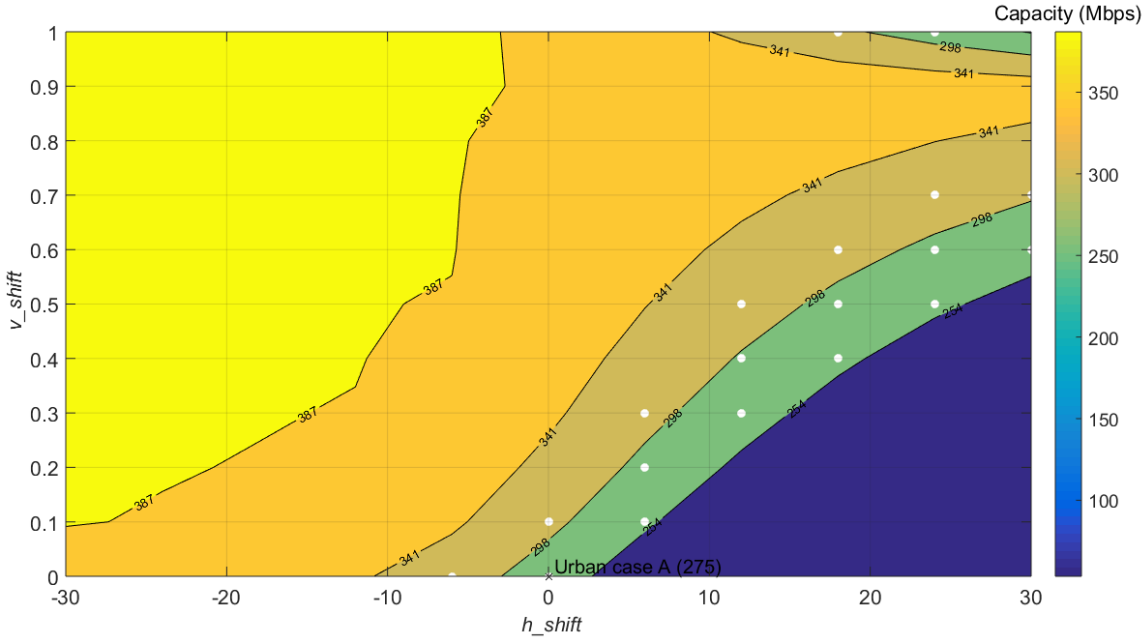


**Fig. 6**. mSHM footprint of the real OV LV BPL topologies of the FIIM database with one branch line fault with reference to the real indicative OV LV BPL urban case A.

From Figs. 5 and 6, it is observed that the real OV LV BPL topologies with one branch line fault, which are based on the real indicative OV LV BPL urban case A, are not strictly bounded in the class area of urban case A but are also extended to the class area of suburban case either in iSHM class map or in mSHM class map. The branch line faults of the real OV LV BPL topologies that are situated at the class area of the suburban

case are characterized by branch line lengths that are lower than approximately 2 m (short branches). This remark can be considered as the continuation of the remark of Sec.2.4, which has dealt with the relative position of OV LV BPL topologies with short branches at iSHM footprints (*i.e.*, lower left regions of the corresponding class areas). Hence, iSHM and mSHM class maps better distinguishes branch line faults of short lengths since the corresponding OV LV BPL topologies with the branch line faults violate the class area borders thus allowing their imminent detection. In general, iSHM and mSHM class maps consist of class areas that are mainly represented by real OV LV BPL topologies of different number of long branches. The last observation about iSHM and mSHM class maps introduces a new technique concerning the detection of branch line faults and energy theft hooks (see also Sec.2.6) that depends on the characterization of the examined OV LV BPL topologies in terms of their number of long branches and not on the straightforward benchmark of their spectral metrics, such as coupling scheme transfer functions and capacities presented in [21]-[28].

## 2.6 HS-DET Method Database Footprint on iSHM and mSHM Class Maps for the Default Operation Settings

In this Section, the iSHM and mSHM footprints of the real OV LV BPL topologies with a single hook for energy theft are first illustrated. For given real OV LV BPL topology, say, the real indicative OV LV BPL suburban case, one hook, which is treated as a new branch [21], [29], [30], is hung on the existing real indicative OV LV BPL suburban case. With reference to HS-DET method database [21], real OV LV BPL topologies with a single hook for energy theft that are based on the real indicative OV LV BPL suburban case with their respective theoretical coupling scheme channel transfer functions can be retrieved. Similarly to the TIM and FIIM database specifications, appropriate HS-DET method database specifications that have been reported in [20] for the database preparation are assumed, namely the location of the hook for energy theft that ranges from 0.1 m to 1000 m with a step of 10 m and the length of the hook that ranges from 0.1 m to 200 m with a step of 10 m. Note that the branch termination, which is used for the simulation of the hook of the energy theft, is again assumed to be open-circuit.

As the iSHM footprint of the real OV LV BPL topologies with a single hook for energy theft that are based on the real indicative OV LV BPL suburban case is concerned, the iSHM footprint of the real OV LV BPL topologies with a single energy theft hook is illustrated as superimposed white areas on class maps in Fig. 7 with reference to the iSHM class map of Fig. 1. Similarly to iSHM footprint of Fig. 7, the mSHM footprint of the real OV LV BPL topologies with a single hook for energy theft that are based on the real indicative OV LV BPL suburban case is shown in Fig. 8.

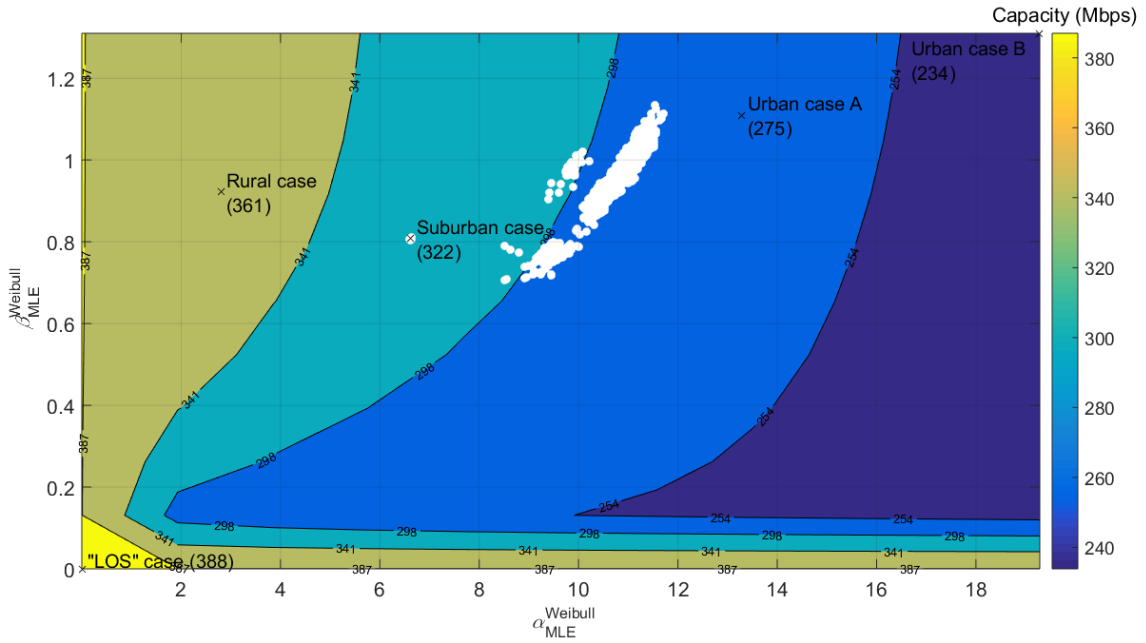


**Fig. 7**. iSHM footprint of the real OV LV BPL topologies of the HS-DET method database with a single hook for energy theft with reference to the real indicative OV LV BPL suburban case.

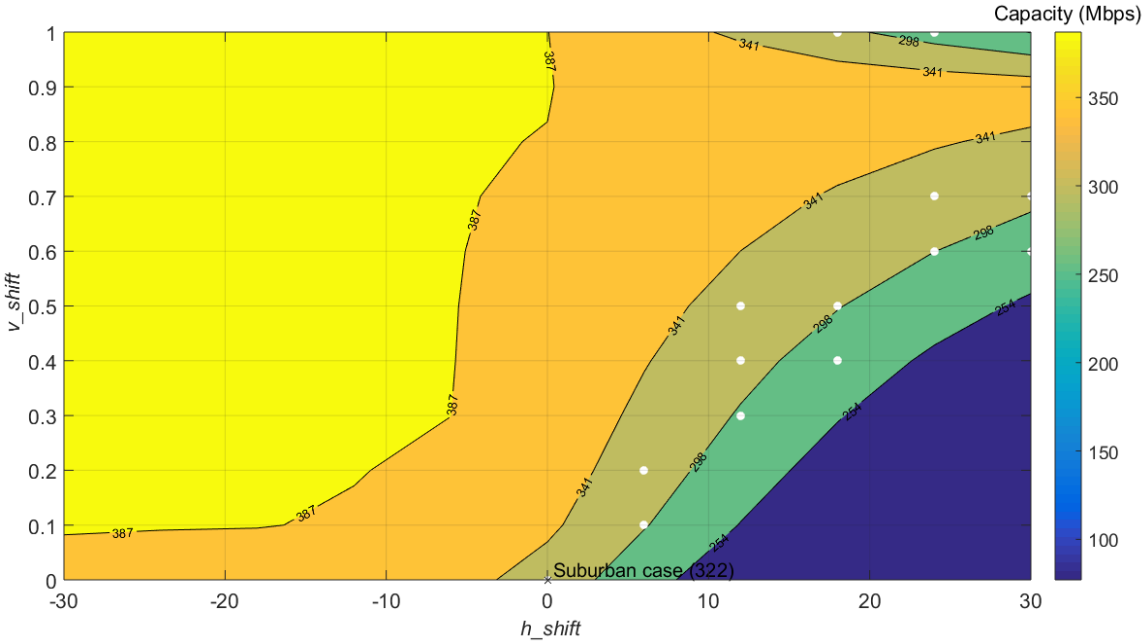


**Fig. 8**. mSHM footprint of the real OV LV BPL topologies of the HS-DET method database with a single hook for energy theft with reference to the real indicative OV LV BPL suburban case.

From Figs. 7 and 8, it is evident that the proposed technique concerning the detection of branch line faults through iSHM and mSHM footprints can be easily extended in order to detect hooks for energy theft. Indeed, the insertion of a single hook, which is treated by the DHM as a new branch insertion to the existing real indicative OV LV BPL suburban case, has as result the shift of the iSHM and mSHM footprints right

inside the class area of urban case A with few exceptions that remain close to the right border of the class area of suburban case; the later exceptions are real OV LV BPL topologies that derive from the real indicative OV LV BPL suburban case while short hooks for energy thefts are deployed across them. Since the relative location of iSHM and mSHM footprints is more sensitive to the number of long branches rather than the multipath environment aggravation due to the short branches, the detection of the hooks for energy theft becomes easier in comparison with the detection of the branch line faults due to the visible violation of class area borders. Here, it should be mentioned that the detection of long hooks for energy thefts that is offered by the examination of the iSHM footprints may act as supplementary technique to the HS-DET method of [21], [29]-[31] that detects more easily the short hooks for energy theft.

## 3. Conclusions

In this second paper, the numerical results concerning the iSHM and mSHM footprints of the OV LV BPL networks have been demonstrated as well as a new technique, which acts supplementary to the existing FIIM and HS-DET method. From iSHM and mSHM footprints of the OV LV BPL topologies it has been verified that: (i) Depending on the number of branches, the real OV LV BPL topologies are classified in the existing class areas; (ii) As the length of the branches of the real OV LV BPL topologies increases, their iSHM footprint tends to be located at the upper right regions of the corresponding class area; (iii) Branch line faults and hook style energy theft can be easily identified by studying the relative location in the corresponding class area given the real OV LV BPL topology of the basis; (iv) Hook style energy theft can be more easily detected in comparison with the branch line faults; and (v) Complimentary to FIIM and HS-DET method, which better operate with short branches, the study of iSHM and mSHM footprints can act as a useful supplementary technique for identifying branch line faults of short branches and hook style energy thefts of long hooks.

## CONFLICTS OF INTEREST

The author declares that there is no conflict of interests regarding the publication of this paper.

## References

[1] A. G. Lazaropoulos, “Statistical Channel Modeling of Overhead Low Voltage Broadband over Power Lines (OV LV BPL) Networks – Part 1: The Theory of Class Map Footprints of Real OV LV BPL Topologies, Branch Line Faults and Hook-Style Energy Thefts,” *Trends in Renewable Energy*, vol. 6, no. 1, pp. 61-87.

[2] G. López, J. Matanza, D. de la Vega, M. Castro, A. Arrinda, J. I. Moreno, and A. Sendin, “The Role of Power Line Communications in the Smart Grid Revisited: Applications, Challenges, and Research Initiatives,” *IEEE Access*, vol. 7, pp. 117346–117368, 2019.

[3] A. G. Lazaropoulos and P. G. Cottis, "Transmission characteristics of overhead medium voltage power line communication channels," *IEEE Trans. Power Del.*, vol. 24, no. 3, pp. 1164-1173, Jul. 2009.

[4] A. G. Lazaropoulos and P. G. Cottis, "Broadband transmission via underground medium-voltage power lines-Part I: transmission characteristics," *IEEE Trans. Power Del.*, vol. 25, no. 4, pp. 2414-2424, Oct. 2010.

[5] E. Biglieri, "Coding and modulation for a horrible channel," *IEEE Commun. Mag.*, vol. 41, no. 5, pp. 92–98, May 2003.

[6] M. Gebhardt, F. Weinmann, and K. Dostert, "Physical and regulatory constraints for communication over the power supply grid," *IEEE Commun. Mag.*, vol. 41, no. 5, pp. 84-90, May 2003.

[7] M. Götz, M. Rapp, and K. Dostert, "Power line channel characteristics and their effect on communication system design," *IEEE Commun. Mag.*, vol. 42, no. 4, pp. 78-86, Apr. 2004.

[8] A. G. Lazaropoulos, "Towards Broadband over Power Lines Systems Integration: Transmission Characteristics of Underground Low-Voltage Distribution Power Lines," *Progress in Electromagnetics Research B*, vol. 39, pp. 89-114, 2012. [Online]. Available: http://www.jpier.org/PIERB/pierb39/05.12012409.pdf

[9] A. G. Lazaropoulos and P. G. Cottis, "Capacity of overhead medium voltage power line communication channels," *IEEE Trans. Power Del.*, vol. 25, no. 2, pp. 723-733, Apr. 2010.

[10] A. G. Lazaropoulos and P. G. Cottis, "Broadband transmission via underground medium-voltage power lines-Part II: capacity," *IEEE Trans. Power Del.*, vol. 25, no. 4, pp. 2425-2434, Oct. 2010.

[11] A. G. Lazaropoulos, "Broadband transmission and statistical performance properties of overhead high-voltage transmission networks," *Hindawi Journal of Computer Networks and Commun.*, 2012, article ID 875632, 2012. [Online]. Available: http://www.hindawi.com/journals/jcnc/aip/875632/

[12] A. G. Lazaropoulos, "Towards Modal Integration of Overhead and Underground Low-Voltage and Medium-Voltage Power Line Communication Channels in the Smart Grid Landscape: Model Expansion, Broadband Signal Transmission Characteristics, and Statistical Performance Metrics (Invited Paper)," *ISRN Signal Processing*, vol. 2012, Article ID 121628, pp. 1-17, 2012. [Online]. Available: http://www.hindawi.com/isrn/sp/2012/121628/

[13] A. G. Lazaropoulos, "Broadband Performance Metrics and Regression Approximations of the New Coupling Schemes for Distribution Broadband over Power Lines (BPL) Networks," *Trends in Renewable Energy*, vol. 4, no. 1, pp. 43-73, Jan. 2018. [Online]. Available: http://futureenergysp.com/index.php/tre/article/view/59/pdf

[14] A. G. Lazaropoulos, "Statistical Broadband over Power Lines Channel Modeling – Part 1: The Theory of the Statistical Hybrid Model," *Progress in Electromagnetics Research C*, vol. 92, pp. 1-16, 2019. [Online]. Available: http://www.jpier.org/PIERC/pierc92/01.19012902.pdf

[15] A. G. Lazaropoulos, "Statistical Broadband over Power Lines (BPL) Channel Modeling – Part 2: The Numerical Results of the Statistical Hybrid Model,"

*Progress in Electromagnetics Research C*, vol. 92, pp. 17-30, 2019. [Online]. Available: http://www.jpier.org/PIERC/pierc92/02.19012903.pdf

[16] A. G. Lazaropoulos, "Enhancing the Statistical Hybrid Model Performance in Overhead and Underground Medium Voltage Broadband over Power Lines Channels by Adopting Empirical Channel Attenuation Statistical Distribution," *Trends in Renewable Energy*, vol. 5, no. 2, pp. 181-217, 2019. [Online]. Available: http://futureenergysp.com/index.php/tre/article/view/96/pdf

[17] A. G. Lazaropoulos, "Virtual Indicative Broadband over Power Lines Topologies for Respective Subclasses by Adjusting Channel Attenuation Statistical Distribution Parameters of Statistical Hybrid Models – Part 1: Theory," *Trends in Renewable Energy*, vol. 5, no. 3, pp. 237-257, Aug. 2019. [Online]. Available: http://futureenergysp.com/index.php/tre/article/view/99/pdf

[18] A. G. Lazaropoulos, "Virtual Indicative Broadband over Power Lines Topologies for Respective Subclasses by Adjusting Channel Attenuation Statistical Distribution Parameters of Statistical Hybrid Models – Part 2: Numerical Results for the Overhead and Underground Medium-Voltage Power Grids," *Trends in Renewable Energy*, vol. 5, no. 3, pp. 258-281, Aug. 2019. [Online]. Available: http://futureenergysp.com/index.php/tre/article/view/100/pdf

[19] A. G. Lazaropoulos, "Virtual Indicative Broadband over Power Lines Topologies for Respective Subclasses by Adjusting Channel Attenuation Statistical Distribution Parameters of Statistical Hybrid Models – Part 3: The Case of Overhead Transmission Power Grids," *Trends in Renewable Energy*, vol. 5, no. 3, pp. 282-306, Aug. 2019. [Online]. Available: http://futureenergysp.com/index.php/tre/article/view/101/pdf

[20] A. G. Lazaropoulos, "Improvement of Power Systems Stability by Applying Topology Identification Methodology (TIM) and Fault and Instability Identification Methodology (FIIM)–Study of the Overhead Medium-Voltage Broadband over Power Lines (OV MV BPL) Networks Case," *Trends in Renewable Energy*, vol. 3, no. 2, pp. 102-128, Apr. 2017. [Online]. Available: http://futureenergysp.com/index.php/tre/article/view/34

[21] A. G. Lazaropoulos, "Detection of Energy Theft in Overhead Low-Voltage Power Grids – The Hook Style Energy Theft in the Smart Grid Era," *Trends in Renewable Energy*, vol. 5, no. 1, pp. 12-46, Oct. 2018. [Online]. Available: http://futureenergysp.com/index.php/tre/article/view/81/pdf

[22] A. G. Lazaropoulos, "Measurement Differences, Faults and Instabilities in Intelligent Energy Systems – Part 2: Fault and Instability Prediction in Overhead High-Voltage Broadband over Power Lines Networks by Applying Fault and Instability Identification Methodology (FIIM)," *Trends in Renewable Energy*, vol. 2, no. 3, pp. 113-142, Oct. 2016. [Online]. Available: http://futureenergysp.com/index.php/tre/article/view/27/33

[23] A. G. Lazaropoulos, "Measurement Differences, Faults and Instabilities in Intelligent Energy Systems–Part 1: Identification of Overhead High-Voltage Broadband over Power Lines Network Topologies by Applying Topology Identification Methodology (TIM)," *Trends in Renewable Energy*, vol. 2, no. 3, pp. 85-112, Oct. 2016. [Online]. Available: http://futureenergysp.com/index.php/tre/article/view/26/32

[24] A. G. Lazaropoulos, "Power Systems Stability through Piecewise Monotonic Data Approximations – Part 1: Comparative Benchmarking of L1PMA, L2WPMA and L2CXCV in Overhead Medium-Voltage Broadband over Power Lines Networks," *Trends*

*in Renewable Energy*, vol. 3, no. 1, pp. 2-32, Jan. 2017. [Online]. Available: http://futureenergysp.com/index.php/tre/article/view/29/34

[25] A. G. Lazaropoulos, "Power Systems Stability through Piecewise Monotonic Data Approximations – Part 2: Adaptive Number of Monotonic Sections and Performance of L1PMA, L2WPMA and L2CXCV in Overhead Medium-Voltage Broadband over Power Lines Networks," *Trends in Renewable Energy*, vol. 3, no. 1, pp. 33-60, Jan. 2017. [Online]. Available: http://futureenergysp.com/index.php/tre/article/view/30/35

[26] A. G. Lazaropoulos, "Main Line Fault Localization Methodology in Smart Grid– Part 1: Extended TM2 Method for the Overhead Medium-Voltage Broadband over Power Lines Networks Case," *Trends in Renewable Energy*, vol. 3, no. 3, pp. 2-25, Dec. 2017. [Online]. Available: http://futureenergysp.com/index.php/tre/article/view/36

[27] A. G. Lazaropoulos, "Main Line Fault Localization Methodology in Smart Grid– Part 2: Extended TM2 Method, Measurement Differences and L1 Piecewise Monotonic Data Approximation for the Overhead Medium-Voltage Broadband over Power Lines Networks Case," *Trends in Renewable Energy*, vol. 3, no. 3, pp. 26-61, Dec. 2017. [Online]. Available: http://futureenergysp.com/index.php/tre/article/view/37

[28] A. G. Lazaropoulos, "Main Line Fault Localization Methodology in Smart Grid– Part 3: Main Line Fault Localization Methodology (MLFLM)," *Trends in Renewable Energy*, vol. 3, no. 3, pp. 62-81, Dec. 2017. [Online]. Available: http://futureenergysp.com/index.php/tre/article/view/38

[29] A. G. Lazaropoulos, "Special Cases during the Detection of the Hook Style Energy Theft in Overhead Low-Voltage Power Grids through HS-DET Method – Part 1: High Measurement Differences, Very Long Hook Technique and "Smart" Hooks," *Trends in Renewable Energy*, vol. 5, no. 1, pp. 60-89, Jan. 2019. [Online]. Available: http://futureenergysp.com/index.php/tre/article/view/82/pdf

[30] A. G. Lazaropoulos, "Special Cases during the Detection of the Hook Style Energy Theft in Overhead Low-Voltage Power Grids through HS-DET Method – Part 2: Different Measurement Differences, Feint "Smart" Hooks and Hook Interconnection Issues," *Trends in Renewable Energy*, vol. 5, no. 1, pp. 90-116, Jan. 2019. [Online]. Available: http://futureenergysp.com/index.php/tre/article/view/83/pdf

[31] A. G. Lazaropoulos, "The Role of Information Technology Department against the Hook Style Energy Theft in Smart Cities – Ad-Hoc Overhead Low-Voltage Broadband over Power Lines (OV LV BPL) Networks," *Trends in Renewable Energy*, vol. 5, no. 2, pp. 117-150, Apr. 2019. [Online]. Available: http://futureenergysp.com/index.php/tre/article/download/93/pdf



# CALL FOR PAPERS

# Trends in Renewable Energy

**ISSN Print: 2376-2136 ISSN online: 2376-2144**

**http://futureenergysp.com/index.php/tre/**

Trends in Renewable Energy (TRE) is an open accessed, peer-reviewed semi-annual journal publishing reviews and research papers in the field of renewable energy technology and science. The aim of this journal is to provide a communication platform that is run exclusively by scientists. This journal publishes original papers including but not limited to the following fields:

- ✧ Renewable energy technologies
- ✧ Catalysis for energy generation, Green chemistry, Green energy
- ✧ Bioenergy: Biofuel, Biomass, Biorefinery, Bioprocessing, Feedstock utilization, Biological waste treatment,
- ✧ Energy issues: Energy conservation, Energy delivery, Energy resources, Energy storage, Energy transformation, Smart Grid
- ✧ Environmental issues: Environmental impacts, Pollution
- ✧ Bioproducts
- ✧ Policy, etc.

We publish the following article types: peer-reviewed reviews, mini-reviews, technical notes, short-form research papers, and original research papers.

*The article processing charge (APC), also known as a publication fee, is fully waived for the Trends in Renewable Energy.*

## Call for Editorial Board Members

We are seeking scholars active in a field of renewable energy interested in serving as volunteer Editorial Board Members.

**Qualifications**

Ph.D. degree in related areas, or Master's degree with a minimum of 5 years of experience. All members must have a strong record of publications or other proofs to show activities in the energy related field.

If you are interested in serving on the editorial board, please email CV to editor@futureenergysp.com.